九州大学学術情報リポジトリ
Kyushu University Institutional Repository

Highly Selective Hydrogen Sensor Based on YSZ and Oxide Sensing Electrode

スリ，アユ，アンガライニ

https://doi.org/10.15017/1441282

出版情報：九州大学，2013，博士（工学），課程博士
バージョン：
権利関係：全文ファイル公表済

KYUSHU UNIVERSITY

Highly Selective Hydrogen Sensor Based on YSZ and Oxide Sensing Electrode

Sri Ayu Anggraini

Interdisciplinary Graduate School of Engineering Sciences

Kyushu University

2014

Table of Contents

Chapter 1 General Introduction 1

Abstract 1

1.1 Hydrogen Economy 3

1.2 Hydrogen Sensing Technologies 6

1.2.1 Conventional gas analyzer vs. solid-state gas sensor 6

1.2.2 Solid-state H_2 sensor 7

1.3 YSZ-based potentiometric gas sensor 17

1.3.1 Equilibrium potential type YSZ-based oxygen sensor 18

13.2 Mixed-potential type YSZ-based gas sensor 21

1.3.3 Sensing electrode materials for mixed-potential type YSZ-based sensor 23

1.4 H_2 detection by mixed-potential type YSZ-based sensor 26

1.5 Challenges and trends in solid-state H_2 sensor 30

1.6 Aim and scope of this study 32

References 34

Chapter 2 Selective Hydrogen Detection by Combining Two-oxides-based Sensing Electrodes 38

2.1 Introduction 38

2.2 Experimental 39

2.2.1 Fabrication of sensor devices 39

2.2.2 Evaluation of sensing properties of the single-type sensor 41

2.2.3 Polarization curve measurements 43

2.2.4 Morphology and crystal structure of the SE 43

2.3 Results and discussion 43

2.3.1 The single-type sensor using SnO_2-based-SE 43

2.3.2 Construction of the combined-type sensor 51

2.4 Conclusions 54

References 57

Chapter 3 SnO_2-based Sensing Electrode with Integrated Catalyst Layer for Selective H_2 detection 58

3.1 Introduction 58

3.2 Experimental 59

3.2.1 Fabrication of sensing devices 59
3.2.2 Evaluation of sensing properties 60
3.2.3 Catalyst material investigation 61
3.2.4 Polarization curve measurements 61
3.2.5 Morphology observation and crystal phase determination of the SE 62
3.3 Results and discussion 62
3.3.1 Selection of a suitable catalyst material for selective C_3H_6 oxidation 62
3.3.2 Influence of a Cr_2O_3 on the sensing characteristic of the sensor using SnO_2 (+ 30 wt.% YSZ)-SE 63
3.3.3 Sensing characteristic of the sensor using SnO_2(+ 30 wt.% YSZ)-SE enveloped with Al_2O_3 and coated with Cr_2O_3 67
3.4 Conclusions 73
References 75

Chapter 4 H_2 Sensing Characteristics of the Sensor Utilizing $Zn_3Ta_2O_8$-based Sensing Electrode 76
4.1 Introduction 76
4.2 Experimental 77
4.2.1 Sensor fabrication 77
4.2.2 Sensing-performance evaluation 77
4.2.3 Polarization curve measurements 78
4.2.4 Morphology and crystal structure of the SE 79
4.3 Results and discussion 80
4.3.1 Effect of Ta_2O_5 addition into ZnO-SE on H_2 sensitivity 80
4.3.2 Effect of sintering temperature of SE on H_2 sensing characteristics 84
4.3.3 Sensing characteristics of the sensor using ZnO(+ 30 wt.% Ta_2O_5)-SE sintered at 1300^{o}C 90
4.4 Conclusions 93
References 94

Chapter 5 H_2 Sensing Characteristic of the Sensor Utilizing $ZnTa_2O_6$-based Sensing Electrode 95
5.1 Introduction 95
5.2 Experimental 96
5.2.1 Sensor fabrication 96
5.2.2 Sensing-performance evaluation 97
5.2.3 Morphology and crystal structure of the SE 98

5.2.4 Polarization curve measurements 98
5.3 Results and Discussion 99
5.3.1 Effect of Ta_2O_5 addition into ZnO-SE on H_2 sensitivity 99
5.3.2 Crystal structure and morphology of Zn-Ta-based oxide SE materials 102
5.3.3 The initial sensing characteristics of the sensor using ZnO(+ 84 wt.% Ta_2O_5)-SE . 107
5.3.4 Sensing characteristics of the sensor using ZnO(+ 84 wt.% Ta_2O_5)-SE after aging 109
5.4 Conclusions 114
References 116

Chapter 6 Insight into Aging Effect on Enhancement of H_2 Sensing Characteristics of the Sensor Utilizing $ZnTa_2O_6$-based Sensing Electrode 117
6.1 Introduction 117
6.2 Experimental 118
6.2.1 Sensor fabrication 118
6.2.2 Sensing-performance evaluation 118
6.2.3 Polarization curve measurements 119
6.2.4 XRD, SEM and XPS measurements 120
6.2.5 Evaluation of gas-phase catalytic activity 120
6.3 Results and discussion 121
6.3.1 Effect of aging on electrode composition and morphology 121
6.3.2 Effect of aging on chemical surface state of SE 126
6.3.3 Effect of aging on catalytic activity 128
6.3.4 Aging mechanism in enhancing sensitivity and selectivity against H_2 135
6.4 Conclusions 138
References 141

Chapter 7 Summary and future works 143
7.1 Summary of the thesis 143
7.2 Future works 146

Acknowledgements 148

Chapter 1

General Introduction

Abstract

The need for an alternative energy sources to replace the dominant fossil fuel has lead us to the use of hydrogen (H_2) as one of the most potential fuel candidates for various applications, from industrial to automotive and even space exploration. Furthermore, the introduction of fuel cell as a stationary power generator has also brought about a lot of attentions to H_2, particularly since the utilization of H_2 produce less pollutant and produce relatively higher energy. Additionally, the abundant source of H_2 on earth makes the prospect of H_2 very attractive as a sustainable alternative energy carrier in the future. The main issue in H_2 utilization (production, storage and delivery) is the safety aspect, since the presence of H_2 in concentration as low as 4 vol.% in air could easily cause a lethal conflagration, posing hazard to the users or operator of the instruments in which H_2 involved. Therefore, a gas sensing device that is capable of detecting and monitoring H_2 in concentration below the lower explosive limit will be of paramount important component to ensure the smooth transition from the fossil fuel-based to H_2 economy.

Among the currently available sensing devices, a solid-state gas sensor based on yttria-stabilized zirconia (YSZ) has been long considered as a strong candidate for a high-performance gas sensor, due to its high sensitivity, low cost for operation and maintenance as well as stable performance during long-term operation. Up to this moment, there have been only a few of highly sensitive and selective mixed-potential type YSZ-based sensor for detection of H_2. Given the important role of H_2 in the future,

the development of a high-performance H_2 sensor using YSZ as the solid electrolyte is highly necessary. The sensing performance of a potentiometric YSZ-based sensor is highly determined by the physical and chemical properties of the sensing electrode (SE) material employed. Finding a suitable SE material that can detect H_2 sensitively with minor cross sensitivity toward other interfering gases is a pivotal point in developing an excellent gas sensor. In the light of finding a substitute for expensive noble metal, metal oxide has been intensively studied as a prospective H_2 sensing electrode material. However, the main challenge in utilizing metal oxide as SE for a mixed-potential-type sensor is the cross selectivity toward the co-existing gases.

In this chapter, the importance of H_2 as alternative energy resources and an H_2 sensor for the whole H_2 economy scenario will be introduced. Assorted types solid state sensors for H_2 detection will also be briefly elaborated here. The development of mixed-potential type YSZ-based sensor will be reviewed, particularly for H_2 detection applications. After that, the utilization of metal oxides as the SE material for H_2 detection is also elaborated. Challenges and trends in H_2 sensor development will also be generally introduced in this chapter. The aims as well as the scope in each chapter of thesis are described at the end of this chapter.

1.1 Hydrogen Economy

Energy has always been an essential and integral component in sustaining our life. For centuries, human has been in constant search for energy sources. An energy carrier moves and delivers energy from its sources into a useable form for the energy user. Since the beginning of industrial revolution in the 18^{th} century, the energy carrier that has been used to accommodate our extensive daily activities is based mainly on fossil fuels, such as coal, petroleum and natural gas. This fact makes the exploitation of fossil fuel to produce energy become an important factor, particularly in shaping our human civilization. The rapid progress in industrial and scientific revolution has brought about a drastic advancement in many aspects from transportation, communication even to medical technology.

As an energy carrier, fossil fuel has been deemed to be unsustainable, predominantly due to the fact that they are depletable. Additionally, these are limited viable fossil fuel sources on earth [1], which sometimes could cause a geopolitical conflict between some countries who want to claim the ownership of the sources. Furthermore, the combustion of fossil fuel liberates large volumes of CO_2, which accounted as one of the green-house gases [2]. It could also affect the energy balance on earth which could force the global climate to change [3].

Considerable concerns and interest about finding an alternative energy carrier is also stem from the strong demand on fuel to support this ever increasing energy consumption [4]. This global energy consumption is expected to escalate continuously (Fig. 1.1), given the massive human activities combined with a constant increase in number of population, particularly in developing countries [5]. In stark contrast to these facts, the available reserves of fossil fuel are running out and cannot be balanced with the rate of exploration and the discovery of the new fossil fuel sources. The global

consensus to reduce and manage the green-house gases emissions which keep on rising, has also motivate to find a replacement of fossil fuel with a sustainable alternative.

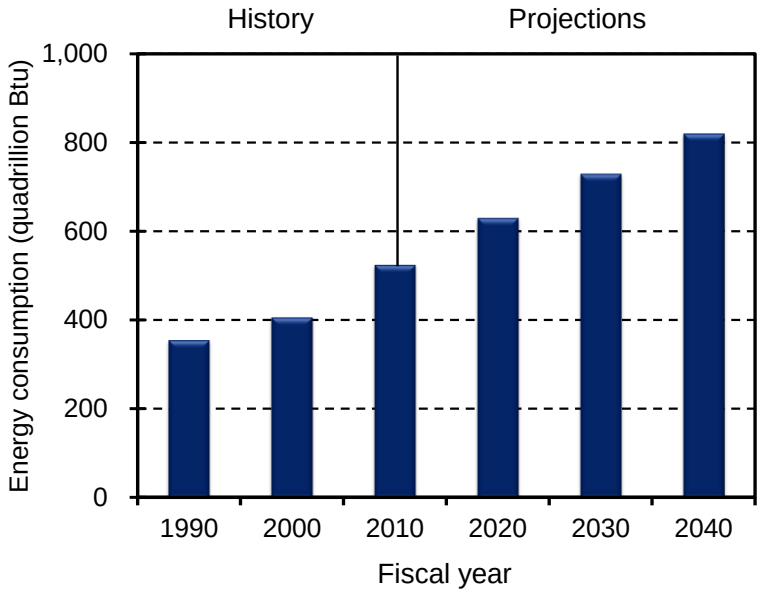

Figure 1.1 World energy consumption (FY 1990-2010) and the future projection of energy consumption (FY 2010-2040) (Source: Ref.[5], with permission from the US EIA)

Table 1.1 The comparison of energy per unit mass several fuels. (Reproduced from Ref.[8], Copyright 2005, with permission from Elsevier)

Fuel type	Energy per unit mass (J/kg)
H_2 liquid	141.90
H_2 gaseous	141.90
Natural gas	50.00
LNG	50.00
LPG	48.80
Gasoline	47.40
Jet fuel	46.50
Fuel oil	45.50
Biodiesel	37.00
Charcoal	30.00
Ethanol	29.90
Methanol	22.30

Of all the existing alternative energy sources and carrier, hydrogen (H_2) has been praised and proposed as one of the most sustainable energy carriers. H_2 can be produced from abundant source such as water [6]. The combustion of H_2 does not produce hazardous pollutant, since it only produces water (H_2O) which can be decompose again into H_2 and O_2 [7]. More importantly, as a gas, H_2 has a relatively higher (specific) energy content, when compared with other fuels (Table 1.1) [8], which makes H_2 becoming more attractive than other energy sources. Moreover, the fact that renewable energy sources such as wind or solar, cannot produce energy all the time made H_2 advantageous over these alternative energy sources, since H_2 production does not rely heavily on nature course. Although, H_2 gas is currently used primarily for manufacturing chemicals [9], a bright future is predicted for it, as an alternative energy carrier to replace the dominant fossil fuel for a transportation fuel. By the year 2050, an ideal H_2 economy is planning to be fully implemented [10], thus H_2 will be used to fuel transportation or to generate electricity and heat for industrial and residential use (Fig. 1.2).

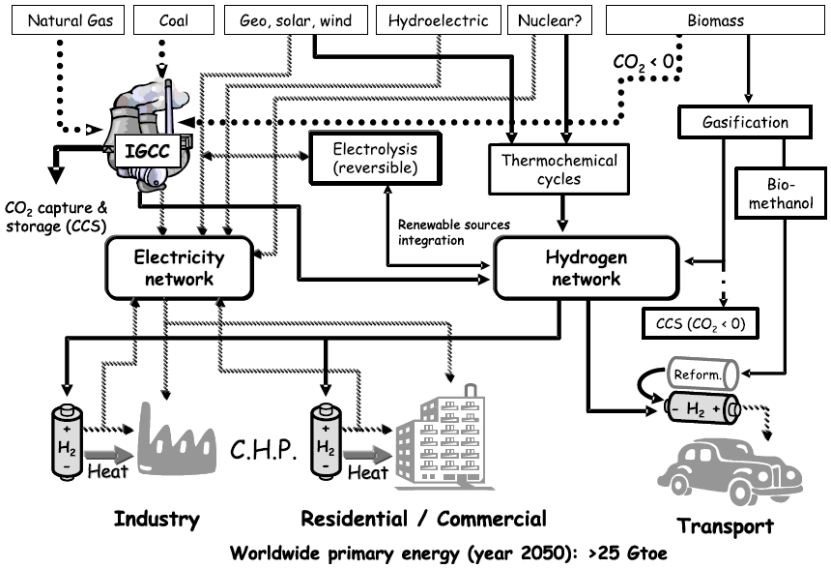

Figure 1.2 Illustration of the H_2 economy scenario in the future, when H_2 will be fully implemented as fuel. (Reproduced from Ref. [10], Copyright 2007, with permission from Elsevier)

To make this elegant theory of H_2 economy into reality, supporting infrastructures are required to be developed to assist H_2 production, storage and delivery. However, H_2 has low ignition energy (0.02 mJ) and the leakage of H_2 of about 4 vol.% (lower explosive limit/LEL) in air could easily create a conflagration [11]. H_2 explosion incidents, such as the space-shuttle Challenger back in 1986 [12] or at Fukushima power plant in 2011 [13] is enough to create reservations regarding the safety aspect of H_2 handling. Therefore, one of the largest obstacles in the transition from fossil fuel-based to H_2 economy is gaining and ensuring public trust regarding the safety aspect of H_2 utilization.

Since H_2 is odorless and colorless gas, it cannot be detected with human olfactory systems [14]. Given the numerous benefits coming from H_2 utilization, it is very important to develop a sensor that could detect the localized H_2 concentration. An H_2 sensor would be mostly valuable since it will alert H_2 users, once the localized H_2 concentration approaching a dangerous level. Therefore, a lethal incident can be prevented by having H_2 sensors installed in H_2-used facilities. Beside the ability to detect H_2 sensitively and rapidly, the sensor needs to be stable for long-term operation, and to have features such as low maintenance cost and simple operation.

1.2 Hydrogen sensing technologies

1.2.1 Conventional gas analyzer vs. solid-state gas sensor

The need for gas detection and monitoring devices also emerged from the raising awareness in maintaining a healthy and clean environment. Among the existing gas concentration analyzers, a solid-state gas sensor is one of the most versatile devices, due to its applicability to detect various gases for different applications. A solid-state gas sensor has been hailed as the best candidate for gas sensing applications, when

compared with even the traditional gas analysis instruments such as gas-chromatography (GC) or mass spectrometer (MS). GC uses a long column for gas component separation and a gas detector to identify each species [15]. MS analyzes gases, based on the typical spectra of each component that is resulted from the deflection of gas molecule in a magnetic field [16]. These conventional analytical instruments are not only expensive in both operation and maintenance, but also large in size (bulky) and require relatively complicated operating procedures.

A solid-state gas sensor can overcome the above-mentioned issues with respect to the traditional analytical instruments. In general, a gas sensor is a small-sized and portable sensing device. Compared with the traditional methods, the utilization of gas sensors also consumes less cost in operation as well as maintenance. Another important advantage of solid-state gas sensor is that it does not necessitate a sample preparation prior to sample analysis. This can make an in-situ or real-time gas measurement feasible to perform on site. With more than 30 years of development and commercialization [17], solid-state gas sensors have been proven to capable of providing a quick and accurate information of a particular target gas. Furthermore, a solid-state gas sensor is also has a stable performance for a long-term operation, even occasionally under challenging working conditions.

1.2.2 Solid-state H_2 sensor

In order to support the safe utilization of H_2 in various applications and infrastructures, an H_2 sensor requires to meet the following criteria:

1. High sensitivity to low H_2 concentration
2. Minor interfering signal from co-existing gases (high selectivity)
3. Long-term stability

4. Rapid response/recovery
5. Low maintenance cost
6. Simple operation
7. Portability

Solid-state gas sensors are the most suitable device to fulfill all those requirements. They have also been extensively studied and developed with different platforms for sensitive and selective H_2 detection, as follows:

a) Electrochemical

A typical solid-state electrochemical sensor generally consists of a sensing electrode and a reference electrode which are separated by a solid electrolyte. A third electrode (counter electrode) is often included into an electrochemical cell to control the performance of the sensing electrode. Based on the sensor operating principle, the main platform for electrochemical H_2 sensors can be classified into three types: amperometric, potentiometric and impedancemetric. Of all the three classes of electrochemical sensors, amperometric and potentiometric sensors have been widely studied, developed and even commercialized. In amperometric sensors, a biased voltage is applied to promote the electrochemical reactions that involved a target gas to occur and produce current, which is recorded as a sensing signal [18]. An example of amperometric sensors using three-electrode configuration (Pt-black as the electrode material) placed on a Teflon® substrate for selective and sensitive H_2 detection (Fig. 1.3)[19].

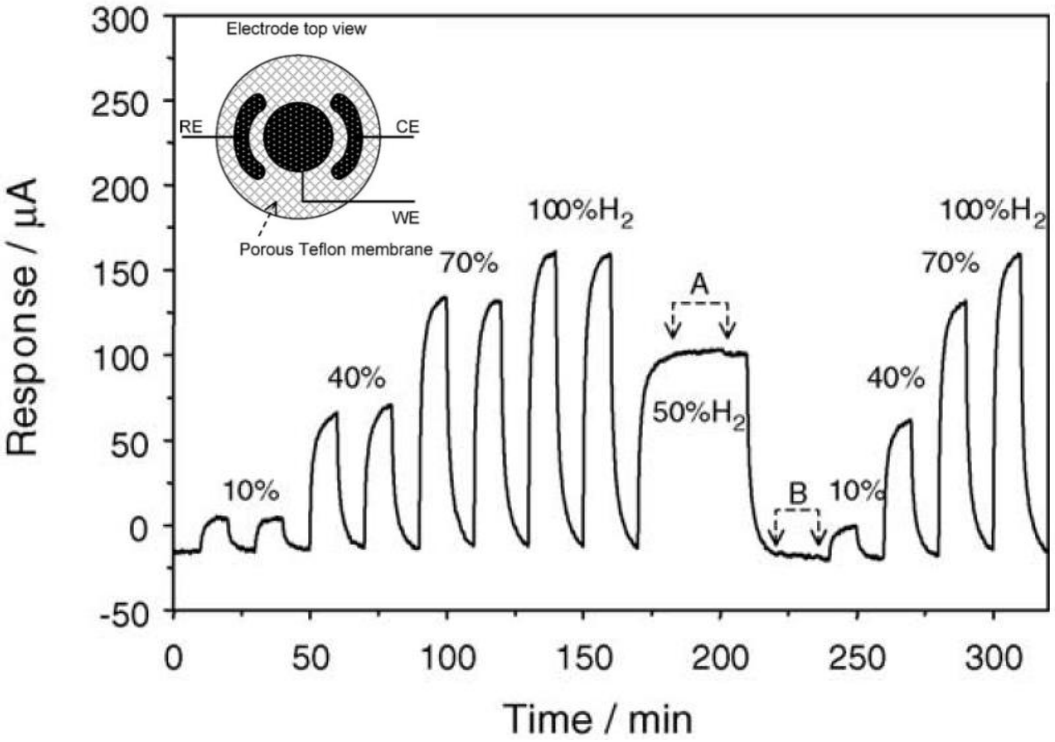

Figure 1.3 Response of an amperometric sensor to various H_2 concentrations mixed with CO and air. In region A, the gas mixture was 50%H_2/air with 1.5, 1, 2.5% CO (each for 15 min). In region B, the gas mixture was 5% CO/air. (Inset is the schematic view of the tested amperometric sensor with three electrodes on porous Teflon® membrane). (Reproduced from Ref.[19], Copyright 2005, with permission from Elsevier)

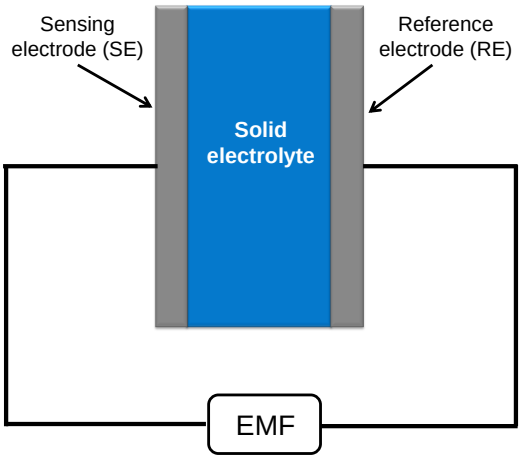

Figure 1.4 Schematic cell arrangement of the potentiometric sensor using solid electrolyte and sensing and reference electrodes.

Unlike amperometric sensors, a potentiometric sensor operates under zero-current or open-circuit conditions. The typical set-up for potentiometric sensor is given in Fig. 1.4. The potential change during exposure to target gas is generated by the electrochemical reactions at electrode/electrolyte interface and reaches a steady state [20], which is recorded as a sensing signal for potentiometric sensor. However, in the case of impedancemetric sensors, the change in impedance when the sensor exposed to target gas is recorded as the sensing signal. The poor long-term stability often restricts the application and development of this type of sensor [21].

b) Resistance

The basic setup of this type of sensor is relatively simple, where a metal oxide film is deposited on top of a ceramic substrate [22]. A resistance-based sensor measures the change in electrical properties (resistance or resistivity) of a sensing material upon the introduction of a target gas. The target gas will be adsorbed and interact with the surface of the sensing material which results in the change of the charge-carrier concentration. The charge carrier for *n*-type semiconductor is electron and for *p*-type semiconductor is hole [23]. The most popular resistance-based sensor is metal oxide (MOX) sensor which utilizes a wide band-gap semiconducting metal oxide as the active element for gas detection, such as tin oxide or zinc oxide. One example of sensitive and selective resistance-based H_2 sensor using TiO_2/PtO-Pt film is given in Fig. 1.5 [24].

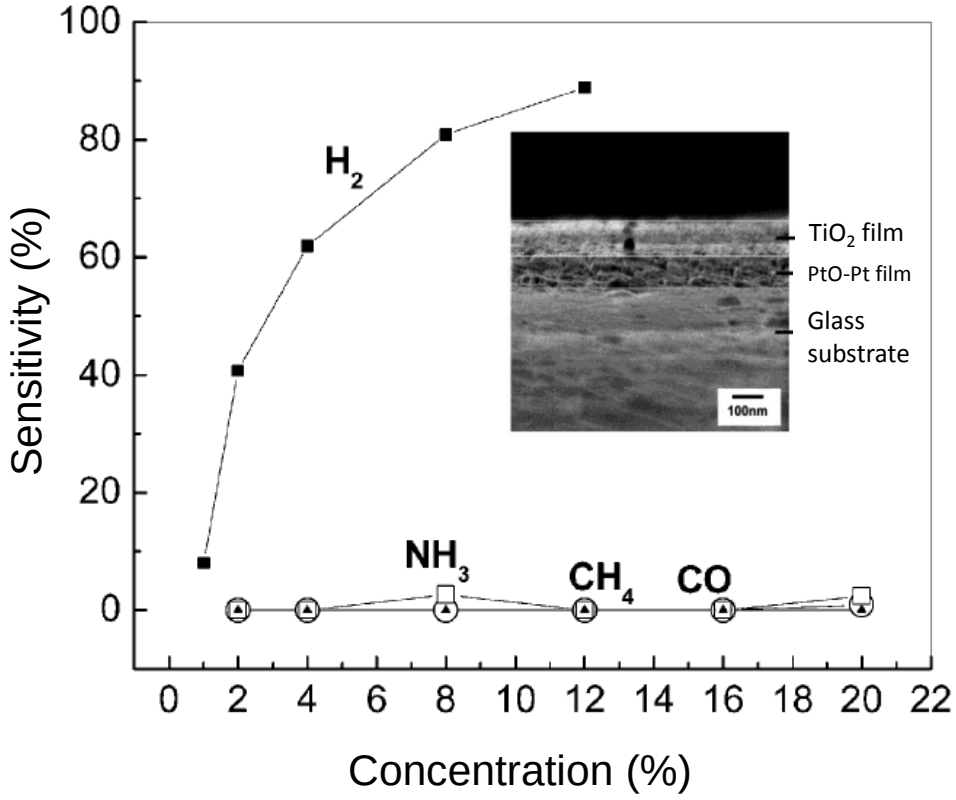

Figure 1.5 Sensitivity to different gases of a resistance-based sensor using TiO_2/PtO-Pt dual layer (inset is the HRSEM images of the cross-section of the double-layer sensing element on a glass substrate). (Reproduced from Ref. [24], Copyright 2002, with permission from the American Chemical Society)

c) Catalytic combustion

A Wheatstone-Bridge circuit is used to measure the sensing-signal output of the catalytic-combustion type sensor. The basic operation of this type sensor is based on the oxidation reaction of a combustible gas as the target gas. This reaction liberates thermal energy (heat) and then, the heat can change the temperature which causes the change in resistance of the sensing element. The change of resistance of the sensing element disrupts the balance (equilibrium state) of the Wheatstone-bridge. The change in voltage is then recorded as a sensing signal [25]. This sensor also known as a Pellistor-type sensor since the sensor using two coils that embedded in a "pellet" or ceramic bead [25].

An example of a catalytic combustion type sensor is given in Fig. 1.6, where Pt-γ alumina was utilized as the sensing element and γ-alumina as the reference element [26].

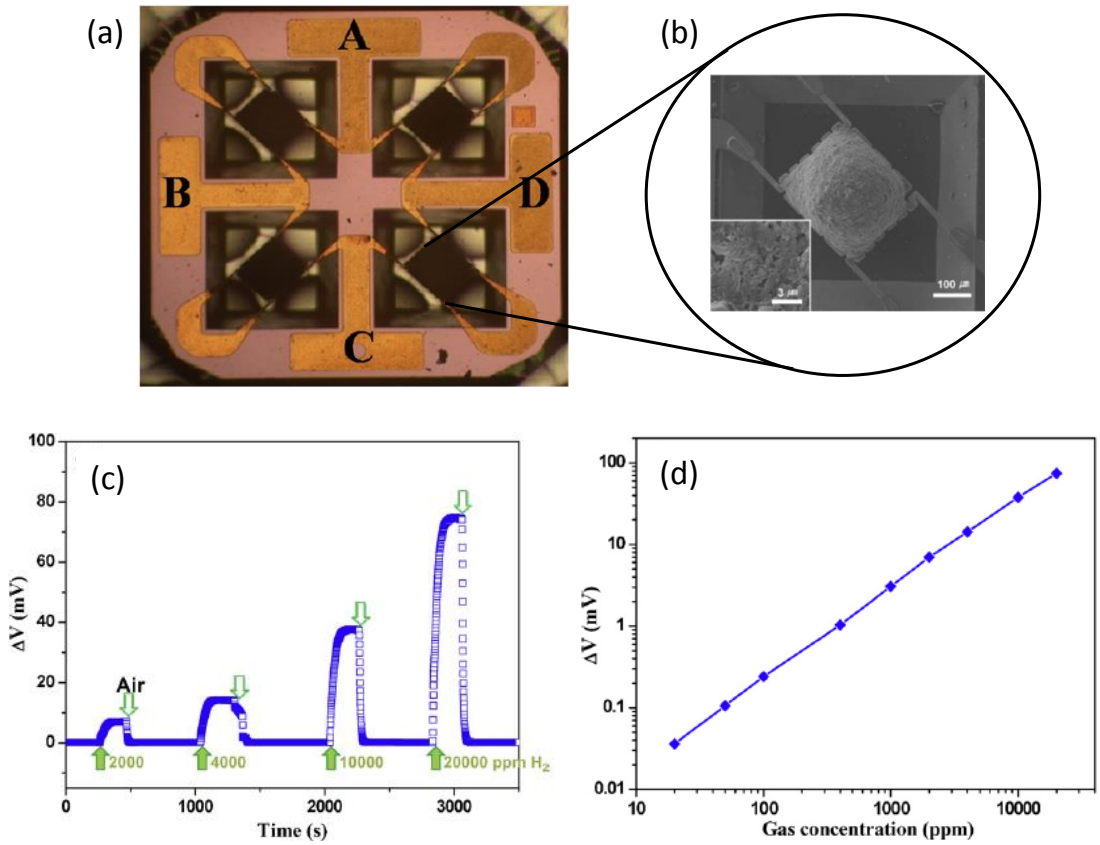

Figure 1.6 (a) A photograph of the catalytic-combustion type sensor and (b) the SEM images of the sensing layer. (c) The response transients to 20-20,000 ppm H_2 and (d) the dependence of sensitivity on H_2 concentration of the developed sensor. (Reproduced from Ref. [26], Copyright 2011, with permission from Elsevier)

d) Optical

Optical-type gas sensor measures the changes in optical properties (e.g. refractive index, absorption, reflectance, etc.) of a material when interacts with a particular gas [27]. The widely-used sensing element for an optical sensor is an optical fiber. Based on the detection principle, an optical sensor can be divided into seven types; absorbance

and reflectance, refractive index, photoluminescence, photothermal, photoacoustic, surface plasmon resonance (SPR) and chemiluminescence [28, 29]. An optical H_2 sensor is mostly based on thin films or noble metal and/or metal oxide coated onto an optical fiber. One advantage from the utilization of optical sensor is the low sensitivity to electromagnetic noise and the potential to detect multiple gases. Figure 1.7 shows one example of a typical fiber optic sensor, aiming at sensitive H_2 detection utilizing fiber optic coated with WO_3 and Pt [30].

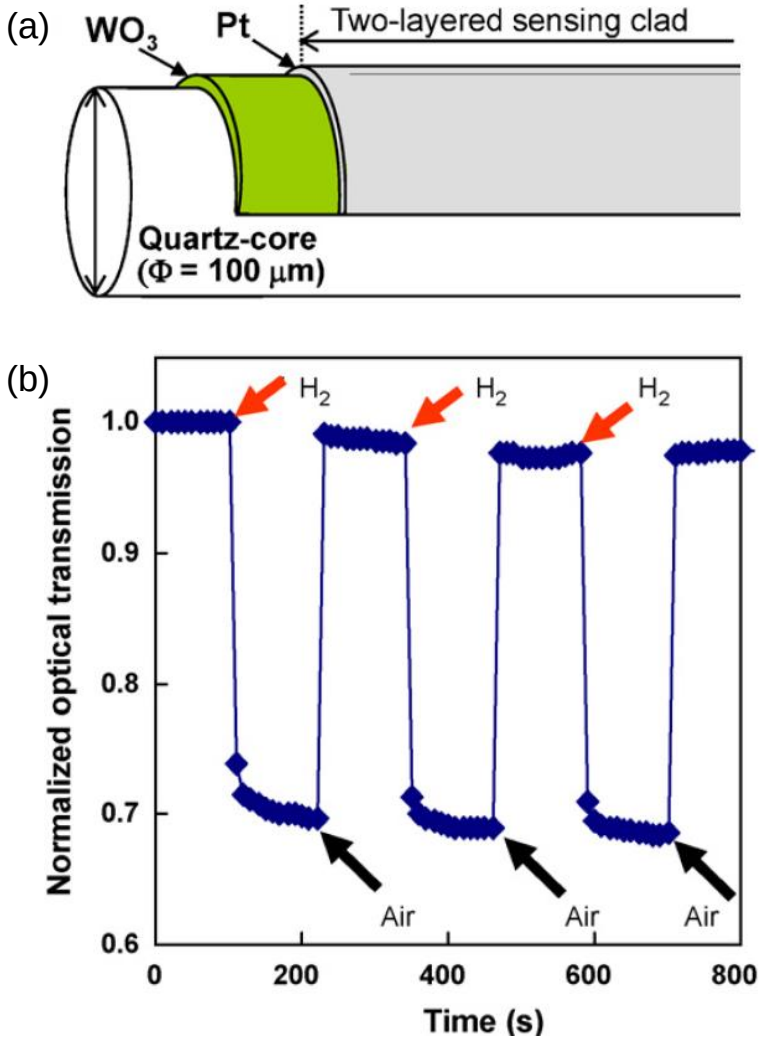

Figure 1.7 (a) Schematic view of a fiber optic sensor using WO_3 and Pt layer on quartz glass fiber and (b) real-time optical transmission change upon the introduction of 10 vol.% H_2/N_2 on the fiber. (Reproduced from Ref. [30], Copyright 2009, with permission from Elsevier)

e) Work function

A work-function type gas sensor ordinarily consists of layers of metal, metal oxide and semiconductor (MOS). A work function is essentially the minimum energy required to remove an electron from an electronic conductor to its non-bounded state [31]. The chemical reaction during the interaction of gas with the solid surface involves a charge transfer process which causes the changes in the work function. Experimentally, the change in work function which is manifested in the change in the electronic properties of the sensing material (such as voltage, resistance etc.) is recorded as a sensing signal [31]. Work-function type gas sensors can be classified into three types; metal-semiconductor (schottky) diode, meta-insulator-semiconductor transistor (MIFSET or MOFSET), and metal-insulator-semiconductor (MOS) capacitor. For H_2 detection, a H_2 sensitive metal is deposited onto an oxide placed on a semiconductor substrate [31]. Figure 1.8 shows an example of response transient to H_2 for a work function type (MOFSET) sensor with different treatment [32].

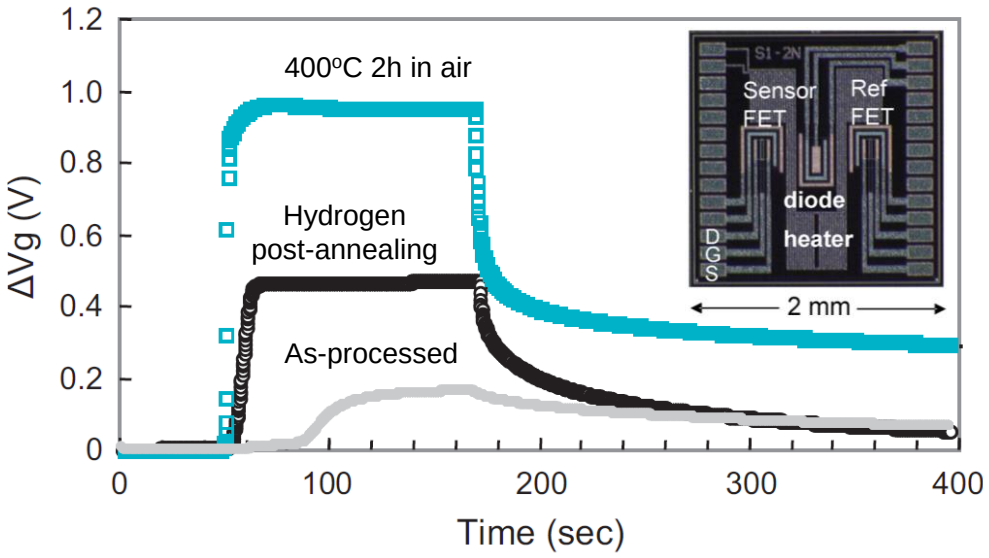

Figure 1.8 Response transient to 1000 ppm H_2 of a MOFSET sensor using as-fabricated chip, annealed at 400°C for 2 h in air and hydrogen post-annealing chip (inset is the photograph of the fabricated sensor chip). (Reproduced from Ref. [32], Copyright 2011, with permission from Elsevier)

f) Acoustics

The sensitivity of an acoustic-type sensor is generated from the interaction of a thin film with a specific gas molecule which causes a change in acoustic wave. The commonly-used thin film for acoustic sensor is a piezoelectric material [33, 34]. An acoustic type sensor can be categorized into three groups; quartz crystal microbalance (QCM), surface or bulk acoustic wave (SAW, BAW) and sound velocity. An example of H_2 sensing characteristic of a surface acoustic wave sensor, including the typical setup of an SAW sensor, is shown in Fig.1.9 [35].

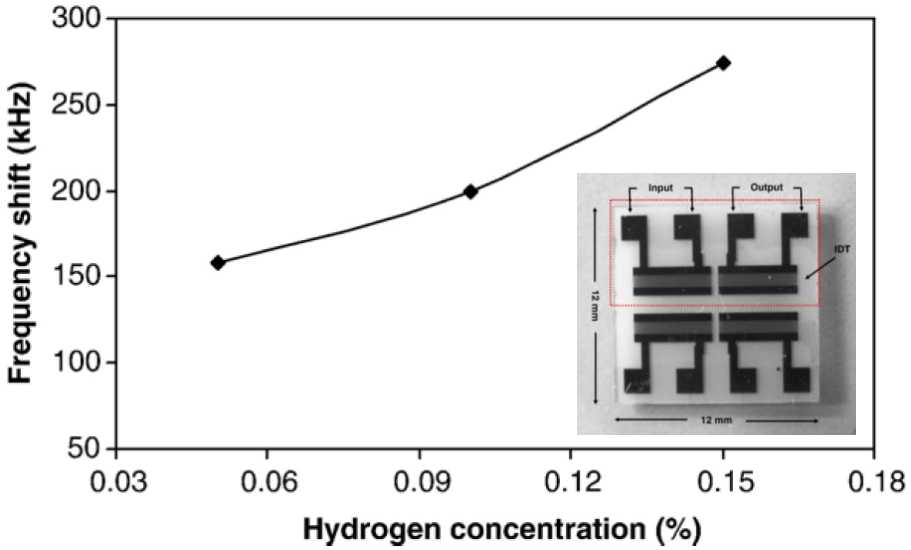

Figure 1.9 Dependence of sensitivity (frequency shift (kHz)) on H_2 concentration (%) for a surface acoustic wave (SAW) sensor using ZnO nanorods on ZnO/64°YX $LiNbO_3$ substrate (inset is the photograph of the fabricated SAW sensor with two sets of resonators). (Reproduced from Ref [35], Copyright 2007,with permission from Elsevier).

Interest and efforts in developing a high-performance solid-state H_2 sensor can be seen from the increasing number of published papers on that regard (Fig. 1.10). Some of the developed H_2 sensor using the various types of sensor that has been previously described is summarized in Table 1[26, 36-54]. It is seen from this table that most of the

reported H_2 sensors can only detect H_2 in a relatively high concentration and very few of them can detect H_2 at low concentration level.

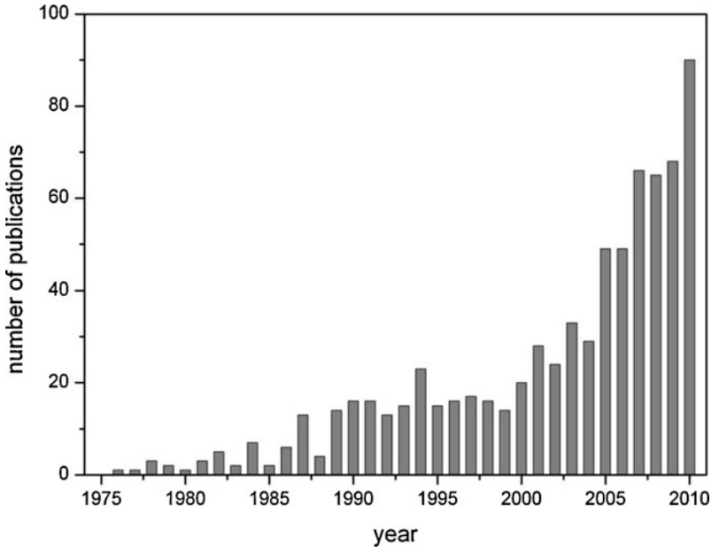

Figure 1.10 The number of published reports on the solid state H_2 sensor for the past three decades. (Reproduced from Ref [11], Copyright 2011, with permission from Elsevier)

Compared with other solid-state gas sensor, electrochemical gas sensor has been hailed as the most promising candidate for high-performance gas sensor. The advantages of electrochemical sensors include:

1) Capable of detecting very low concentration gas (high sensitivity)
2) Linear sensing signal output (good accuracy)
3) Relatively high life expectancy (excellent long-term stability)
4) Low power requirements
5) Simple operation, calibration and maintenance
6) Does not get poisoned by the tested gases
7) Less expensive than other gas sensing technologies

Electrochemical sensors have been proven as an attractive sensor technology for many

decades. The above-mentioned advantages makes electrochemical gas sensor received a lot of attentions from researchers or practitioners in the gas sensor field for hazardous gas detection development, including H_2 concentration monitoring.

Table 1.2 Comparison of sensing characteristic of various types of solid-state gas sensor for H_2 detection

Type of sensor	Sensing element	Temperature (°C)	Detection range	Ref.
Resistance	SnO_2-Co	120-480	40 ppm	[36]
Resistance	SnO_2	200-300	10-1000 ppm	[37]
Resistance	SnO_2+Pt	125	160-5000 ppm	[38]
Resistance	CuO	300	1- 6 vol.%	[39]
Resistance	Pt-WO_3	95-220	30-200 ppm	[40]
Electrochemical	ZnO/$CaZr_{0.9}In_{0.1}O_{3-\delta}$/Pt	700	50-500 ppm	[41]
Electrochemical	Pt(+Au mesh)/YSZ/Pt	550	10-400 ppm	[42]
Electrochemical	PTFE/Pt-Ru/Pt-C/Nafion	RT	560-11,500 ppm	[43]
Work function	Pt/β-Ga_2O_3/GaN	227	100-10,000 ppm	[44]
Work function	Pt/i-ZnO/GaN	RT	100-10,000 ppm	[45]
Work function	Pd/Au/pSiC & Pt/Au/pSiC	RT	10-40 ppm	[46]
Work function	Pd/SiO_2/n-Si/Al_2O_3	RT	1480-11,840 ppm	[47]
Work function	PMMA/In_2O_3-SnO_2	RT	600-15,000 ppm	[48]
Work function	Pd/Si (nanowire)/SiO_2/Si	RT	13-50,000 ppm	[49]
Catalytic	Pt-nanoparticles	150	0-10,000 ppm	[50]
Catalytic	Pt-γ-Al_2O_3	180	20-20,000 ppm	[26]
Optical	Pd/WO_3	RT	0.5-3 vol.%	[51]
Optical	Pd/Au	RT	1-4 vol.%	[52]
Acoustic	Pd/Au/AIN	RT	0.3-2 vol.%	[53]
Acoustic	CuPc+Pd/$LiNbO_3$-Y-Z	RT	0.5-3 vol.%	[54]

(RT : Room temperature)

1.3 YSZ-based potentiometric gas sensor

Among the existing electrochemical gas sensors, the YSZ-based electrochemical sensors have been long considered as the most practical one and widely studied. The advantages of the YSZ utilization as a solid electrolyte in gas sensing application are as

follows:

1) Chemically inert toward exhaust gas
2) Excellent thermal and mechanical stability
3) Superior ionic conductivity and negligible electric conductivity
4) Compatible for different operation conditions

Those advantages, particularly the excellent stability, make YSZ-based sensors considered as one of the potential candidates for high-performance gas sensors.

1.3.1 Equilibrium potential type YSZ-based oxygen sensor

The measurement of gas concentration using a solid electrolyte cell was emerged and started back in 1950s, during the work that was initially focused on measuring the potential difference (E_{cell}) of a gas with determined concentration using a potentiometric cell [55]. The success in the initial investigation using O_2 was followed by the success in estimating the gas partial pressure of other gases from observing the electromotive force (emf) of the cell [56]. This work later inspired further extensive research in the development of a solid-state gas sensor, including transducers that have a role in transforming the sensing signal into an electrical signal.

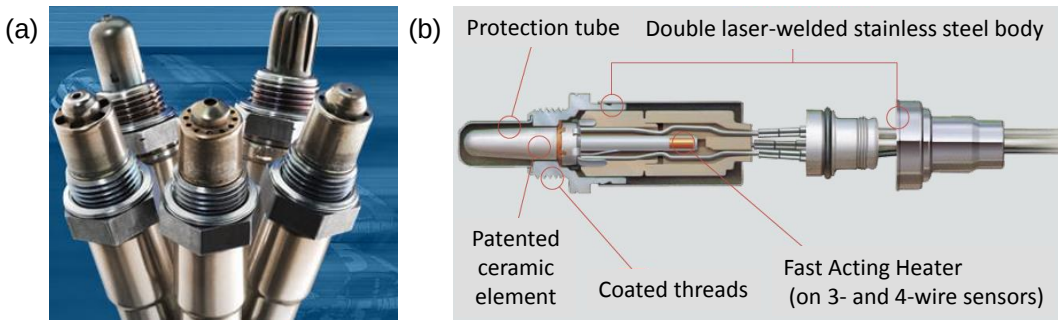

Figure 1.11 (a) Various commercial O_2 sensors and (b) the component of a thimble O_2 sensor for automotive applications. (Reproduced from Ref.[58], with permission from Bosch®)

The most successful commercialization of gas sensor is the utilization of YSZ as base material in O_2 sensor for automotive application (Fig. 1.11), which was initiated by Bosch in 1970s [57, 58]. The presence of an O_2 sensor in the engine is aiming to regulate the ratio of air to fuel around the stoichiometric conditions. A better engine performance, efficient fuel utilization and low hazardous-gases emission can be achieved by installing an O_2 sensor upstream and downstream of the three-way catalyst (TWC) [59].

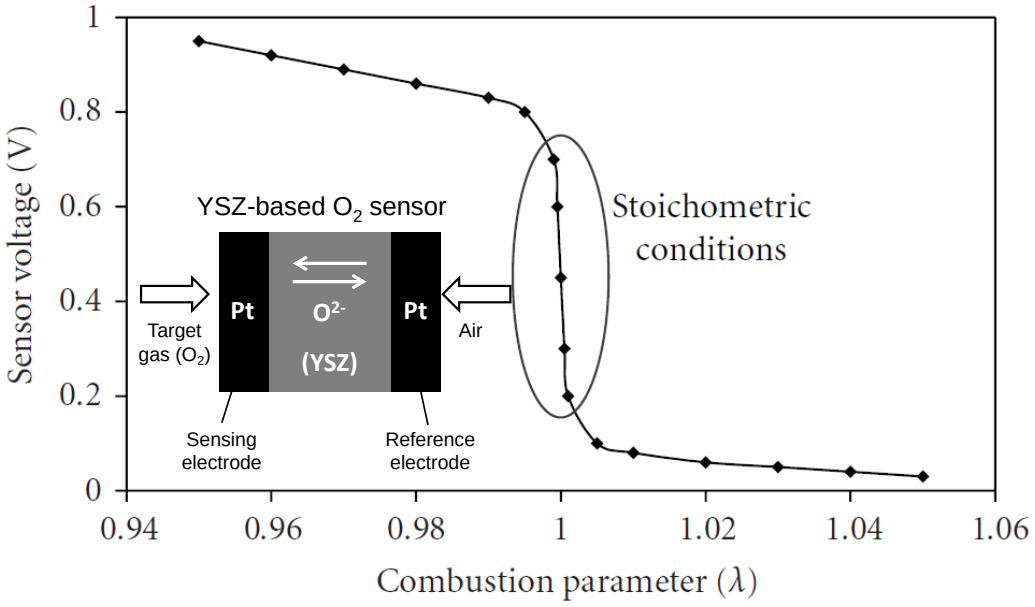

Figure 1.12 The relationship between the voltage of O_2 sensor and combustion parameters (λ) (Reproduced from Ref.[60]). (Inset is the typical cell arrangement of an O_2 sensor).

An O_2 sensor is essentially a potentiometric sensor that detects the change of O_2 concentration in the exhaust gas from a vehicle. In combustion engine system, λ refers to the comparison of the actual air/fuel (A/F) ratio with the stoichiometric A/F. Therefore, $\lambda>1$ means a rich O_2 region and $\lambda<1$ means a lean O_2 region. When $\lambda=1$, the air/fuel ratio reach a stoichiometric point where all the exhaust gas attain maximum conversion level (100%). This is the point where there is an abrupt change in O_2

concentration (from lean to rich), which can be detected as a large change in the sensor potential (Fig. 1.12) [60].

The typical and simplest arrangement of a potentiometric O_2 sensor is shown in the inset of Fig. 1.12, which consists of YSZ as the solid electrolyte that separate a porous sensing electrode and a porous reference electrode layer [61]. A potential difference between two electrodes in an O_2 sensor was developed when anodic (Eq. 1.1) and cathodic (Eq. 1.2) reactions reach an equilibrium state [62]. This potential difference is then recorded as a sensing signal.

Cathodic : $O_2 + 4e^- \rightarrow 2O^{2-}$ (1.1)

Anodic : $2O^{2-} \rightarrow O_2 + 4e^-$ (1.2)

Theoretically, the potential difference generated from a potentiometric O_2 sensor can be explained by using Nernst equation (Eq. 1.3) [63],

$$E = \frac{RT}{4F} ln \frac{P_{O_2}^2}{P_{O_2}^1} \quad (1.3)$$

Where R is gas constant (8.314 $J \cdot K^{-1} \cdot mol^{-1}$), T is the absolute temperature (Kelvin), F is Faraday constant (9.65 x 10^4 coulombs/mol) and 4 is the number of electrons participated in the electrochemical reactions. The Nernst equation clearly expressed that the generated potential correlates logarithmically with the change in gas concentration. When a charge transfer process takes place reversibly, the potential difference between the electrodes of the cell (E) is defined as an electromotive force (*emf*) [64]. Thermodynamically, when chemical reactions occur at both electrodes, the change in emf value correlates with the change in Gibbs free energy which equal to the work performed to transport an electric charge across one electric potential to another [65].

1.3.2 Mixed-potential type YSZ-based gas sensors

When two gas species exist in the sensing electrode, a thermodynamic equilibrium cannot be attained. Hence, the sensing characteristic of the YSZ-based sensor deviate from the ideal Nernst behavior, which defined as a non-Nernst behavior by Flemming [66]. The simultaneous presence of two gas species (oxygen and target gas) is postulated to cause the occurrence of two electrochemical reactions, namely cathodic reaction of O_2 (Eq. 1.1) and anodic reaction of the target gas (represented here as H_2 in Eq. 1.5) at the interface between sensing electrode and solid electrolyte [67].

$$\text{Cathodic} \quad : \quad O_2 + 4e^- \rightarrow 2O^{2-} \qquad (1.1)$$

$$\text{Anodic} \quad : \quad 2H_2 + 2O^{2-} \rightarrow 2H_2O + 4e^- \qquad (1.3)$$

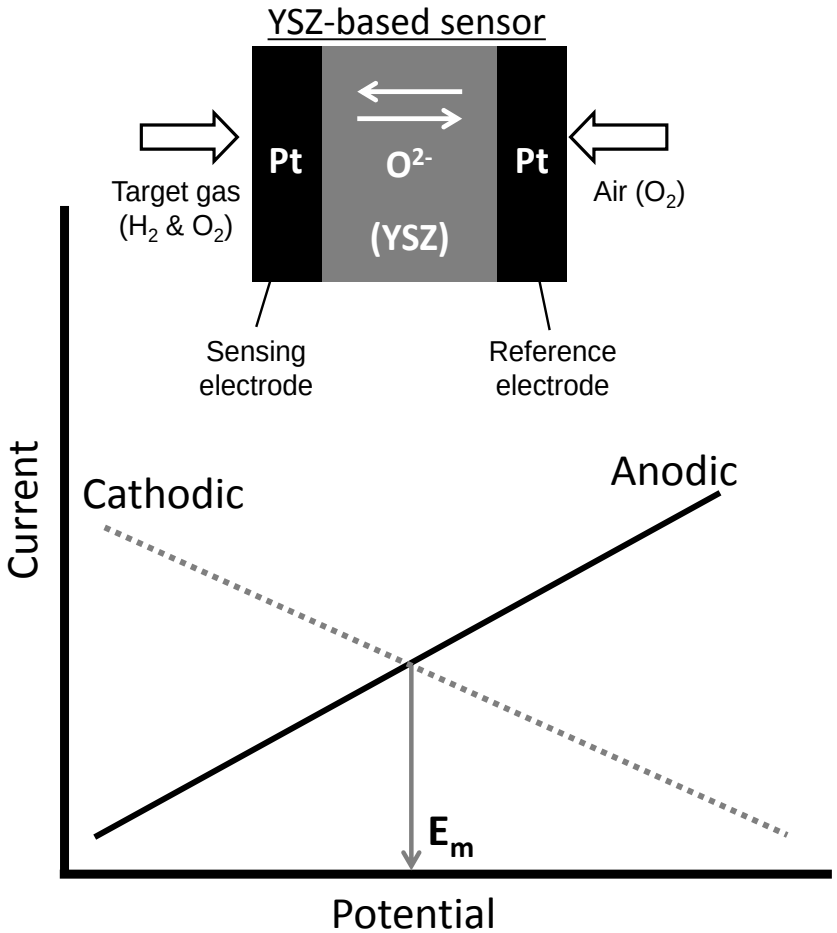

Figure 1.13 Mixed-potential theory elucidation using polarization curves. (Inset is the typical setup for a mixed-potential type YSZ-based sensor).

The cell potential can be established when each electrochemical reaction occurs at the same rate. Since the sensing electrode favors the anodic reaction of a reducing gas as the target gas rather than the cathodic reaction of O_2, the resulting cell potential becomes more negative [68].

Mathematically, this phenomenon can be elucidated by the mixed potential model using polarization (current-voltage) curves [69]. The sensitivity is represented by the intersect point between anodic and cathodic curves defined as the mixed potential (Em) of a sensor (Fig. 1.13). Figure 1.14 illustrates the sensing mechanism of an YSZ-based mixed potential type sensor in a simplified form. A typical mixed-potential type sensor would be consisting of a sensing electrode that exposed to the target gases, a reference electrode that exposed to the reference gas (air) and YSZ as a solid electrolyte that separate them (Fig. 1.14 (a)). As can be seen here, the electrochemical reactions will occur at the interface between sensing electrode and YSZ, which often called the triple-phase boundary (TPB) [70, 71]. The term “TPB” itself refers to the point where the solid electrolyte, sensing electrode and gases involved in the electrochemical reactions are connected (Fig. 1.14 (b)) [71]. Prior to undergoing electrochemical reactions, the target gas will be naturally oxidized within the sensing electrode layer (heterogeneous catalysis) (Fig. 1.14 (c)) [72]. Hence, the catalytic activity towards the heterogeneous reaction will control the percentage of gases capable of reacting at TPB. Therefore, the overall sensing performance of a mixed-potential type sensor would be largely determined by the type of the sensing electrode material, the fabrication process of the sensing electrode as well as the operational conditions of the sensor.

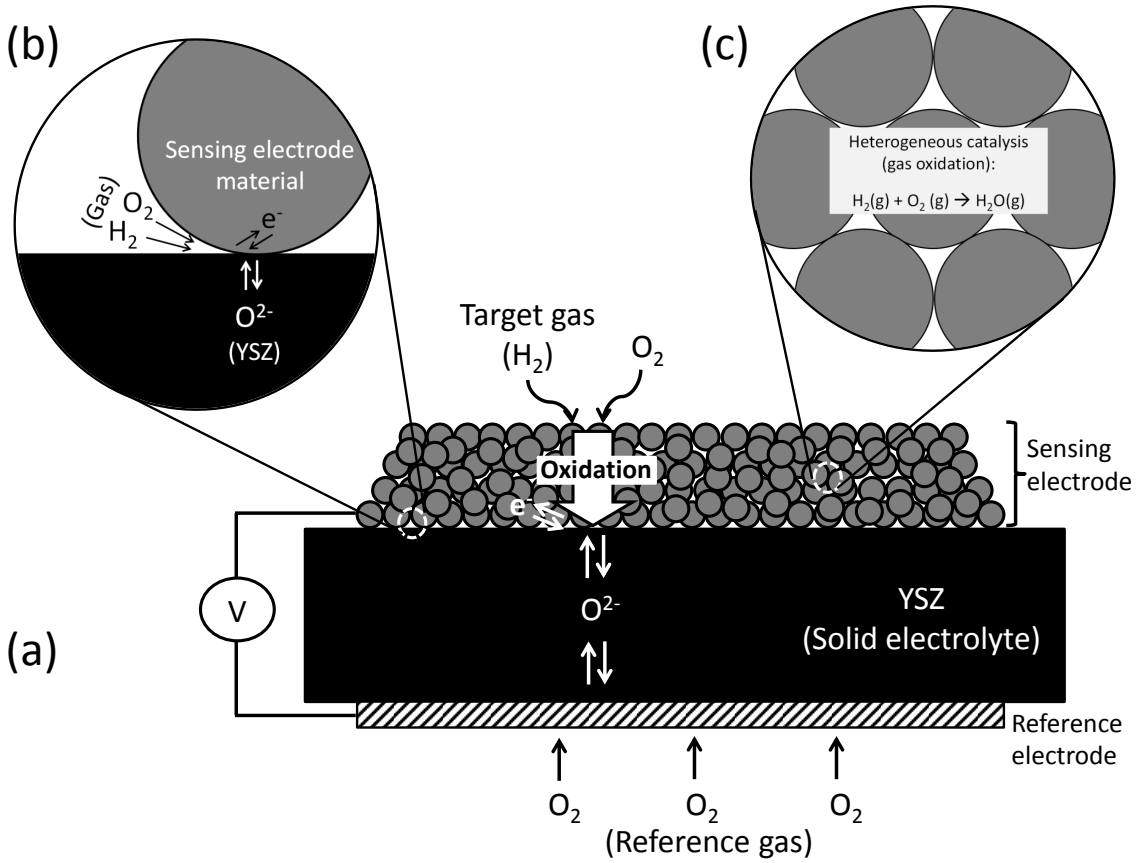

Figure 1.14 (a) Simplified illustration of the sensing mechanism of a mixed-potential type YSZ-based sensor, (b) illustration of the electrochemical reactions at the triple-phase boundary (TPB) and (c) the heterogeneous catalysis of the target gas at the sensing layer.

1.3.3 Sensing electrode materials for mixed-potential type YSZ-based sensor

Since the sensing signal generation of a mixed-potential type sensor is governed by the electrochemical reactions and the heterogeneous catalysis, the role of a sensing electrode material is highly pivotal in determining the sensing performance of the sensor. Due to the contradictive role of the two governing reactions (gas phase reactions and electrochemical reactions) in mixed-potential type sensor, it is important to have a sensing electrode material that has low catalytic activity to heterogeneous catalysis, low catalytic activity to the electrochemical reaction of O_2 and high catalytic activity to the

electrochemical reaction of a target gas.

Noble metals such as platinum (Pt) and gold (Au) have been used extensively as the sensing electrode material for YSZ-based sensors, due to its excellent catalytic properties that improved the sensing characteristics [73]. However, the high cost of noble metals has motivated the search for the replacement of noble metals with any other materials having equally or similarly excellent catalytic properties but with lower cost. More importantly, the sensing electrode material has to be stable for long-term operation under challenging environment conditions.

This search to substitute for the expensive noble metals leads to semiconducting metal-oxide sensing-electrode materials. The assorted structure and composition of semiconducting metal oxides are allowing them to posses various desirable catalytic properties, and hence the utilization of metal oxides as a prospective candidate for gas sensing applications seems to be an attractive idea. In general, metal oxides exist in the wide spread form of insulator to metal. Based on the electronic configuration, metal oxides can be divided into the following groups [74]:

1. Transition metal oxides (TiO_2, V_2O_5, Cr_2O_3, Mn_2O_3 etc.)

   Oxides in this group generally exist in more than one oxidation states, which are consequently relatively easy to be reduced and oxidized. These oxides have been used extensively as a sensing electrode material for YSZ-based sensor.

2. Non-transition metal oxides which can be divided into two sub-groups:

   (a) Pre-transition metal oxides (Al_2O_3 etc.).

   Since oxides in this group are difficult to be reduced or oxidized, they are expected to be quite inert. Hence, these oxides are rarely used as a sensing material.

   (b) Post-transition metal oxides (ZnO, SnO_2 etc.)

Given the electronic structure of oxides in this group (full *d* orbital), they can be reduced but not oxidized. This makes oxides in this group become alternative choices for gas sensing material.

These wide range electronic properties of metal oxides lead to different catalytic properties, and hence bring many possibilities for gas sensing applications. Furthermore, relatively lower production cost for metal oxides makes the sensor using metal oxides as SE more promising, particularly from sensor commercialization point of view. Thus, the sensing properties of sensors using semiconducting metal oxides in the form of thin or thick films have been examined extensively. Not only as a gas sensitive material, metal oxides occasionally have been used as a supporting material for metal catalyst [75]. Figure 1.15 is an example of different H_2 sensitivity generated from different types and different structures of metal oxides used as the SE materials, in comparison with metal (like Ag) as SE for the mixed-potential type YSZ-based sensors [76]. Among the various SE materials, SnO_2 gave the highest sensitivity to H_2 (Fig. 1.15) [76].

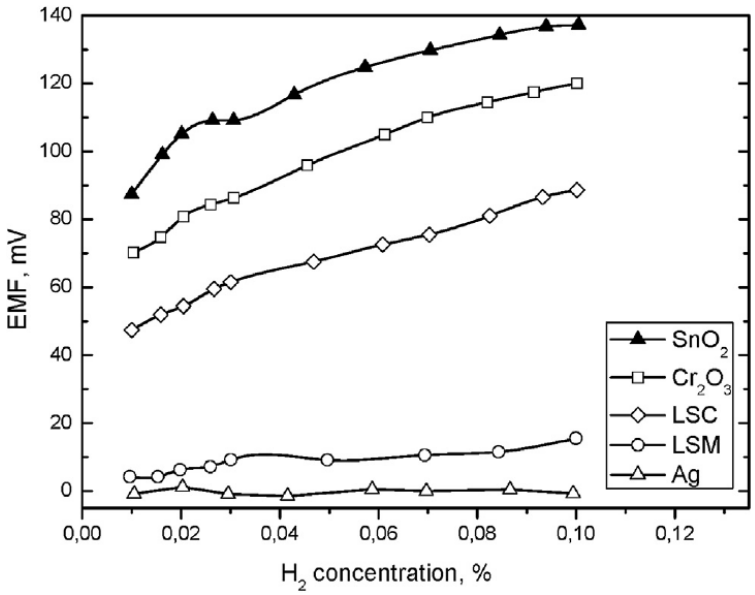

Figure 1.15 Dependence of sensitivity on H_2 concentration for YSZ-based sensors using each of different SE materials. (Reproduced from Ref.[76], Copyright 2013, with permission from Elsevier).

1.4 H_2 detection by mixed-potential type YSZ-based sensors

So far, most of YSZ-based sensors are aimed to detect exhaust gases such as hydrocarbons or NOx. However, due to its promising long-term stability, the potential of YSZ-based sensors to function as a H_2 detector has been studied and investigated for the past decade. Since the sensing signal generation of a YSZ-based sensor is governed by the balanced rates between the electrochemical reactions and the gas-phase reactions, most of approaches focused on controlling these reactions by exploring the suitable sensing electrode material.

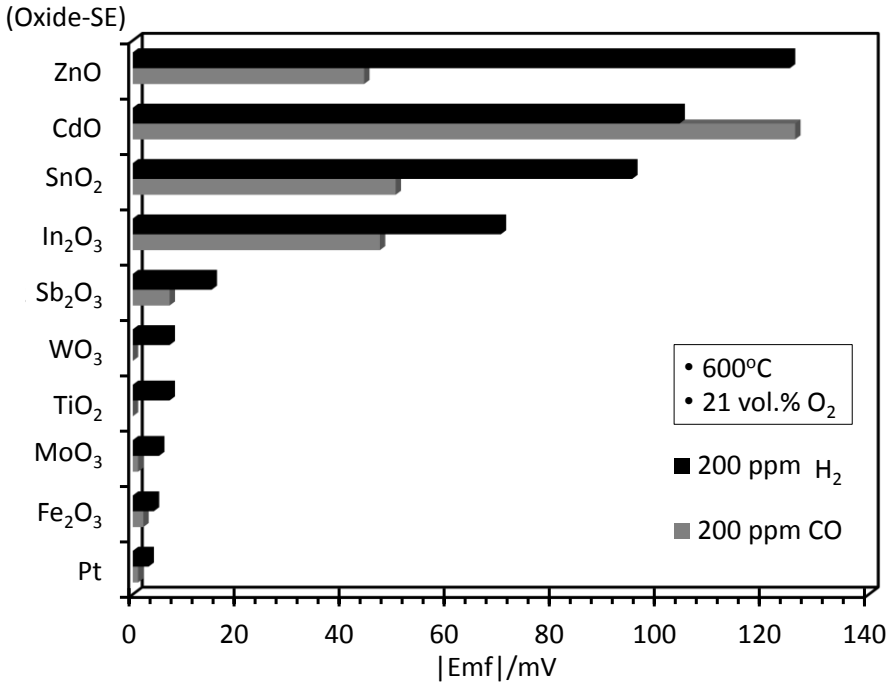

Figure 1.16 Sensitivity toward H_2 and CO for YSZ-based sensors using various metal oxides as a sensing electrode material. (Adapted from Ref.[81], Copyright 1998, with permission from Elsevier).

Initially, metals and alloys have been tested as the prospective SE to detect H_2 sensitively and selectively [77-80]. As a replacement for metals and alloys for SE material, Miura et al has investigated the utilization of various single oxides as an SE

material for YSZ-based H_2 sensors in tubular configuration (Fig. 1.16). Oxides such as ZnO and SnO_2 were reported to generate higher response toward 200 ppm H_2 in air, when compared with other examined oxides [81]. However, in accompany to the high H_2 sensitivity, the sensor using the oxides-SE (ZnO or SnO_2) was also sensitive to CO [81].

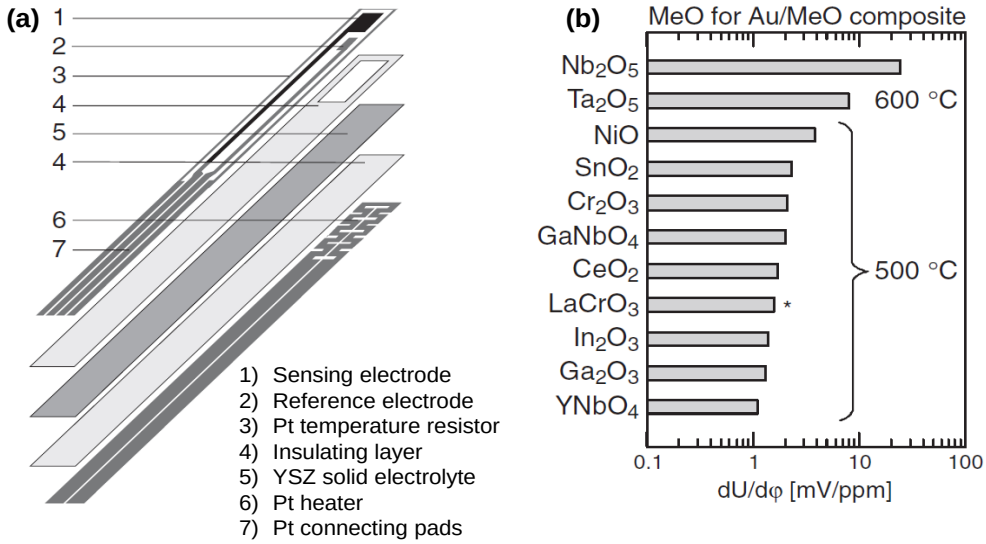

Figure 1.17 (a) Construction of the developed YSZ-based sensor and (b) H_2 sensitivity of the YSZ-based sensor using Au with different metal oxide addition. (Reprinted from Ref.[82], Copyright 2006, with permission from Elsevier).

Metal oxides were also often used as a component in a composite SE material. Figure 1.17 shows an example of an attempt to search for H_2 sensitive material by mixing different metal oxides into Au. In this case, Nb_2O_5 and Ta_2O_5 generated higher H_2 sensitivity when compared with other metal oxides, even at different temperature [82]. Interestingly, similar finding which shows that Ta_2O_5 exhibited highest H_2 response compared with other oxides has also been reported by Hibino et al. who developed YSZ-based sensors using metal oxide covered with Au net [83]. This high response to H_2 is also followed by higher response to other gases such as C_3H_6 and CO

[83]. Furthermore, detail elucidation on the sensing mechanism of this sensing performance of this sensor is yet to be reported.

Aside from being a single oxide or composite, oxide-based solid solution has also been employed and tested as SE for mixed-potential type sensor. Figure 1.19 (a) shows another endeavor in developing YSZ-based sensor using indium tin oxide/tin-doped indium oxide (ITO) as a sensing electrode and Ag as a reference electrode in planar configuration [84]. Despite the quick and relatively sensitive response to H_2, this sensor

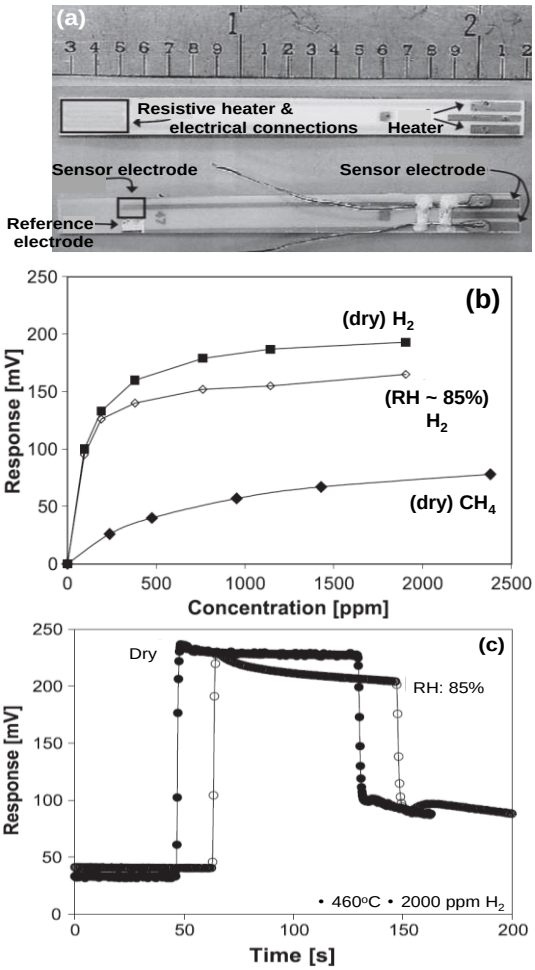

Figure 1.19 (a) The setup of the developed YSZ-based sensor, (b) H_2 and CH_4 concentration dependence on sensitivity and (c) H_2 response transients of the developed sensor in dry and wet condition. (Reproduced from Ref.[84], Copyright 2004, with permission from Elsevier).

can only distinguish H_2 from H_2O and CH_4. This would limit the utilization of the sensor on particular application.

While most research on YSZ-based H_2 sensors devoted in improving the sensitivity and response time by finding an appropriate sensing performance, the different sensing construction was also attempted and investigated, aiming at sensitive and selective H_2 detection. As shown in Fig. 1.18 (a), a planar YSZ-based sensor was developed by using ITO as the sensing electrode and Pt as a reference electrode [85]. The unique point of this design is the utilization of a dense sensing electrode and porous YSZ as a solid electrolyte as opposed to the typical type of YSZ-based sensor which employed dense YSZ and porous SE. Such a construction is aimed to reduce the counter-productive effect of heterogeneous catalysis. This sensing device has also been proven to be capable of generating sensitive response to H_2 with quick response (3-7 s), while the selectivity remains to be unsatisfactory (Fig. 1.18 (b))[85] .

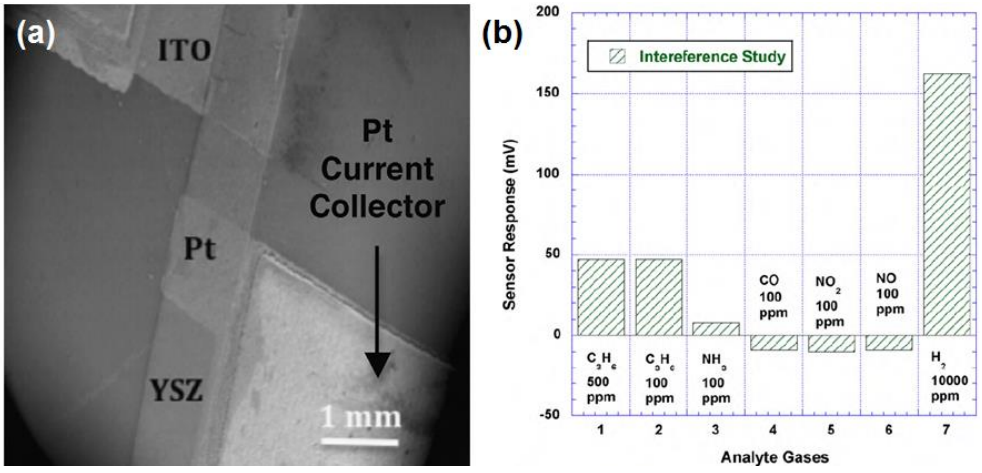

Figure 1.18 (a) SEM images of the YSZ-based sensor using ITO-SE and Pt-RE and (b) the cross-sensitivity of the developed sensor to different gases. (Reprinted from Ref.[85], Copyright 2010, with permission from Elsevier).

Based on these reported results, considerable success and progress have been made predominantly with regards to sensitivity and response time. However, since excellent selectivity is also a pivotal feature that defines a high performance mixed potential type YSZ-based sensor, then developing a highly sensitive and selective H_2 sensor is also equally important, particularly for the future implementation of H_2 economy scenario.

1.5 Challenges and trends in solid-state H_2 sensor

Excellent sensitivity, high selectivity, rapid response/recovery, long-term stability and low fabrication cost as the factors that defined a high performance sensor, will remain to be the main target of H_2 sensor research in the future. There is a general aspiration to miniaturize or simplify the sensor construction in planar configuration to promote the utilization of YSZ-based sensor in wider application. The miniaturization of the YSZ-based sensor will eliminate the reference-sensing gas separation, which commonly deployed in the standard design of a YSZ-based sensor. Modifying this standard design has been one of the approaches that pose some issues, since with different design and construction occasionally give an adverse effect to the sensing characteristics.

Extensive explorations have also been devoted in finding a sensing electrode that can fulfill those requirements for an excellent sensor. In spite of the strong necessity to miniaturize the sensor, finding a suitable sensing electrode material would be another challenge in H_2 sensor development. Broad varieties of electronic and chemical properties of metal oxides have opened many possibilities for structures manipulations and modifications, so the desirable sensing performance can be obtained.

Additionally, nanostructured metal oxide will be another prospective candidate for H_2 sensing material of YSZ-based sensors. The nano dimension of a nanomaterial is

expected to bring many attractive chemical and electrical properties which will be beneficial for the developed sensor. However, since the YSZ-based sensors can only functioned at relatively high temperature (approximately 400^{o}C), the stability of nanomaterial at high temperature is the challenge that need to be addressed for future YSZ-based sensor development. Greater control over micro and nanostructure of the sensing electrode material would also attract great interest in the sensor technological advancement in the future. Therefore, selection, design and processing the sensing electrode material are one of the key elements in gas sensor research and development.

Table 1.3 Examples of the reported mixed-potential type YSZ-based H_2 sensors.

Sensor configuration (RE/YSZ/SE)	Operating temperature (^{o}C)	Detection range (ppm)	Cross sensitivity examined	Ref
Pt/YSZ/Pt-Cu	550	0-10,000	CO	[80]
Pt/YSZ/Mo	550	0-10,000	CO	[80]
Pt/YSZ/$La_{0.8}Sr_{0.2}CrO_3$	1000^{o}C	500	C_3H_6 & C_3H_8	[83]
Au-$LaMnO_3$/YSZ/TbYSZ-Au	600	0-500	C_3H_6 & CO	[83]
Pt/YSZ/In_2O_3	600	0-500	C_3H_6 & CO	[86]
Pt/YSZ/In_2O_3(+ 0.1% MnO_2)	600	0-500	C_3H_6 & CO	[87]
$LaMnO_3$/YSZ/$LaMnO_3$-Al_2O_3(1.5%Pt)	400-500	2000	CO	[88]
Pt mesh-Pt/YSZ/ZnO-Pt mesh	450-600	50-500	-	[89]
Pt/YSZ/Pt	150-200	0-40,000	-	[90]
Pt/YSZ/Pt/CuO-ZnO	415-500	0-1,400	-	[91]

Despite the importance in having a sensitive sensing material with rapid response, the ability of the sensor to distinguish the target gas among various existing interfering gases is also equally important to avoid false signal generation. However, among the YSZ-based H_2 sensors reported, a sensor that can detect H_2 sensitively and selectively is rare. As can be seen from Table 1.3, hydrocarbon (C_3H_6 and C_3H_8) and CO gases are the main interfering gases that may override H_2 signal of a mixed-potential type YSZ-based

sensor [80, 83, 86-91]. Therefore, a mixed-potential type YSZ-based sensors, that are not only capable of exhibiting sensitive response to H_2, but also a highly selective one, is of the utmost importance not only for the whole H_2 economy scenario, but also for wider applications that involved H_2. Furthermore, while the basic principle of a mixed-potential type sensor has been established, a deeper insight and detailed elucidation on the H_2 sensing mechanism are yet to be revealed.

The emerging hydrogen economy concept would make development of a highly selective and sensitive H_2 sensor a great interest and highly important. In addition to this, insight into H_2 sensing mechanism will be useful not only people who work for gas sensor but also for other researcher or practitioners who study various H_2 applications

1.6 Aim and scope of the study

In the light of developing a high performance H_2 sensor, the research presented in this thesis is aiming at developing a higly sensitive and selective mixed-potential type YSZ-based H_2 sensor using metal oxide as the base material for the sensing electrode. Different methods to improve the selectivity toward H_2 is particularly proposed in this thesis.

The content of this thesis will be divided into two parts. The first part of the thesis will be focused on SnO_2 as the base SE material and how to improve the selectivity of the sensor using SnO_2-SE. Combined-type sensor is proposed as one of the effective way to improve selectivity. Afterward, another strategy in improving the sensor selectivity was also introduced by enveloping the SE layer with a catalyst layer to selectively oxidise the unwanted gases. Second part of the thesis will be covering the novel Zn-Ta-O oxide as a new H_2 sensitive material. The H_2 selectivity is attempted by optimizing the fabrication process and also via long-term aging process.

In **Chapter 2**, SnO_2 is chosen as an H_2 sensitive material. An attempt to improve selectivity of the sensor is proposed by pairing a SnO_2-based-SE with a counter electrode that can cancel out the sensing signal of the interferring gases.

Chapter 3 explains the new strategy for improving the selectivity of a mixed-potential type sensor using SnO_2-based SE. A novel design using an additional catalyst layer covering the sensing elecrode is proposed in this chapter.

In **Chapter 4**, ZnO is introduced as the base material for H_2 sensor. Ta_2O_5 addition to ZnO is propose as a method to improve the sensitivity of the sensor using ZnO-SE. The selectivity and sensitivity optimization of the sensor using Zn-Ta-O-based-SE will be attempted by controlling the sintering temperature during the fabrication process.

In **Chapter 5**, another Zn-Ta-O-oxide, namely $ZnTa_2O_6$, is introduced as a H_2 sensitive material. The sensing characteristic of the sensor using $ZnTa_2O_6$-based-SE before and after long-term aging will be evaluated and eloborated here.

Chapter 6 covers the aging mechanism in enhancing the sensing characteristic of the sensor using $ZnTa_2O_6$-based-SE, which is elucidated by series of experiments. The results from XRD, SEM, XPS and polarization curve measurements are analyzed and the corresponding effect on sensing characteristic of the sensor is also examined.

In **Chapter 7**, a summary of this thesis including prospect for future research topic will be introduced.

References

[1] S. Shafiee, E. Topal, *Energy Policy*, 37(2009) 181-9.

[2] L. Chiari, A. Zecca, *Energy Policy*, 39(2011) 5026-34.

[3] T.J. Crowley, *Science*, 289(2000) 270-7.

[4] U.E.I.A. (EIA), International Energy Outlook 2013 with Projections to 2040, *International Energy Outlook 2013*.

[5] K. Goldewijk, *Popul Environ*, 26(2005) 343-67.

[6] T. Nakamura, *Solar Energy*, 19(1977) 467-75.

[7] H. Kato, K. Asakura, A. Kudo, *Journal of the American Chemical Society*, 125(2003) 3082-9.

[8] A. Midilli, M. Ay, I. Dincer, M.A. Rosen, *Renewable and Sustainable Energy Reviews*, 9(2005) 255-71

[9] R. Ramachandran, R.K. Menon, *International Journal of Hydrogen Energy*, 23(1998) 593-8.

[10] G. Marbán, T. Valdés-Solís, *International Journal of Hydrogen Energy*, 32(2007) 1625-37.

[11] T. Hübert, L. Boon-Brett, G. Black, U. Banach, *Sensors and Actuators B: Chemical*, 157(2011) 329-52.

[12] T. Pinch, How Do We Treat Technical Uncertainty in Systems Failure? The Case of the Space Shuttle Challenger 1, in: T. Porte (Ed.) Social Responses to Large Technical Systems, Springer Netherlands1991, pp. 143-58.

[13] K. Hirose, *Journal of Environmental Radioactivity*, 111(2012) 13-7.

[14] Y.S.H. Najjar, *International Journal of Hydrogen Energy*, 38(2013) 10716-28.

[15] P. Marriott, R. Shellie, *TrAC Trends in Analytical Chemistry*, 21(2002) 573-83.

[16] R. Aebersold, *Nature*, 422(2003) 198.

[17] W.C. Maskell, *Solid State Ionics*, 134(2000) 43-50.

[18] Y. Tan, T.C. Tan, *Sensors and Actuators B: Chemical*, 28(1995) 113-21.

[19] Y. Chao, S. Yao, W.J. Buttner, J.R. Stetter, *Sensors and Actuators B: Chemical*, 106(2005) 784-90.

[20] S. Zhuiykov, *Sensors and Actuators B: Chemical*, 119(2006) 456-65.

[21] G. Korotcenkov, B.K. Cho, *Sensors and Actuators B: Chemical*, 156(2011) 527-38.

[22] G. Korotcenkov, *Sensors and Actuators B: Chemical*, 121(2007) 664-78.

[23] N. Yamazoe, *Sensors and Actuators B: Chemical*, 5(1991) 7-19.

[24] X. Du, Y. Wang, Y. Mu, L. Gui, P. Wang, Y. Tang, C*hemistry of Materials*, 14(2002) 3953-7.

[25] D.W. Dabill, S.J. Gentry, P.T. Walsh, *Sensors and Actuators B:Chemical*, 11(1987) 135-43.

[26] E.-B. Lee, I.-S. Hwang, J.-H. Cha, H.-J. Lee, W.-B. Lee, J.J. Pak, et al., *Sensors and Actuators B: Chemical*, 153(2011) 392-7.

[27] C. McDonagh, C.S. Burke, B.D. MacCraith, *Chemical Reviews*, 108(2008) 400-22.

[28] A. Airoudj, D. Debarnot, B. Bêche, F. Poncin-Epaillard, *Analytical Chemistry*, 80(2008) 9188-94.

[29] H. Qazi, A. Mohammad, M. Akram, *Sensors*, 12(2012) 16522-56.

[30] T. Watanabe, S. Okazaki, H. Nakagawa, K. Murata, K. Fukuda, *Sensors and Actuators B: Chemical*, 145(2010) 781-7.

[31] A. Oprea, N. Bârsan, U. Weimar, *Sensors and Actuators B: Chemical*, 142(2009) 470-93.

[32] T. Usagawa, Y. Kikuchi, *Sensors and Actuators B: Chemical*, 160(2011) 105-14.

[33] J.K.S. Wan, M.S. Ioffe, M.C. Depew, *Sensors and Actuators B: Chemical*, 32(1996) 233-7.

[34] H. Becker, M. von Schickfus, S. Hunklinger, *Sensors and Actuators A: Physical*, 54(1996) 618-21.

[35] A.Z. Sadek, W. Wlodarski, Y.X. Li, W. Yu, X. Li, X. Yu, et al., *Thin Solid Films*, 515(2007) 8705-8.

[36] L.P. Oleksenko, N.P. Maksymovych, A.I. Buvailo, I.P. Matushko, N. Dollahon, *Sensors and Actuators B: Chemical*, 174(2012) 39-44.

[37] B. Wang, L.F. Zhu, Y.H. Yang, N.S. Xu, G.W. Yang, *The Journal of Physical Chemistry C*, 112(2008) 6643-7.

[38] A.Z. Adamyan, Z.N. Adamyan, V.M. Aroutiounian, A.H. Arakelyan, K.J. Touryan, J.A. *International Journal of Hydrogen Energy*, 32(2007) 4101-8.

[39] N.D. Hoa, S.Y. An, N.Q. Dung, N. Van Quy, D. Kim, *Sensors and Actuators B: Chemical*, 146(2010) 239-44.

[40] C. Zhang, A. Boudiba, C. Navio, C. Bittencourt, M.-G. Olivier, R. Snyders, et al., *International Journal of Hydrogen Energy*, 36(2011) 1107-14.

[41] L. Dai, L. Wang, G. Shao, Y. Li, *Sensors and Actuators B: Chemical*, 173(2012) 85-92.

[42] M. Breedon, N. Miura, *Sensors and Actuators B: Chemical*, 182(2013) 40-4.

[43] X. Lu, S. Wu, L. Wang, Z. Su, *Sensors and Actuators B: Chemical*, 107(2005) 812-7.

[44] C.-T. Lee, J.-T. Yan, *Sensors and Actuators B: Chemical*, 147(2010) 723-9.

[45] H.-Y. Lee, H.-L. Huang, C.-T. Lee, *Sensors and Actuators B: Chemical*, 157(2011) 460-5.

[46] K.-S. Kim, G.-S. Chung, *Sensors and Actuators B: Chemical*, 160(2011) 1232-6.

[47] D. Dwivedi, R. Dwivedi, S.K. Srivastava, *Sensors and Actuators B: Chemical*, 71(2000) 161-8.

[48] A. Kumar, P. Zhang, A. Vincent, R. McCormack, R. Kalyanaraman, H.J. Cho, et al., *Sensors and Actuators B: Chemical*, 155(2011) 884-92.

[49] K. Skucha, Z. Fan, K. Jeon, A. Javey, B. Boser, *Sensors and Actuators B: Chemical*, 145(2010) 232-8.

[50] E. Brauns, E. Morsbach, G. Schnurpfeil, M. Bäumer, W. Lang, *Sensors and Actuators B: Chemical*, 187(2013) 420-5.

[51] M. Yang, Y. Sun, D. Zhang, D. Jiang, *Sensors and Actuators B: Chemical*, 143(2010) 750-3.

[52] Z. Zhao, M. Knight, S. Kumar, E.T. Eisenbraun, M.A. Carpenter, *Sensors and Actuators B: Chemical*, 129(2008) 726-33.

[53] D. Chen, J.J. Wang, D.H. Li, Y. Xu, *Sensors and Actuators B: Chemical*, 159(2011) 234-7.

[54] W.P. Jakubik, M.W. Urbańczyk, S. Kochowski, J. Bodzenta, *Sensors and Actuators B: Chemical*, 82(2002) 265-71.

[55] H.H. Möbius, R. Hartung, *J Solid State Electrochem*, 14(2010) 669-73.

[56] H.-H. Möbius, *J Solid State Electrochem*, 1(1997) 2-16.

[57] R. Ramamoorthy, P.K. Dutta, S.A. Akbar, *Journal of Materials Science*, 38(2003) 4271-82.

[58] Robert Bosch GmBh. (Bosch), Oxygen sensors, http://www.boschautoparts.com/oxygensensors/pages/oxygensensors.aspx, 2013.

[59] J. Riegel, H. Neumann, H.M. Wiedenmann, *Solid State Ionics*, 152–153(2002) 783-800.

[60] Lόpez-Gandara, C., F.M. Ramos, *Journal of Sensors*, 2009(2009).

[61] P.K. Sekhar, E.L. Brosha, R. Mukundan, W. Li, M.A. Nelson, P. Palanisamy, et al., *Sensors and Actuators B: Chemical*, 144(2010) 112-9.

[62] N. Miura, G. Lu, N. Yamazoe, *Solid State Ionics*, 136–137(2000) 533-42.

[63] W. Göpel, G. Reinhardt, M. Rösch, *Solid State Ionics*, 136–137(2000) 519-31.

[64] K.H.a.J.B. Goodenough, *Solid oxide fuel cell technology*, UK: Woodhead Publishing in Energy; 2009.

[65] Y. Yan, N. Miura, N. Yamazoe, *Journal of The Electrochemical Society*, 143(1996) 609-13.

[66] W.J. Fleming, *Journal of The Electrochemical Society*, 124(1977) 21-8.

[67] G. Korotcenkov, S.D. Han, J.R. Stetter, *Chemical Reviews*, 109(2009) 1402-33.

[68] R. Mukundan, E.L. Brosha, D.R. Brown, F.H. Garzon, *Electrochemical and Solid-State Letters*, 2(1999) 412-4.

[69] J. Fergus, *J Solid State Electrochem*, 15(2011) 971-84.

[70] E.L. Brosha, R. Mukundan, D.R. Brown, F.H. Garzon, J.H. Visser, M. Zanini, et al., *Sensors and Actuators B: Chemical*, 69(2000) 171-82.

[71] W. Xiong, G.M. Kale, *Sensors and Actuators B: Chemical*, 114(2006) 101-8.

[72] X. Liang, S. Yang, J. Li, H. Zhang, Q. Diao, W. Zhao, et al., *Sensors and Actuators B: Chemical*, 158(2011) 1-8.

[73] S. Guo, E. Wang, *Nano Today*, 6(2011) 240-64.

[74] G. Korotcenkov, *Materials Science and Engineering: B*, 139(2007) 1-23.

[75] P. Elumalai, V.V. Plashnitsa, Y. Fujio, N. Miura, *Sensors and Actuators B: Chemical*, 144(2010) 215-9.

[76] G. Fadeyev, A. Kalakin, A. Demin, A. Volkov, A. Brouzgou, P. Tsiakaras, *International Journal of Hydrogen Energy*, 38(2013) 13484-90.

[77] H. Okamoto, H. Obayashi, T. Kudo, *Solid State Ionics*, 1(1980) 319-26.

[78] H. Okamoto, H. Obayashi, T. Kudo, *Solid State Ionics*, 3–4(1981) 453-6.

[79] H. Okamoto, G. Kawamura, T. Kudo, *Journal of Catalysis*, 87(1984) 1-9.

[80] A. Vogel, G. Baier, V. Schüle, *Sensors and Actuators B: Chemical*, 15(1993) 147-50.

[81] N. Miura, T. Raisen, G. Lu, N. Yamazoe, *Sensors and Actuators B: Chemical*, 47(1998) 84-91.

[82] J. Zosel, G. Schiffel, F. Gerlach, K. Ahlborn, U. Sasum, V. Vashook, et al., *Solid State Ionics*, 177(2006) 2301-4.

[83] T. Hibino, A. Hashimoto, S. Kakimoto, M. Sano, *Journal of The Electrochemical Society*, 148(2001) H1-H5.

[84] L.P. Martin, A.Q. Pham, R.S. Glass, *Solid State Ionics*, 175(2004) 527-30.

[85] P.K. Sekhar, E.L. Brosha, R. Mukundan, M.A. Nelson, T.L. Williamson, F.H. Garzon, *Sensors and Actuators B: Chemical*, 148(2010) 469-77.

[86] F.H. Garzon, R. Mukundan, R. Lujan, E.L. Brosha, *Solid State Ionics*, 175(2004) 487-90.

[87] E.L. Brosha, R. Mukundan, D.R. Brown, F.H. Garzon, *Sensors and Actuators B: Chemical*, 87(2002) 47-57.

[88] R. Sorita, T. Kawano, *Sensors and Actuators B: Chemical*, 36(1996) 274-7.

[89] G. Lu, N. Miura, N. Yamazoe, *Sensors and Actuators B: Chemical*, 35(1996) 130-5.

[90] W.F. Chu, V. Leonhard, H. Erdmann, M. Ilgenstein, *Sensors and Actuators B: Chemical*, 4(1991) 321-4.

[91] Y. Tan, T.C. Tan, *Journal of The Electrochemical Society*, 141(1994) 461-7.

Chapter 2

Selective Hydrogen Detection by Combining Two-oxides-based Sensing Electrodes

2.1 Introduction

It has been established in the previous chapter that, YSZ-based gas sensors have been acknowledged as one of the leading candidates, owing to the ability of fulfilling the requirements of high-performance gas sensors [1-3]. This fact makes a YSZ-based sensor also a suitable candidate for in-situ measurement of H_2. However, the main challenge in YSZ-based H_2 sensor development is the interference from various co-existing gases, such as carbon monoxide (CO) and hydrocarbons (HCs) which may cause a false signal [4, 5].

Pairing two metal-oxides with different sensing properties in combined-type sensor configuration, has been proven to be an effective method for cancelling out unwanted cross-sensitivity from interfering gases, resulting in sensitive and selective responses toward a target gas [5, 6]. When an H_2 sensitive oxide-based-SE paired with an appropriate counter-part electrode, the resulting combined-type sensor is expected to generate minimum responses toward the interfering gases, while maintaining sensitive response to H_2. Therefore, an effort to develop a highly selective and sensitive H_2 sensor by pairing two SEs as a combined-type sensor is reported here.

Selective H_2 sensor development was begun by investigating a suitable H_2-sensitive electrode material which was selected from several metal oxides. Afterward, a prospective counter electrode material was chosen among several oxide SE materials

that have been reported to generate sensitive and selective response toward the interfering gas. In addition to these, the author also proposes YSZ addition as a method to improve the mechanical resilient of SnO_2 as the SE. The effect of increasing YSZ addition on the sensing performance of the developed sensor using SnO_2 as the SE material will be also discussed here with respect to sensing response and electrode morphology.

2.2 Experimental

2.2.1 Fabrication of sensor devices

The sensor was fabricated by using a commercial hemispherically-terminated YSZ tube (8 mol.% Y_2O_3-doped ZrO_2, Nikkato, Japan). The physical dimensions of the tube were 300 mm in length; 5 and 8 mm in inner and outer diameter, respectively. The schematic representation of the tubular sensor is shown in Fig. 2.1. Here, circuits (a) and (b) represent the connectivity used for the single-type sensor which is comprised of a metal oxide SE, measured against inner Pt/air-RE. Circuit (a) represents the single-type SnO_2 (+ 30 wt.% YSZ)-SE, and circuit (b) indicates the connectivity of the single-type NiO (+50 mol.% TiO_2)-SE. Circuit (c) represents the connection used in the combined-type sensor using SnO_2 (+ 30 wt.% YSZ)-SE and NiO (+ 50 mol.% TiO_2)-SE.

The sensing-performance stabilization of the mixed-potential-type YSZ-based sensors has been proposed recently via the utilization of an additional YSZ layer in between the SE and the YSZ solid electrolyte [7]. The existence of such an intermediate YSZ layer can stabilize the sensing signal and improve the mechanical stability of SE [6]. Thus, an intermediate YSZ layer (*i*-YSZ) between SE and the YSZ tube was also formed in this study. The YSZ powder (8 mol.% Y_2O_3-doped ZrO_2, Tosoh, Japan) was

mixed with an organic binder (α-terpineol) and the resulting paste was applied onto the surface of the YSZ tube. Following this, a commercial SnO_2 powder (Kishida Chemical, Japan) was used as the base material for SnO_2-based SE. When required, the YSZ powder was added into the SnO_2 powder and ground in a mortar. Then, α-terpineol was added into the oxide powder mixture to make a uniform paste. The obtained paste was applied onto the surface of the YSZ layer to form a 4 mm-wide banded SE layer.

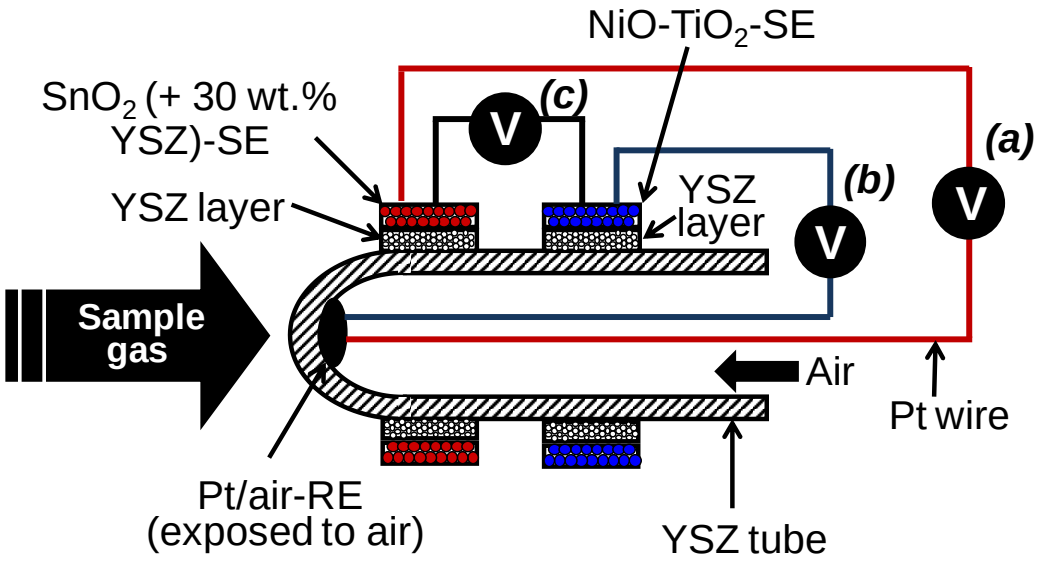

Figure 2.1 Schematic representation of the fabricated YSZ-based sensor utilizing SnO_2(+ 30 wt.% YSZ)-SE vs. Pt-RE (circuit (a)), NiO-TiO_2-SE vs. Pt-RE (circuit (b)), and the combined-type sensor utilizing SnO_2(+ 30 wt.% YSZ)-SE vs NiO-TiO_2-SE (circuit (c)). (Reproduced from [14], Copyright 2012, with permission from Elsevier)

In a similar manner, NiO(+ 50 mol.% TiO_2)-SE, henceforth denoted as NiO-TiO_2-SE, was fabricated with a commercial NiO powder (Kojundo Chemical Lab., Japan) which was mixed ultrasonically in ethanol with TiO_2 (Kojundo Chemical Lab. Co., Japan), dried and ground in a mortar. The NiO(+ 5 wt.% Au)-SE was fabricated by sonicating the commercial NiO powder with a commercial gold powder (particle size 0.3 -0.6 μm, Nilaco, Japan) in ethanol, followed by drying at 130^{o}C, and subsequently

grinding in a mortar. A commercial $ZnCr_2O_4$ powder (Kojundo Chemical Lab., Japan) was utilized to fabricate the $ZnCr_2O_4$-SE. The same organic binder was also added to make a paste, which was painted as a 3 mm-wide band on the surface of the intermediate YSZ layer. The Pt paste (Tanaka Kikinzoku, Japan) was applied on the inner side of YSZ tube. The painted-YSZ tube was then dried at 130^oC, and subsequently sintered at 1000^oC for 2 h.

As illustrated in Fig. 2.1, for the single-type sensors (circuits (a) and (b)), all potential measurements were conducted by connecting the metal-oxide SEs to the positive terminal of a digital electrometer (R8240, Advantest, Japan) and the inner Pt/air-RE to the negative terminal of the electrometer.

(+) SnO_2 (+YSZ)|*i*-YSZ|YSZ|Pt,air (-)

(+) NiO-TiO_2|*i*-YSZ|YSZ|Pt,air (-)

Circuit (c) in Fig. 2.1 depicts the arrangement of the combined-type sensor. For the combined-type sensor, all potential measurements were carried out by connecting the two electrodes; with the SnO_2-based electrode to the positive current-collector lead and the NiO-based electrode to the negative current-collector lead, as indicated below:

(+) SnO_2 (+YSZ)|*i*-YSZ|YSZ|*i*-YSZ|NiO-TiO_2 (-)

2.2.2 Evaluation of the sensing properties of the single-type sensor

The fabricated tubular YSZ-based sensors were assembled in a custom quartz testing-cell in close proximity to the gas inlet, and connected to a conventional gas-flow apparatus equipped with a high-temperature electric furnace (Fig, 2.2). The evaluation of gas-sensing characteristics was performed at 600^oC. The sensor was exposed to the humidified base-gas (21 vol.% O_2 + 5 vol.% H_2O + N_2 balance) or the humidified sample-gas containing H_2, CO, C_3H_6, CH_4, NO or NO_2, diluted with the base gas, under

a constant gas flow-rate of 100 cm^3/min. The gas concentration of each sample gas was fixed at 100 ppm for cross sensitivity measurements. The concentration of water vapor was also fixed at 5 vol.%, except for the examination of water vapor effect on gas-sensing characteristics. The inner Pt electrode was always exposed to ambient atmospheric air, functioning as a Pt/air-RE. The difference in potential (*emf*) between either of the outer SEs connected to the positive terminal of the electrometer and the inner Pt/air-RE connected to the negative terminal was measured as a sensing signal. The gas sensitivity (Δemf) was defined as the difference between the emf value in the base gas and that in the sample gas.

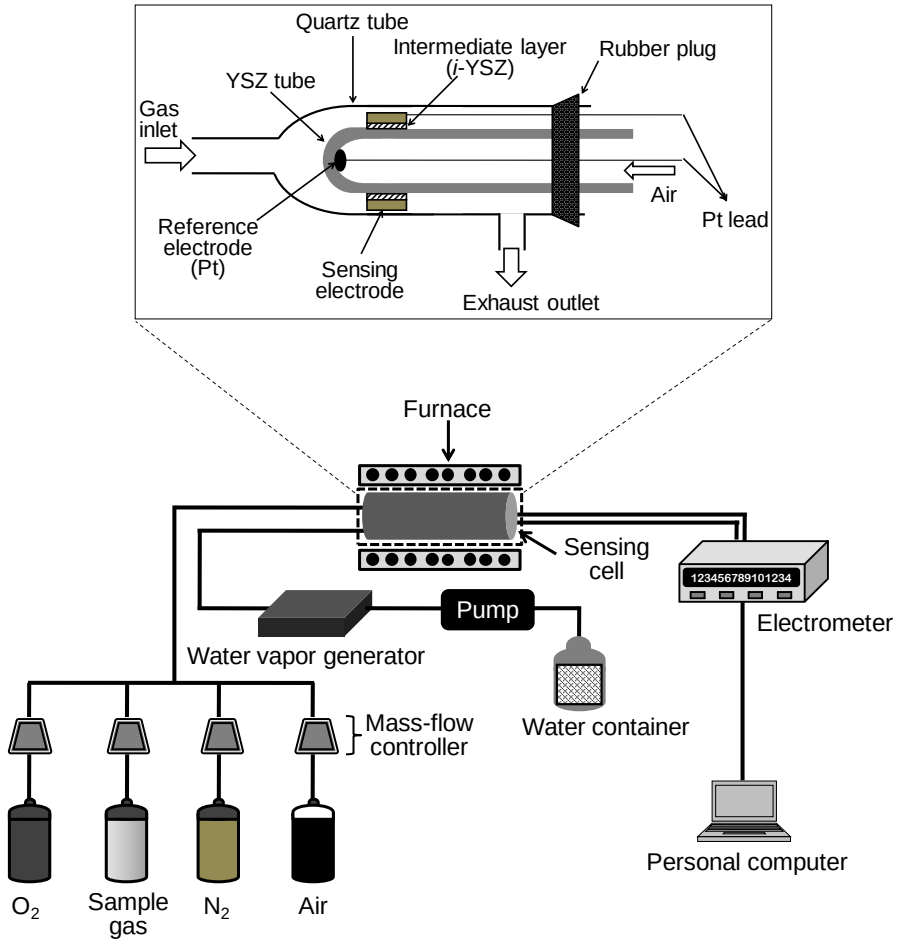

Figure 2.2 The schematic view of the sensor evaluation system. (Inset: The schematic illustration of the sensor arrangement inside the quartz cell). (Reproduced from [15], Copyright 2013, with permission from Elsevier)

2.2.3 Polarization curve measurements.

The current-voltage (polarization curve) characteristics were measured by means of an automatic polarization system (HZ-3000, Hokuto Denko, Japan). The potential scan was carried out in potentiodynamic mode at a scan rate of 5 mV/min, for the base gas (21 vol.% O_2) as well as the sample gas containing 100 ppm H_2 (+ 21 vol.% O_2) in humid conditions (5 vol.% H_2O). The modified polarization curve for the cathodic reaction of O_2 was obtained by plotting the applied potential against the absolute current value. The modified polarization curve for the anodic reaction of H_2 was estimated by subtracting the current value in the base gas from the current value in sample gas at each potential.

2.2.4 Morphology and crystal structure of SE

The morphology of SE was observed by using a field emission scanning electron microscope (FE-SEM, JSM-6340F, JEOL, Japan). The crystal structure of the SE layer was examined by means of an X-ray diffractometer (XRD, RINT 2100VLR/PC, Rigaku, Japan) with Cu Kα radiation (λ = 1.5406 Å).

2.3 Results and discussion.

2.3.1 The single-type sensor using SnO_2-based-SE

Prior to the decision to employ a SnO_2-based-SE as an H_2 sensitive electrode, several metal oxides were investigated as a potential sensing electrode material, and their sensing performances toward H_2 were examined against a Pt/air-RE. For this material screening-test, an intermediate YSZ layer was deposited prior to the application of the metal-oxide sensing layer, to improve the mechanical strength of the interface between SE and YSZ. Fig. 2.3 shows the comparison of H_2 sensitivity for SE materials

examined in this study. It can be seen that SnO_2 gave the highest response toward 100 ppm H_2, when compared with other examined metal-oxide SEs. Nevertheless, since some processes in our sensor fabrication were conducted manually by hand, the mechanical resilience of the electrode, especially when winding the Pt current-collector, is a critical requirement for ease of manufacture. As for SnO_2, the mechanical resilience of SnO_2-SE itself was often found to be insufficient to endure the fabrication processes. Therefore, further enhancing the mechanical stability of the SE was necessary.

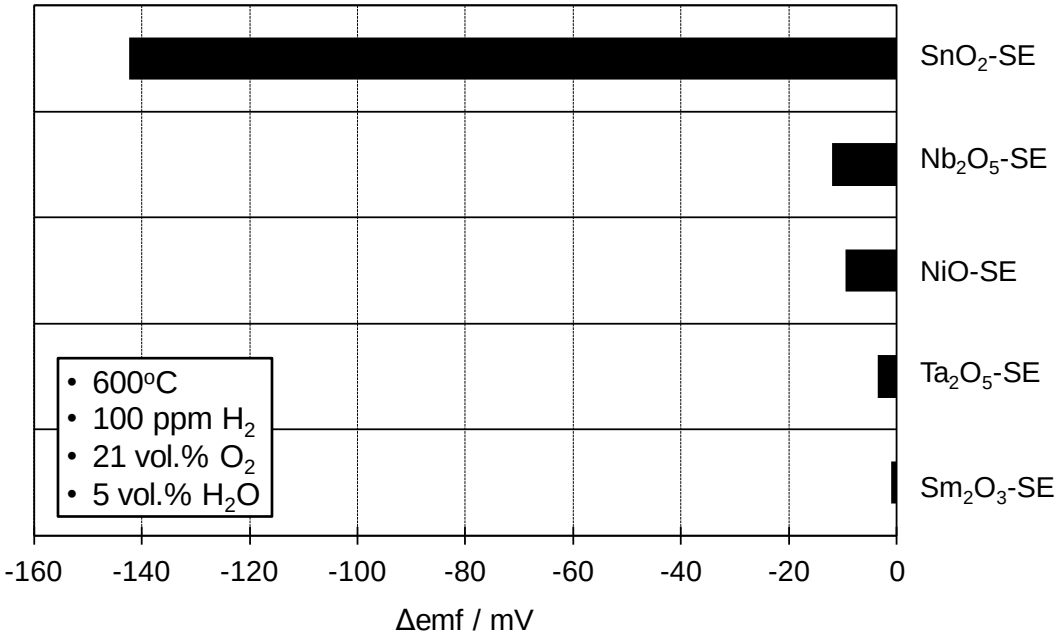

Figure 2.3 The responses toward 100 ppm H_2 for several YSZ-based sensors utilizing each of different metal-oxide SEs, operated at 600°C under humid conditions (21 vol.% O_2 and 5 vol.% H_2O). (Reproduced from [14], Copyright 2012, with permission from Elsevier)

A study conducted by Wama *et al.* revealed that additions of YSZ into the metal oxide SE material could improve the mechanical stability of the sensor [8]. Then, YSZ was added into the SnO_2-SE in different mixing ratios and the sensing performance was examined here. When YSZ powder was added into the SnO_2 powder, the resulting SE

was found to have better mechanical stability than the electrode without the YSZ additive. However, the addition of YSZ also affects the sensing performance of sensor. Fig. 2.4 compares the cross sensitivities of the sensors using each of SnO_2-SEs with different ratios of YSZ additive. The addition of 10 wt.% YSZ slightly decreased the gas sensitivity ((Δemf) from -142 mV to -128 mV. However, the gas selectivity trend is indifferent from those of the original SnO_2-SE; the sensitivity to propene (C_3H_6) is still higher than that of H_2. When the YSZ content was raised to 30 wt.%, a lower response toward H_2 and C_3H_6, was observed (Δemf = -75 mV and -55 mV, respectively). In this case, better H_2 selectivity was observed compared with the previous two SEs. Further increasing YSZ addition up to 50 wt.% brought about a dramatic decrease in sensitivity ((Δemf < -5 mV) to almost all examined gases.

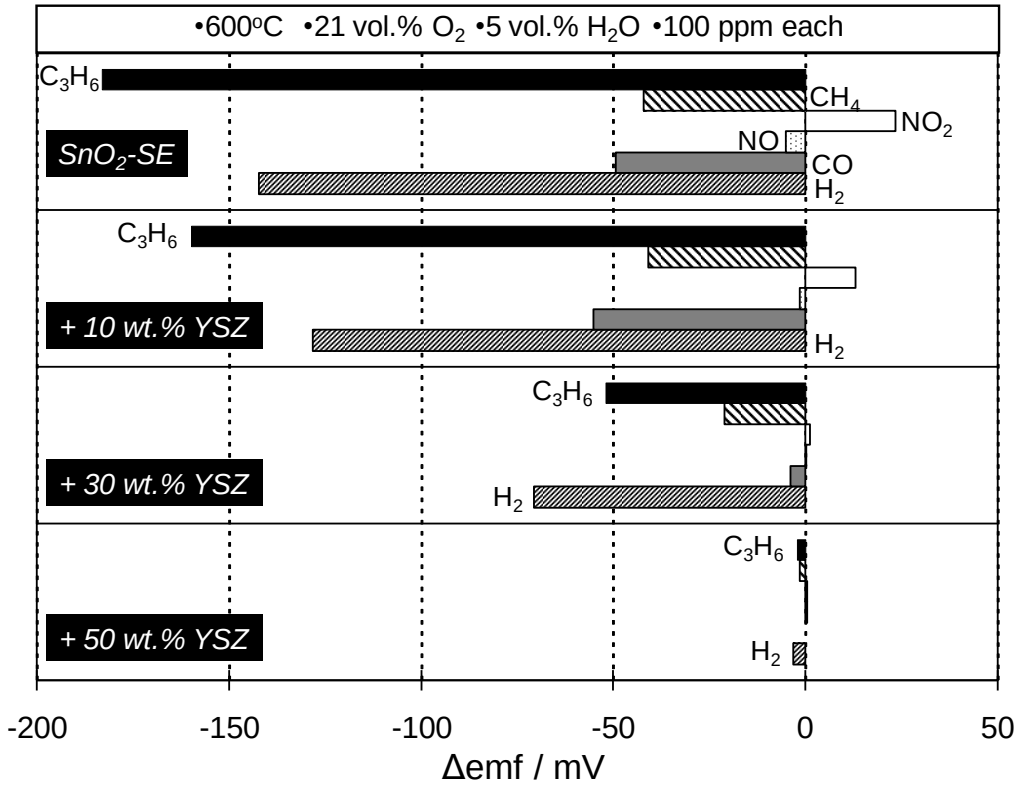

Figure 2.4 The cross sensitivities of the sensors using SnO_2-SEs with different additions of YSZ (10, 30, and 50 wt.%), operated at 600°C under humid condition (21 vol.% O_2 and 5 vol.% H_2O). (Reproduced from [14], Copyright 2012, with permission from Elsevier)

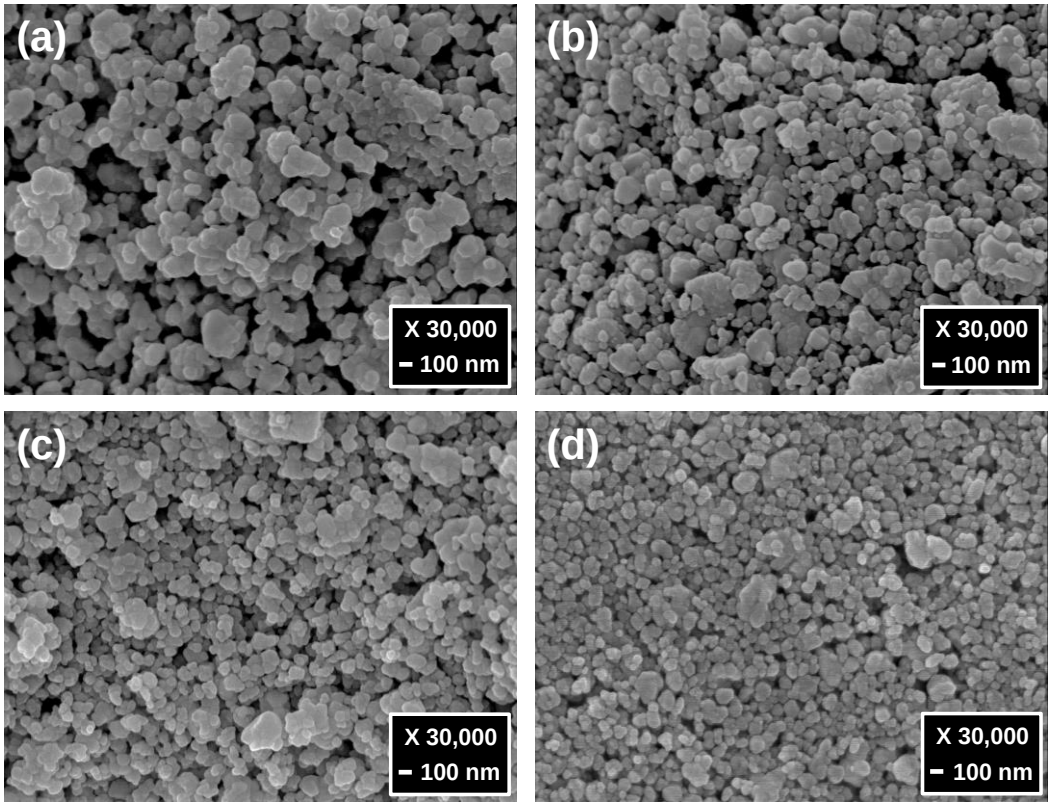

Figure 2.5 The representative SEM images of (a) SnO_2, (b) SnO_2(+ 10 wt.% YSZ), (c) SnO_2 (+ 30 wt.% YSZ) and (d) SnO_2(+ 50 wt.% YSZ), after sintering at 1000^{o}C for 2 h. (Reproduced from [14], Copyright 2012, with permission from Elsevier).

The morphological transformation of the SnO_2-SE after the respective additions of YSZ and sintering at 1000^{o}C for 2 h was investigated by SEM observation. Fig. 2.5 is a comparison of representative SEM surface images of SnO_2–SE without (a), and with (b-d) the addition of YSZ. As can be seen from Fig. 2.5 (a), after sintering at 1000^{o}C, SnO_2 had a porous structure which was comprised of polygonal-shaped particles, with a particle size of approximately 100-400 nm. However, the addition of 10 wt.% YSZ resulted in a slight apparent densification of the surface, as some of the inter-particle voids were observed to be blocked, by the smaller YSZ particles (approximately 100 nm), even after a 10 wt.% YSZ addition (Fig. 2.5 (b)). The addition of 30 wt.% YSZ was observed to further reduce the porosity of the SnO_2-SE surface, creating a slightly denser surface (Fig. 2.5 (c)), when compared with SnO_2-SE with lower YSZ addition.

When the YSZ addition increased up to 50 wt.%, a significantly denser surface was obtained when compared with SnO_2 alone, as more voids were blocked with the smaller YSZ particles (Fig. 2.5 (d)). Interestingly, the particle size and shape of the SnO_2 itself were largely unaffected by the addition of YSZ, even after sintering at 1000°C for 2 h (Fig. 2.5 (b-d)).

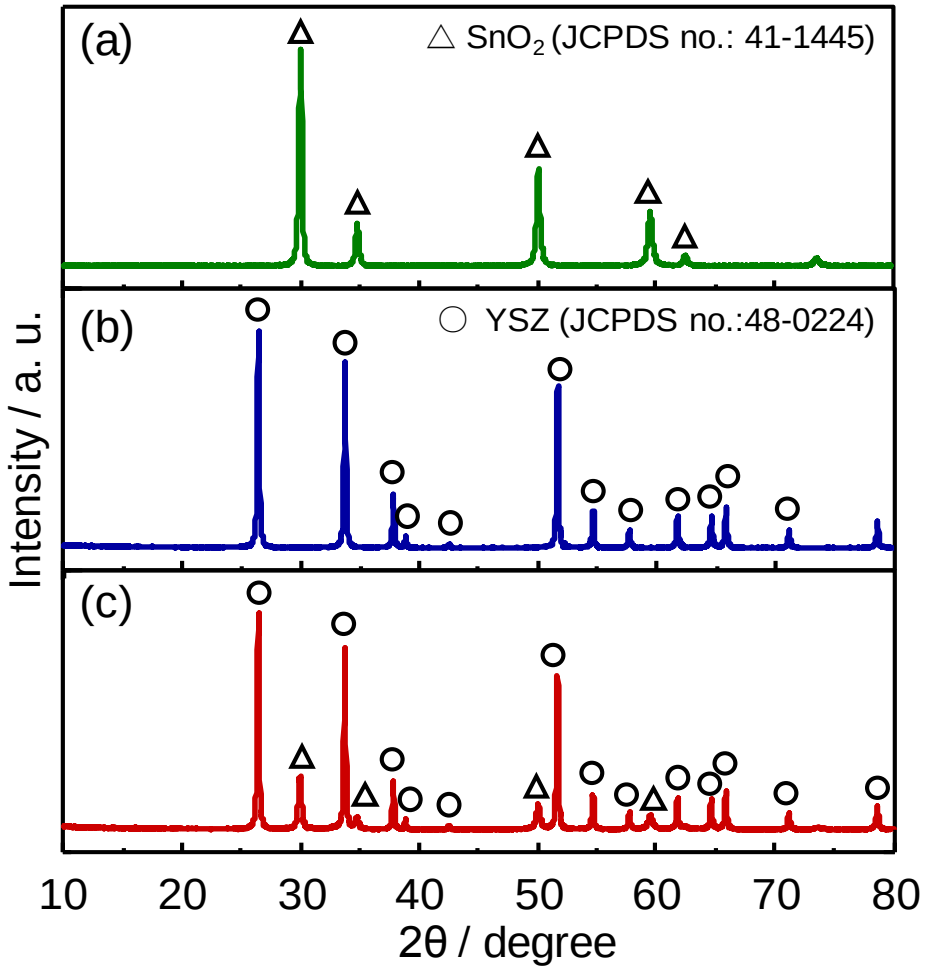

Figure 2.6 The XRD patterns for (a) SnO_2, (b) YSZ and (c) SnO_2(+30 wt.% YSZ), after sintering at 1000°C for 2 h. (Reproduced from [14], Copyright 2012, with permission from Elsevier)

In order to confirm that the addition of YSZ would not form any unexpected compounds with SnO_2, XRD measurements were conducted. For comparison, SnO_2 and YSZ powders were separately sintered at 1000°C, their corresponding X-ray diffraction patterns are presented in Fig. 2.6 (a) and (b), respectively. These patterns are in good

agreement with the reference patterns for SnO_2 (JCPDS no. : 41-1445) and YSZ (JCPDS no. : 48-0224). Fig. 2.6 (c) shows the peaks observed for the mixed SnO_2 (+ 30 wt. % YSZ)-SE material. Despite sintering at 1000^oC for 2 h, the addition of YSZ into SnO_2 did not result in the formation of a new phase or solid solution, since all observed peaks were in excellent agreement with those identified for SnO_2 and YSZ.

The effect of YSZ additions on the sensing performance of the developed sensors can be rationalized via the measurement of polarization (current–voltage) curves. Polarization curves can also be used to explain and confirm the sensing mechanism based on mixed potential. By using a modified polarization curve, the mixed potential that arises at the SE/YSZ interface can be confirmed mathematically [9]. Here, the mixed potential is defined as the potential where the modified cathodic and anodic polarization curves intersect when plotted together. The cathodic and anodic reactions ((1) and (2)) that proceed simultaneously at the SE/YSZ interface cause the development of a mixed-potential.

$$O_2 + 4e^- \rightarrow 2O^{2-} \quad (1)$$

$$2H_2 + 2O^{2-} \rightarrow 2H_2O + 4e^- \quad (2)$$

The polarization curve measurements for the tubular YSZ-based sensors using SnO_2-SEs with different additions of YSZ were conducted in the base gas (21 vol.% O_2) or the sample gas (100 ppm H_2 + 21 vol.% O_2) at 600^oC in humid conditions (5 vol.% H_2O). The measurements were performed with respect to an inner Pt/air-RE by applying a linearly increasing sweep potential over a defined range and measuring the generated current. Fig. 2.7 (a) shows the modified cathodic polarization curves of 21 vol.% O_2. Here, the absolute current values are used in these modified cathodic curves. Similarly, Fig. 2.7 (b) shows the modified anodic polarization curves of 100 ppm H_2. These modified polarization curves are plotted together in Fig. 2.7 (c).

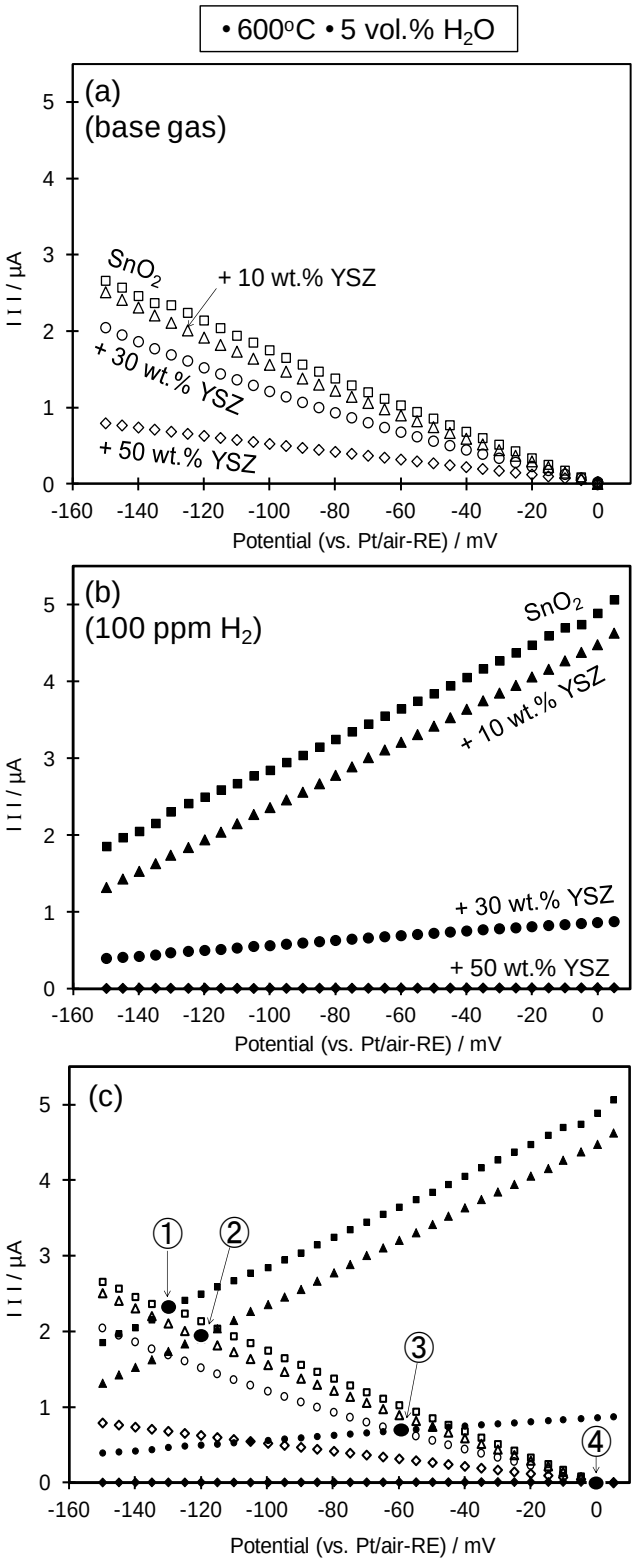

Figure 2.7 (a) The modified cathodic polarization curves of 21 vol.% O_2, (b) the modified anodic polarization curves of 100 ppm H_2 and (c) the combined cathodic and anodic polarization curves, for the tubular YSZ-based sensors using SnO_2-SEs with different additions of YSZ, at an operational temperature of 600°C. (Reproduced from [14], Copyright 2012, with permission from Elsevier)

Table 2.1 The comparison between estimated mixed-potential value and observed emf value, for the sensors utilizing SnO_2-SEs with increasing addition of YSZ, toward 100 ppm H_2 operated at 600°C. (The number ①-④ are corresponding to those given in Fig. 6) (Reproduced from [14], Copyright 2012, with permission from Elsevier)

	① SnO_2 only	② + 10 wt.% YSZ	③ + 30 wt.% YSZ	④ + 50 wt.% YSZ
Estimated mixed-potential (mV)	-130	-120	-60	-1
Observed emf value (mV)	-142	-128	-75	-3

As shown in Fig. 2.7 (a) and (b), the measured current for the cathodic reaction of O_2 as well as for the anodic reaction of H_2 decreased with increasing YSZ additions into SnO_2-SE. This trend is speculated to originate from one or a combination of the following possible explanations. Firstly, the addition of YSZ into SnO_2-SE will effectively displace SnO_2 particles at the triple phase boundary (TPB), decreasing the number of available reaction site for the electrochemical reactions to proceed at the interface of SE/YSZ. Secondly, the denser and more tortuous morphology (Fig. 2.5 (b-d)) which formed after the addition of YSZ into SnO_2 may have significantly decreased the proportion of some reactant gases capable of reaching the SE/YSZ interface. Thirdly, the addition of YSZ into SnO_2-SE may have caused subtle surface changes. These changes may include those pertaining to crystallography, morphology, stoichiometry, and surface states caused by the formation of compounds which are dissimilar to those of the original materials. Should such surface changes take place, they are likely to be so small that they are undetectable via XRD measurements. These changes may affect gas sensitivity.

Fig. 2.7 (c) shows the modified polarization curves for both anodic and cathodic reactions, confirming that the examined sensors are governed by the mixed-potential

sensing mechanism. The intersection point (estimated value) of anodic and cathodic curves for each of the sensor using the SnO_2-based SEs numerically correspond well with the generated emf value (observed H_2 sensitivity), as summarized in Table 2.1. Since the generated current was found to decrease for both anodic and cathodic reactions with increasing YSZ addition, the corresponding intersection points were observed to decrease, eventually approaching 0 mV for SnO_2(+ 50 wt.% YSZ)-SE (④). Thus, the mixed-potential for each sensor using SnO_2-based-SEs decreased with increasing YSZ addition. The good consistency between each estimated mixed-potential value and each observed sensor's emf response confirms that the sensing mechanism of the present sensors is based on the mixed-potential model [10-12].

2.3.2. Construction of the combined-type sensor

Our group has already demonstrated the utilization of $ZnCr_2O_4$, NiO (+ 5 wt.% Au), and NiO-TiO_2 as excellent SE materials in a YSZ-based sensor for sensitive and selective sensing of propene (C_3H_6) at high temperature (550-650^{o}C) [7, 10, 13]. Thus, another set of tubular YSZ sensors utilizing each of $ZnCr_2O_4$-, NiO (+ 5 wt.% Au)-, and NiO-TiO_2-SEs as well as Pt/air-RE was then fabricated in this study. Here, an additional layer of YSZ was also used as an intermediate layer between the SE and the YSZ tube.

The cross sensitivities toward different tested gases were examined for these three sensors at 600^{o}C under 21 vol.% O_2 and 5 vol.% H_2O. As shown in Fig. 2.8, each sensor can generate a relatively sensitive and selective emf response toward C_3H_6 at 600^{o}C. Among the examined SEs, the sensor utilizing NiO-TiO_2-SE was observed to have the closest sensitivity toward 100 ppm C_3H_6 (Fig. 2.8 (c)), with that generated by the sensor using SnO_2 (+ 30 wt.% YSZ)-SE. Hypothetically, if both of NiO-TiO_2-SE and SnO_2(+ 30 wt.% YSZ)-SE were paired as a combined-type sensor, the response toward C_3H_6

could be significantly minimized while maintaining high response toward H_2. Therefore, a combined-type sensor utilizing SnO_2 (+ 30 wt.% YSZ) electrode and NiO-TiO_2 electrode was fabricated, and its sensing performances were examined at 600°C.

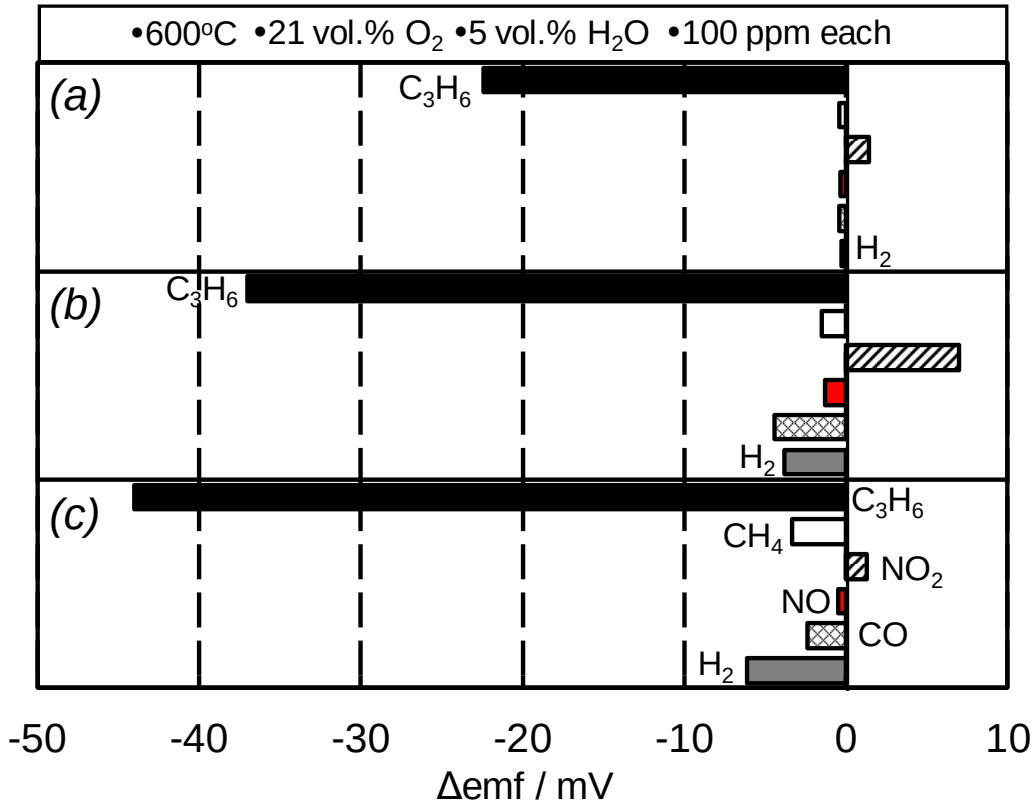

Figure 2.8 The comparison of the cross sensitivity to various gases (100 ppm) examined for each single-type sensor comprised of (a) $ZnCrO_4$-SE, (b) NiO (+ 5 wt.% Au)-SE, and (c) NiO-TiO_2-SE, operated at 600°C under humid operating conditions (21 vol.% O_2 and 5 vol.% H_2O). (Reproduced from [14], Copyright 2012, with permission from Elsevier)

The response transient to different gases for this combined-type sensor are shown in Fig. 2.9 (c), together with those obtained for the single-type sensors using each of SnO_2(+ 30 wt.% YSZ)-SE (Fig. 8 (a)) and NiO-TiO_2-SE (Fig. 2.9 (b)). This combined-type sensor could generate better selectivity toward H_2, when compared with

the sensor using the parental SnO_2-based SE. This indicates that the combined-type sensors can actually cancel and diminish effectively the responses toward interfering gases (especially C_3H_6), while maintaining high H_2 sensitivity.

The response transients to various H_2 concentrations were examined for the combined-type sensor and the results are presented in Fig. 2.10 (a). This sensor responded even to low concentrations of H_2 (20 and 40 ppm), with 90% response time of about 25 s. For higher H_2 concentrations (100 –800 ppm), the 90% response time was as short as approximately 9 s for all measured concentrations. Fig. 2.10 (b) depicts the dependence of sensitivity on H_2 concentration for the present sensor. Good linearity between Δemf and H_2 concentration on a logarithmic scale was observed. In addition, the effect of water vapor concentration in the sample gas on the emf response of the combined-type sensor is given in Fig. 2.10 (c). It can be seen that the change in H_2O concentration within the range of 1-4 vol.% hardly affects the baseline value or the emf responses toward 100 and 800 ppm H_2. This indicates that the combined-type sensor will be able to endure operating conditions, while maintaining stable H_2 sensing characteristics.

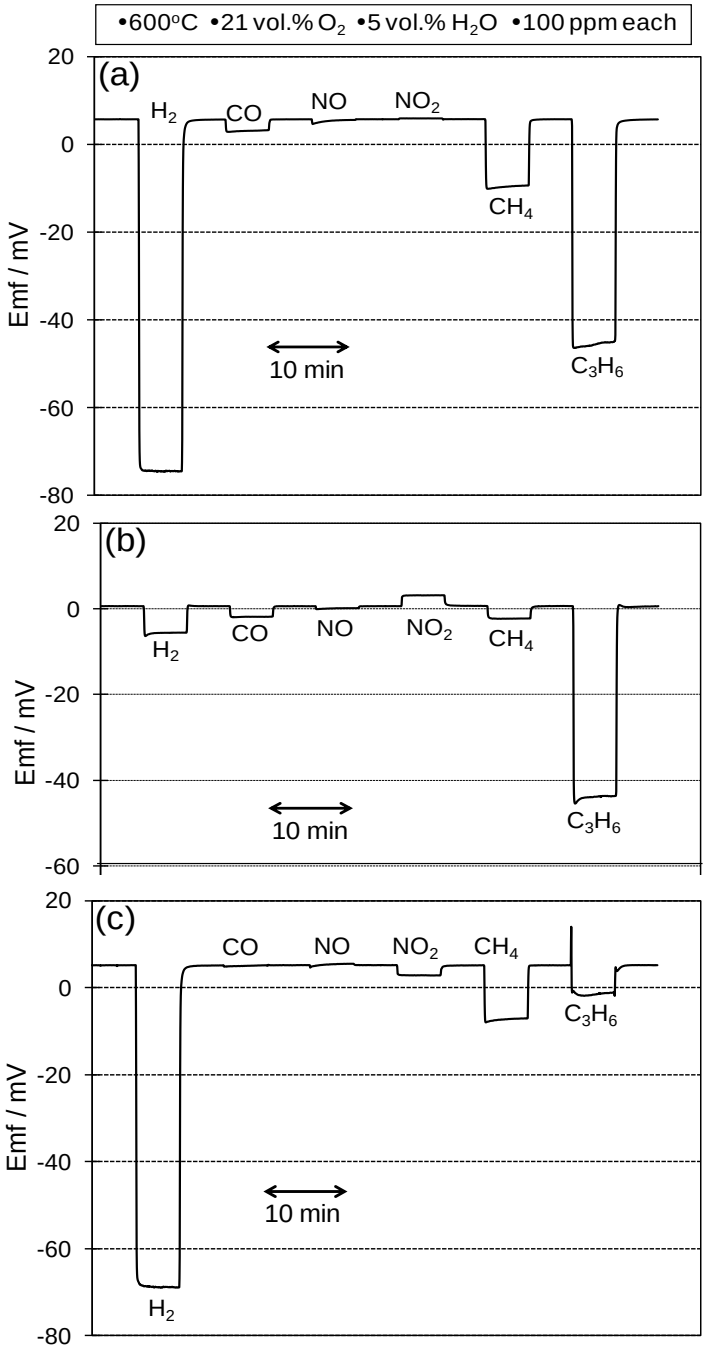

Figure 2.9 The response transients of the sensors utilizing (a) SnO_2 (+ 30 wt.% YSZ)-SE vs. Pt/air-RE, (b) NiO-TiO_2-SE vs. Pt/air-RE, (c) SnO_2 (+ 30 wt.% YSZ) electrode vs. NiO-TiO_2 electrode, operated at 600°C under humid conditions (21 vol.% O_2 and 5 vol.% H_2O). (Reproduced from [14], Copyright 2012, with permission from Elsevier)

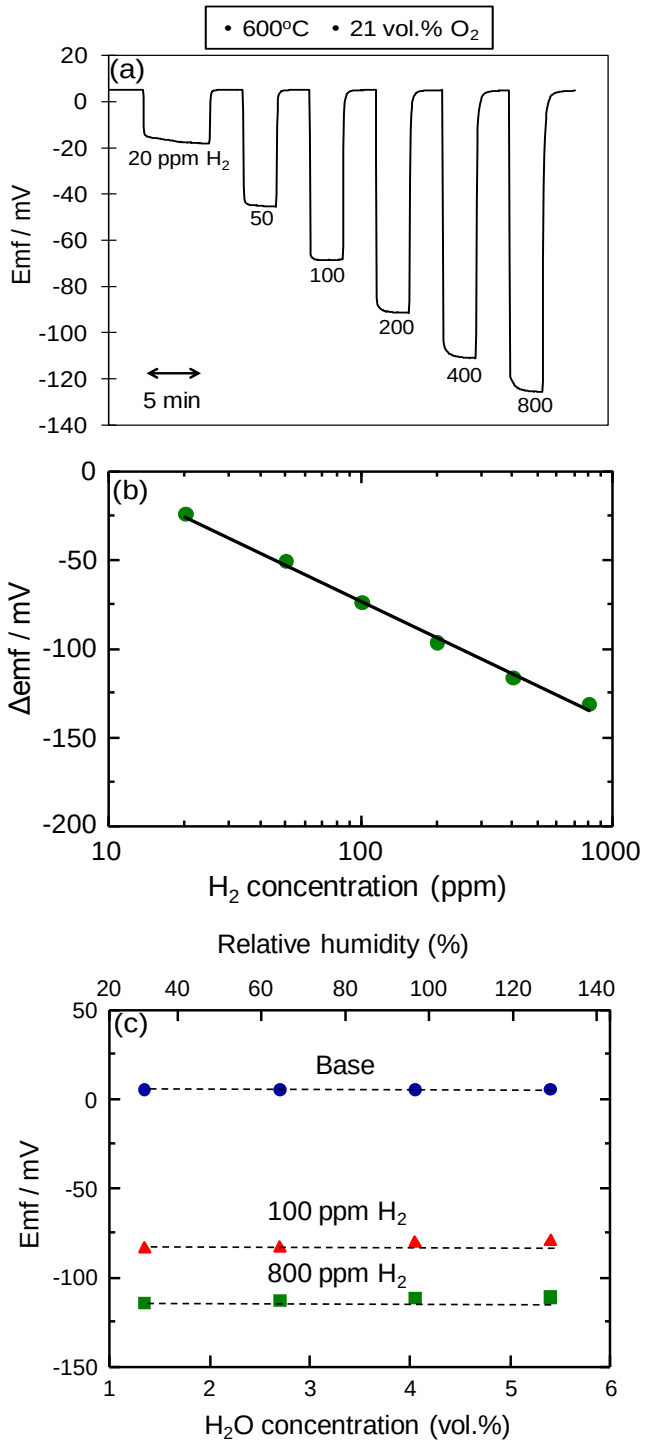

Figure 2.10 (a) The response transients to various H_2 concentrations, (b) the dependence of sensitivity on the logarithm of H_2 concentration, and (c) the effect of water vapor concentration on emf response, for the combined-type sensor using SnO_2(+ 30 wt.% YSZ) electrode and NiO-TiO_2 electrode, at an operational temperature of 600°C. Corresponding relative humidity values were calculated at 30°C. (Reproduced from [14], Copyright 2012, with permission from Elsevier)

2.4 Conclusions

The utilization of the sensor comprised of a YSZ solid electrolyte and an oxide-based SE was examined here for sensitive H_2 detection. The addition of 30 wt.% YSZ into SnO_2-SE could improve the mechanical stability of the sensor, while maintaining sensitive response toward H_2. The increasing YSZ content in the SnO_2–SE resulted in denser electrode morphology and was accompanied with a decrease in current for both polarization curves of anodic reaction of H_2 and cathodic reaction of O_2. The mixed potential value estimated from the intersection point of the both modified anodic and cathodic polarization curves was found to correspond well with the observed emf value of the single-type sensors using each of the SnO_2-based SEs. This suggests that the sensing mechanism of the present single-type sensors is based on mixed-potential model. In order to reduce the cross sensitivity to interfering gas (C_3H_6), the SnO_2(+ 30 wt.% YSZ) electrode was paired with the NiO-TiO_2 electrode, constructing a combined-type sensor. As a result, this sensor could detect H_2 sensitively and selectively, with acceptable response and recovery speed, as well as the water vapor insensitivity.

(Some of the contents in this chapter is reproduced from [14], Copyright 2012, with permission from Elsevier)

References

[1] P.E. Norio Miura, Vladimir V. Plashnitsa, Taro Ueda, Ryotaro Wama, Masahiro Utiyama, Solid State Electrochemical Gas Sensing, in: G.F. Elisabetta Comini, Giorgio Sberveglieri (Ed.) Solid State Gas Sensing, Springer Science + Business Media, LLCC, USA, 2009, p. 181.

[2] C.O. Park, J.W. Fergus, N. Miura, J. Park, A. Choi, *Ionics*, 15(2009) 261-84.

[3] G. Lu, N. Miura, N. Yamazoe, *Sensors and Actuators B: Chemical*, 35(1996) 130-5.

[4] P. Elumalai, V.V. Plashnitsa, T. Ueda, N. Miura, *Electrochemistry Communications*, 10(2008) 745-8.

[5] N. Miura, T. Raisen, G. Lu, N. Yamazoe, *Sensors and Actuators B: Chemical*, 47(1998) 84-91.

[6] S.A. Anggraini, V.V. Plashnitsa, P. Elumalai, M. Breedon, N. Miura, *Sensors and Actuators B: Chemical*, 160(2011) 1273-81.

[7] Y. Fujio, V.V. Plashnitsa, P. Elumalai, N. Miura, *Talanta*, 85(2011) 575-81.

[8] R. Wama, V.V. Plashnitsa, P. Elumalai, T. Kawaguchi, Y. Fujio, M. Utiyama, et al., *Journal of The Electrochemical Society*, 156(2009) J102-J7.

[9] V.V. Plashnitsa, V. Gupta, N. Miura, *Electrochimica Acta*, 55(2010) 6941-5.

[10] Y. Fujio, V.V. Plashnitsa, N. Miura, *Journal of the Ceramic Society of Japan*, 118(2010) 197-201.

[11] G.M. Kale, *Advanced Powder Technology*, 20(2009) 426-31.

[12] D. Schönauer, K. Wiesner, M. Fleischer, R. Moos, *Sensors and Actuators B: Chemical*, 140(2009) 585-90.

[13] P. Elumalai, V.V. Plashnitsa, Y. Fujio, N. Miura, *Sensors and Actuators B: Chemical*, 144(2010) 215-9.

[14] M. Yamaguchi, S. A. Anggraini, Y. Fujio, M. Breedon, V. V. Plashnitsa, N. Miura, *Electrochimica Acta*, 76 (2012) 152-8

[15] S. A. Anggraini, M. Breedon, N. Miura, *Sensors and Actuators B: Chemical*, 187 (2013) 58-64.

Chapter 3

SnO_2-based Sensing Electrode with Integrated Catalyst Layer for Selective H_2 Detection

3.1 Introduction

In the previous chapter, the utilization of SnO_2 as sensing electrode material for sensitive H_2 detection has been reported. The lack of mechanical strength that initially observed was improved by the addition of YSZ powder into SnO_2-SE [1]. The poor H_2-selectivity of the sensor using SnO_2 (+ 30 wt.% YSZ)-SE was solved by pairing it with NiO(+ 50 mol.% TiO_2)-SE, constructed as a combined-type sensor to cancelling out the response to unwanted gas responses [2].

Given the importance of a highly selective and sensitive H_2 sensor, another strategy to improve the selectivity of a YSZ-based sensor using a selective catalyst layer is proposed in this chapter. The existence of a selective catalyst layer on top of SE layer will facilitate the oxidation of the interfering gases selectively, prior to reaching the interface between SE and YSZ. With the catalyst layer applied on top of the sensing layer, SE will occupy less substrate area; hence the sensor can be easily miniaturized into a compact sensor.

The utilization of a catalyst has been proposed previously using oxide-based catalyst for YSZ-based sensor [3-5]. Here, a systematic evaluation of a suitable catalyst material being capable of selectively facilitating the oxidation of C_3H_6, as well as the design of an appropriate SE structure with a physically isolated catalyst layer were investigated, and the detailed sensing characteristics of the developed sensor were

discussed. Unfortunately, the utilization of an integrated catalyst layer is not necessarily effective. Therefore, a method to optimize the sensing performance of the sensor using catalyst layer over sensing layer is introduced and the corresponding morphology and the sensing characteristic toward H_2 were investigated and reported here.

3.2 Experimental

3.2.1 Fabrication of sensing devices

A commercial hemispherically-terminated YSZ tube (8 mol.% Y_2O_3-doped ZrO_2, Nikkato, Japan) was used as the substrate for the sensing and reference electrodes. The physical dimensions of the tube were 300 mm in length; 5 and 8 mm inner and outer diameter, respectively.

The sensing performance stabilization of mixed-potential-type YSZ-based sensors has been proposed via the utilization of an additional YSZ layer in between the SE and the YSZ solid electrolyte [6]. The existence of such an intermediate YSZ (*i*YSZ) layer can stabilize the sensing signal and improve the mechanical stability of SE [6]. Therefore, an *i*YSZ layer was formed in between SE and YSZ solid electrolyte. The YSZ powder (8 mol.% Y_2O_3-doped ZrO_2, Tosoh Corp., Japan) was mixed with an organic binder (α-terpineol). The resulting paste was applied onto the surface of the YSZ tube. Following this, a commercial SnO_2 powder (Kishida Chemical, Japan) was used for fabrication of the SnO_2-based SE. When required, YSZ powder was added into SnO_2 powder and ground in mortar. An organic binder (α-terpineol) was added into the oxide powder mixture to make a uniform paste. The paste was applied onto the surface of the *i*-YSZ layer to form a 3 mm wide banded oxide layer.

In a similar manner, the Al_2O_3 layer was fabricated using commercial nano Al_2O_3

powder (Sigma aldrich, Japan). The Cr_2O_3 catalyst layer was fabricated by mixing the commercial Cr_2O_3 powder (Kishida Chemical, Japan) with the same organic binder to form a paste, which was painted as a 3 mm wide band. Each layer was dried at 130^{o}C in a drying oven overnight, prior to applying the next layer. The Pt paste (Tanaka Kikinzoku, Japan) was applied on the inner side of YSZ tube as the reference electrode (RE). The painted-YSZ tube was then dried at 130^{o}C, and subsequently underwent a sintering process at 1000^{o}C for 2 h.

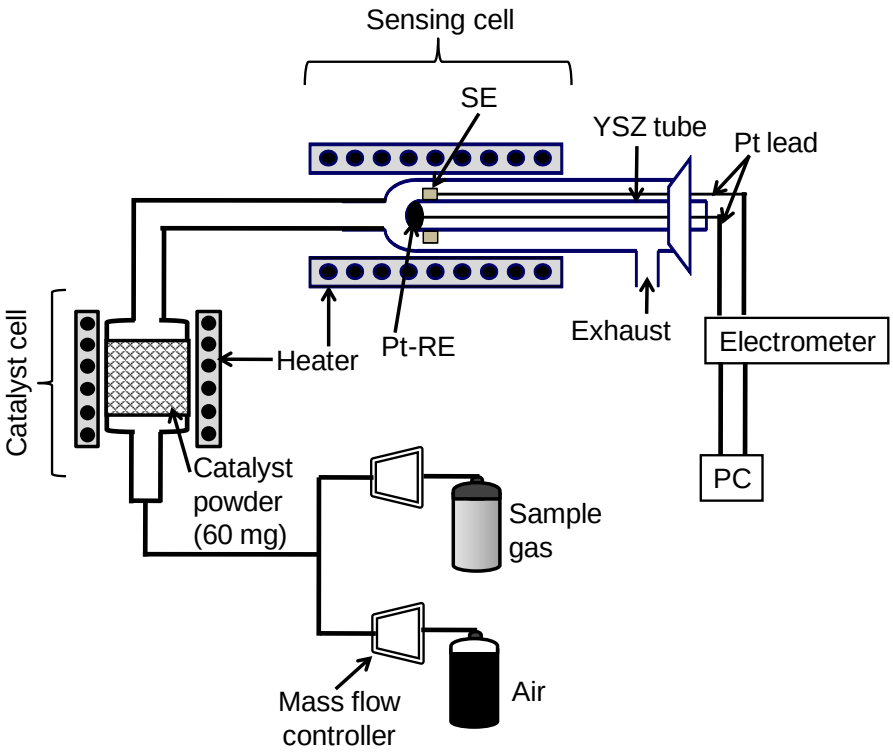

Figure 3.1 Schematic view of the sensing characteristic evaluation system equipped with an upstream quartz catalytic cell. (Reproduced from [10], Copyright 2013, with permission from Elsevier).

3.2.2 Evaluation of sensing properties

The fabricated tubular YSZ-based sensors were assembled in a custom quartz testing cell in close proximity to the gas inlet and connected to a conventional gas-flow apparatus equipped with a high-temperature electric furnace, as depicted in Fig. 3.1. The

evaluation of gas-sensing characteristics was performed at 550^{o}C. The sensor was exposed to the humidified base gas (21 vol.% O_2 + 1 vol.% H_2O in N_2 balance) or the humidified sample gas containing H_2, CO, C_3H_6, CH_4, NO or NO_2 diluted in 21 vol.% O_2 + 1 vol.% H_2O in N_2 balance with a constant gas flow rate of 100 cm^3/min. The sample gas concentration was fixed at 100 ppm for cross-sensitivity measurements. The water vapor concentration was also fixed at 1 vol.%, except during the examination of effect that water vapor has on gas-sensing characteristics. The inner Pt-RE was always exposed to the ambient atmospheric air (Pt/air-RE). The difference in electromotive force (*emf*) between the outer SE connected to the positive terminal of a digital electrometer (R8240, Advantest, Japan), and the inner Pt/air-RE connected to the negative terminal was measured as the sensing signal. The gas sensitivity (Δemf) was defined as the difference between the emf value of the base gas and the sample gas.

3.2.3 Catalyst material investigation

For catalyst material investigation, the evaluation of the gas-phase catalytic activity was conducted with cell arrangement given in Fig. 3.1. The metal-oxide catalyst powder (60 mg) was sintered at 1000^{o}C for 2 h, before placement into a U-shaped quartz tube packed with quartz wool which formed the separate catalyst cell. This catalyst cell was located upstream of the sensing cell. The temperature inside the catalyst cell was maintained at the same temperature as that inside the sensing cell.

3.2.4 Polarization curve measurements

The current-voltage characteristics (polarization curves) were measured by means of an automatic polarization system (HZ-3000, Hokuto Denko, Japan). The potential scan was carried out in potentiodynamic mode at a scan rate of 5 mV/min, in the base

gas (21 vol.% O_2 + 1 vol.% H_2O), as well as in the sample gas containing 100, 400, and 800 ppm H_2 (21 vol.% O_2 + 1 vol.% H_2O). The polarization curve for the electrochemical reaction of H_2 was estimated by subtracting the current value in the base gas from that in sample gas at each potential.

3.2.5 Morphology observation and crystal phase determination of the SE

The morphology of the SE was observed by using a field-emission scanning electron microscope (SEM, JSM-6340F, JEOL, Japan). The crystal structure of the SE layer was examined by means of an X-ray diffractometer (XRD, RINT 2100VLR/PC, Rigaku, Japan) with Cu Kα radiation (λ = 1.5406 Å).

3.3 Results and discussion.

3.3.1 Selection of a suitable catalyst material for selective C_3H_6 oxidation

Initially, a suitable catalyst material that could facilitate the oxidation of C_3H_6 selectively was sought. The catalytic activities of prospective catalyst materials were examined by installing a separate catalyst cell, upstream from the sensing cell (Fig. 3.1). Hence, the catalyst would facilitate the oxidation of unwanted gas components, and the residual gas would be detected by the sensor using SnO_2 (+ 30 wt.% YSZ)-SE in the sensing cell. The relative sensitivity toward both C_3H_6 and H_2 was measured, when the sensor utilizing SnO_2 (+ 30 wt.% YSZ)-SE was set downstream from the catalyst cell.

The relative conversion given in Fig. 3.2 is the emf of the sensor when coupled with the catalyst cell, divided by the emf value of the initial sensor (without the catalyst cell), and multiplied by one hundred. As can be seen from this figure, among the examined metal-oxide catalyst materials, the sensor using SnO_2 (+ 30 wt.% YSZ)-SE together with the Cr_2O_3 powder loaded in the catalyst cell is capable of selectively

facilitating the oxidation of C_3H_6, since it can convert approximately 84% C_3H_6 and as little as 4% H_2. Therefore, Cr_2O_3 was then used as the catalyst material, in order to obtain a sensitive and selective response toward H

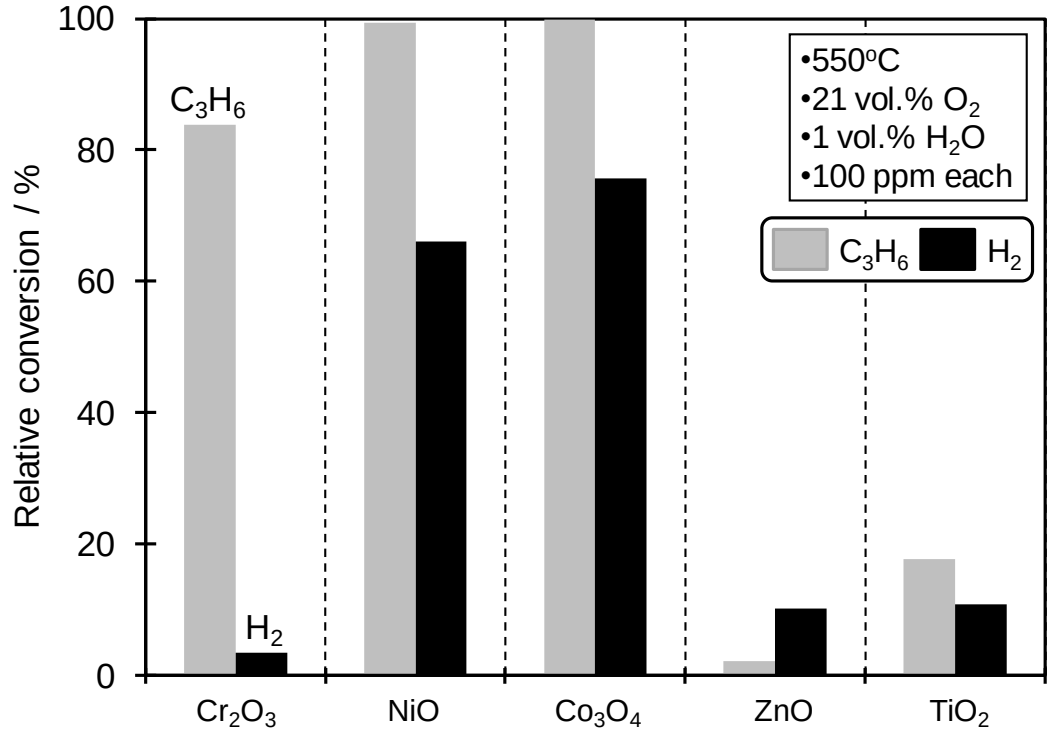

Figure 3.2 Relative sensitivity comparison of the conversion of C_3H_6 and H_2 for the sensor using SnO_2 (+ 30 wt.% YSZ)-SE with different metal oxide catalyst materials placed in the upstream catalyst cell. (Reproduced from [10], Copyright 2013, with permission from Elsevier)

3.3.2. Influence of a Cr_2O_3 catalyst on the sensing characteristic of the sensor using SnO_2 (+ 30 wt.% YSZ)-SE

Figure 3.3 shows the comparison of cross sensitivity to different gases for the sensors utilizing SnO_2-based-SEs or Cr_2O_3–SE at 550°C under humid conditions. The sensor using SnO_2-SE was observed to give high responses toward H_2 (Δemf = -101 mV) and C_3H_6 (Δemf= -121 mV), as shown in Fig. 3.3(a). As the first step, Cr_2O_3 was directly deposited on top of the SnO_2 (+ 30 wt.% YSZ)-SE layer as a laminated SE,

henceforth denoted as Cr_2O_3/SnO_2 (+ 30 wt.% YSZ)-SE. The sensing characteristics of the sensor using Cr_2O_3/SnO_2 (+ 30 wt.% YSZ)-SE is presented in Fig. 3.3 (b). As shown here, the sensitivity toward H_2 for the present sensor decreased, when compared with that of the sensor using the parent SnO_2-SE, from approximately -101 mV to 0 mV. In addition, lower response toward C_3H_6 was also seen, where the Δemf was observed to decrease from about -121 mV to -15 mV.For further investigation, Cr_2O_3 was then used as an additive, where 1 wt.% Cr_2O_3 was added into SnO_2 to form a mixture. The sensing characteristic of the sensor utilizing SnO_2 (+ 1 wt.% Cr_2O_3)-SE is given in Fig. 3.3 (c).

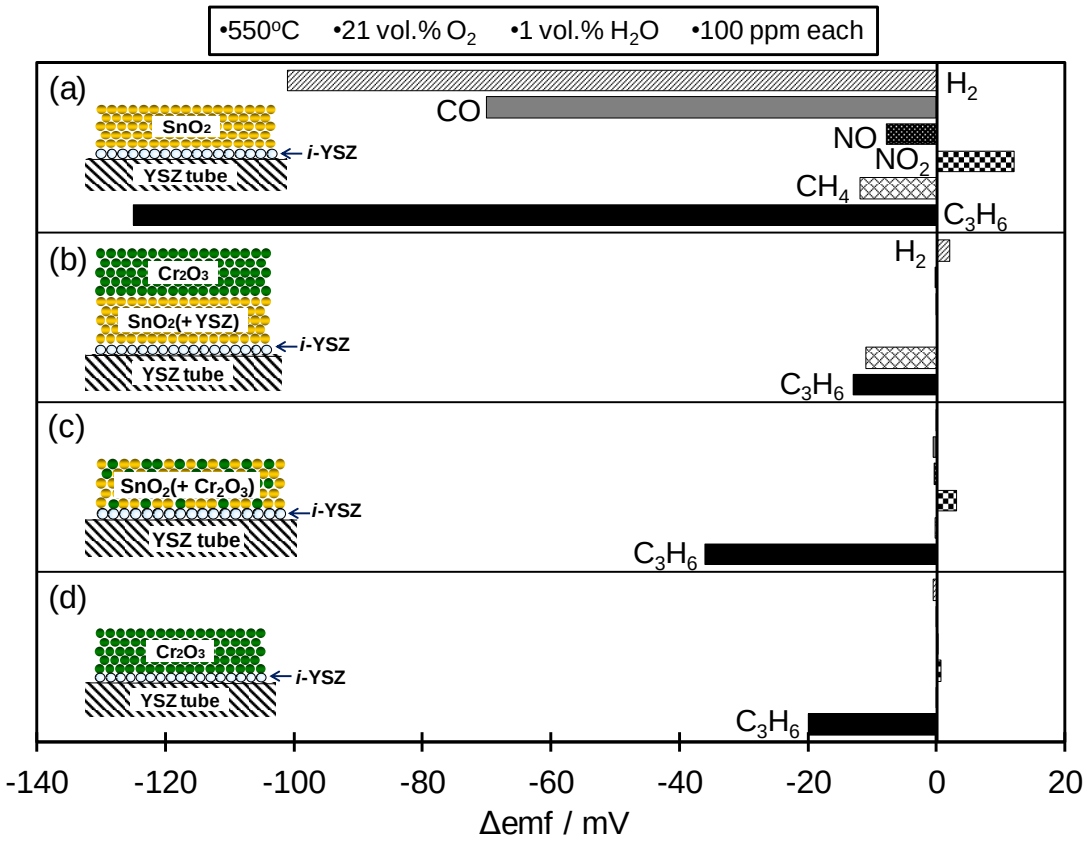

Figure 3.3 Cross sensitivity comparison toward different examined gases for the sensor utilizing (a) SnO_2-SE, (b) Cr_2O_3/SnO_2 (+ 30 wt.% YSZ)-SE, (c) SnO_2 (+ 1 wt.% Cr_2O_3)-SE and (d) Cr_2O_3-SE, at operational temperature of 550°C. (Reproduced from [10], Copyright 2013, with permission from Elsevier)

The addition of a relatively small amount of Cr_2O_3 has also drastically altered the sensing characteristics of the parent SnO_2-SE, where the response toward H_2 (Δemf) decreased from -101 to 0 mV. However, the sensing characteristics of the sensor using SnO_2 (+ 1 wt.% Cr_2O_3)-SE as well as the sensor using Cr_2O_3/SnO_2 (+ 30 wt.% YSZ)-SE was observed to be similar with that of the parent Cr_2O_3-SE (Fig. 3 (d)), that gave negligible response toward H_2 and low response toward C_3H_6 (Δemf = -20 mV).

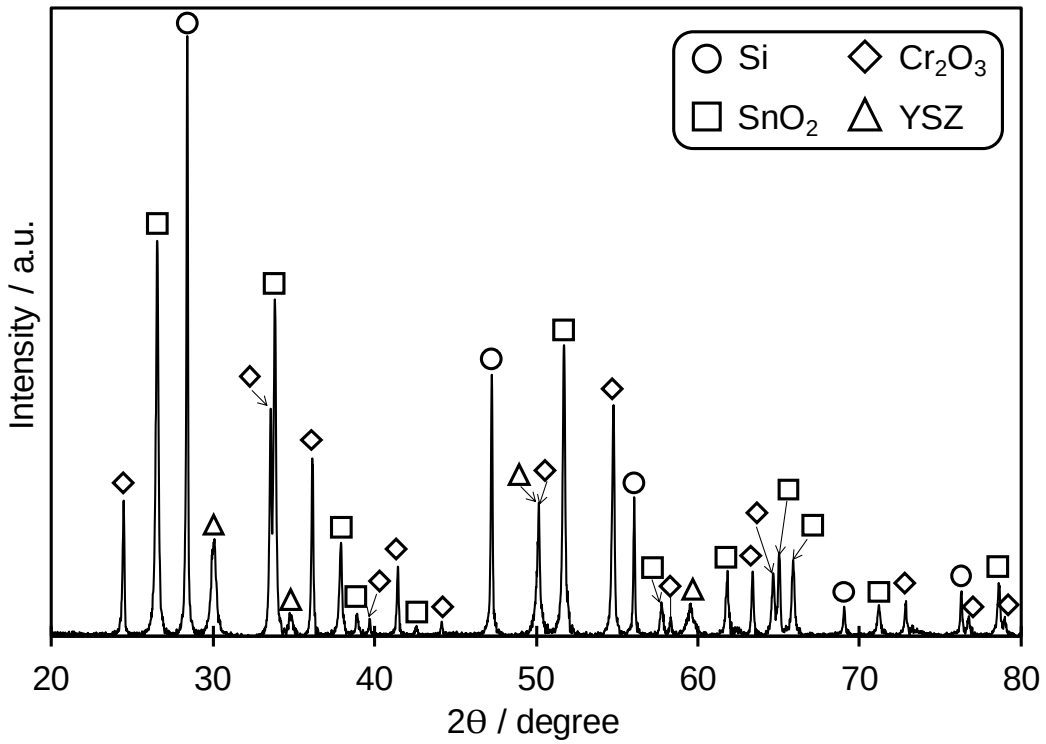

Figure 3.4 XRD pattern for SnO_2 (+ 30 wt.% YSZ)+ Cr_2O_3 after sintering at 1000^{o}C for 2 h. (Reproduced from [10], Copyright 2013, with permission from Elsevier)

The crystal phase composition of the Cr_2O_3/SnO_2 (+ 30 wt.% YSZ) mixture was examined. Figure 3.4 shows the XRD pattern of the SnO_2 (+ 30 wt.% YSZ) and Cr_2O_3 with ratio 1:1 in weight after sintering at 1000^{o}C for 2 h. The peaks are assigned to SnO_2 (JCPDS no.: 41-1445), YSZ (JCPDS no.: 48-0224) and Cr_2O_3 (JCPDS no.: 38-1479). The peaks of silicon (Si) are generated from the silicon powder that was used

as a calibration standard for this measurement, and is in good agreement with Si reference (JCPDS no.: 27-1402). The results in Fig. 3.4 indicated that there was no formation of a new compound after the sintering process, when Cr_2O_3 was utilized as an additive into SnO_2-SE, as well as when Cr_2O_3 was employed as the catalyst layer on top of the SnO_2 (+ 30 wt.% YSZ)-SE layer.

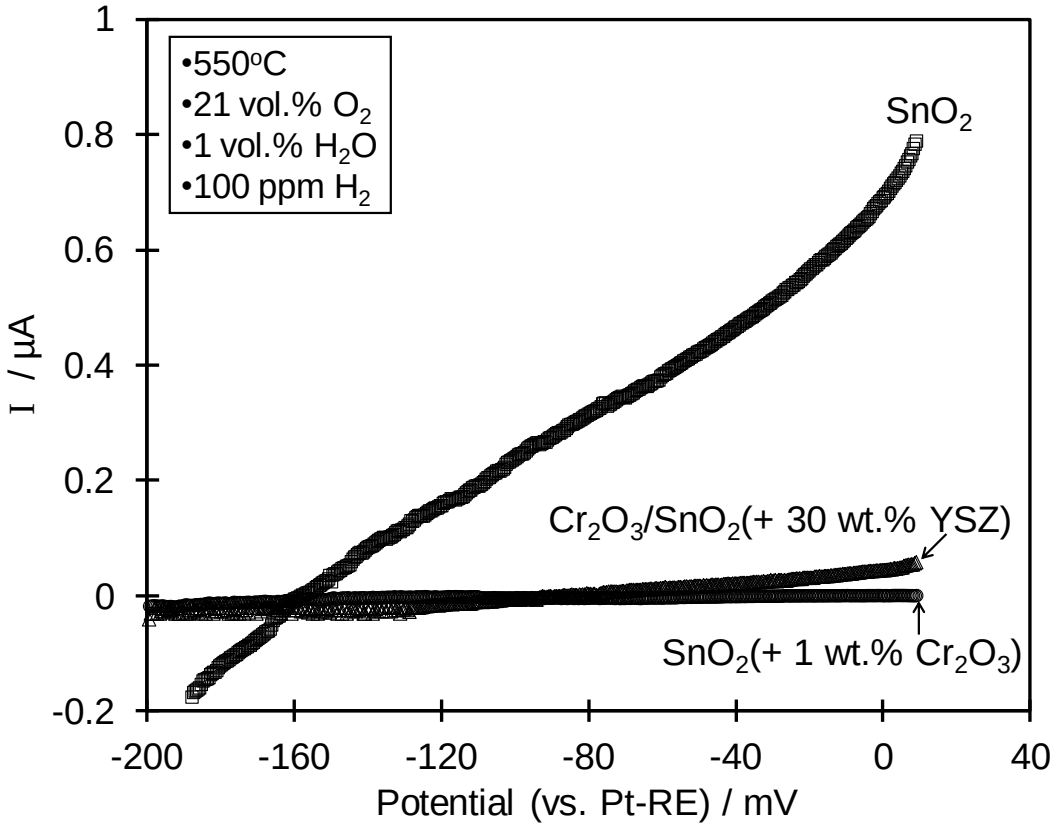

Figure 3.5 The modified polarization curves of electrochemical reactions of H_2 for the sensor utilizing SnO_2-SE, Cr_2O_3/SnO_2 (+ 30 wt.% YSZ)-SE and SnO_2 (+1 wt.% Cr_2O_3)-SE. (Reproduced from [10], Copyright 2013, with permission from Elsevier)

The electrochemical activity of the three different SEs was examined in detail via several polarization-curve measurements. Figure 3.5 is the modified polarization curves for the electrochemical reaction of H_2. The generated current of H_2 reactions for the sensor using Cr_2O_3/SnO_2 (+ 30 wt.% YSZ)-SE or the SnO_2 (+ 1 wt.% Cr_2O_3)-SE was

found to be much lower than the generated current from the sensor using SnO_2-SE. The generated current of the electrochemical reaction of H_2 for both sensors using Cr_2O_3/SnO_2 (+ 30 wt.% YSZ)-SE and SnO_2 (+ 1 wt.% Cr_2O_3)-SE was observed to be almost identical. This suggests the penetration of Cr_2O_3 particles into the SnO_2-SE layer, potentially reaching the interface between SE and YSZ, when Cr_2O_3 was deposited directly on top of SnO_2 (+ 30 wt.% YSZ)-SE. Therefore, the decreased electrochemical reaction current for the sensor using Cr_2O_3/SnO_2 (+ 30 wt.% YSZ)-SE is believed to be due to the penetration of Cr_2O_3 particles into the SnO_2 layer, which might reach the interface between SE and YSZ. Therefore, the existence of Cr_2O_3 at the SE/YSZ interface may have decreased the catalytic activity toward the electrochemical reaction of H_2. Since the existence of Cr_2O_3 across the SE, as well as at the interface between SE and YSZ could change the catalytic activity of the electrochemical reactions toward H_2. Therefore for the successful utilization of Cr_2O_3 as a catalyst layer, a barrier layer is necessary to prevent the penetration of Cr_2O_3 particles into the SnO_2 layer.

3.3.3 Sensing characteristic of the sensor using SnO_2 (+ 30 wt.% YSZ)-SE enveloped with Al_2O_3 and coated with Cr_2O_3

A barrier layer that covered the entire SE surface was employed to prevent the penetration of Cr_2O_3 particles into SnO_2 layer which could ultimately migrate to the interface between SE and YSZ. As a barrier layer material, alumina (Al_2O_3) was selected, owing to its stable and relatively inert properties [7]. Due to the inertness of Al_2O_3, it is believed that the formation of a new compound even when Al_2O_3 was sandwiched between the SE and the catalyst layer is unlikely, as is also the generation of competing catalytic activity when deposited over the SnO_2 electrode. In addition, a dense intermediate layer that is capable of preventing the intrusion of Cr_2O_3 particles

into the SE layer can be attained by using the nano-sized Al_2O_3, as demonstrated here. Furthermore, the Al_2O_3 layer was designed to envelop the SE layer; so gases could not permeate into the SE from the side walls of the SE itself.

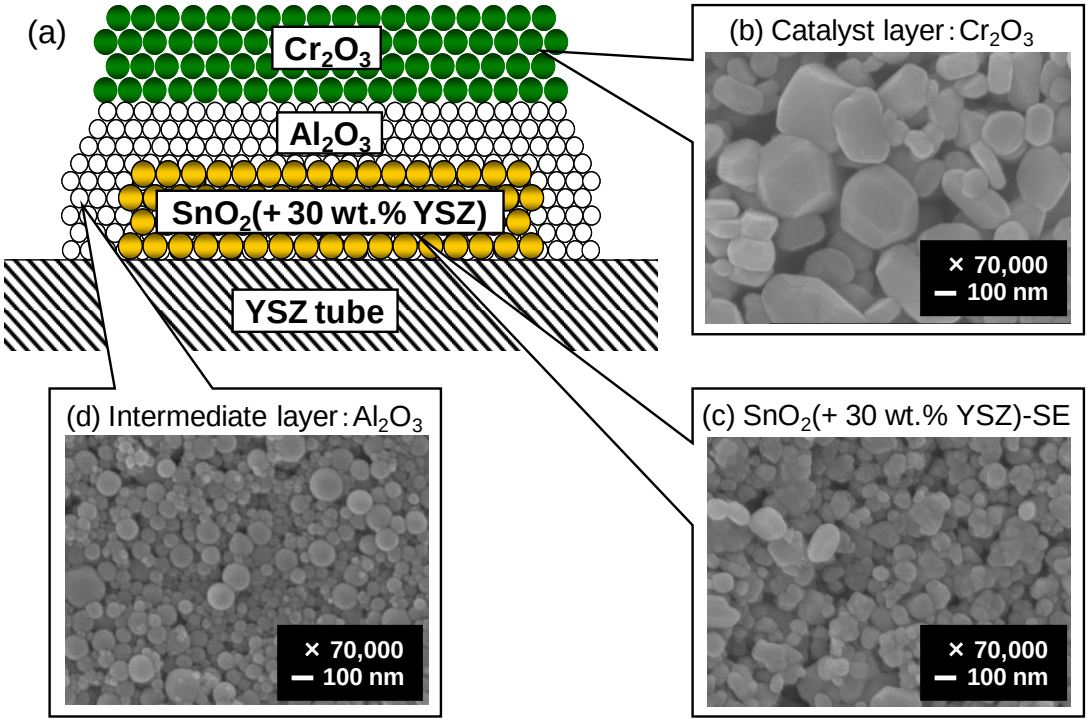

Figure 3.6 (a) Schematic view of the sensor using $Cr_2O_3/Al_2O_3/SnO_2$ (+ 30 wt.% YSZ)-SE and the representative SEM images for (b) the catalyst layer (Cr_2O_3), (c) the sensing electrode (SnO_2 (+ 30 wt.% YSZ)) layer and (d) the barrier layer (Al_2O_3), after sintering at 1000°C for 2 h. (Reproduced from [10], Copyright 2013, with permission from Elsevier)

The schematic view of the sensor construction utilizing SnO_2 (+ 30 wt.% YSZ)-SE that was enveloped by the intermediate layer of Al_2O_3 and coated with a Cr_2O_3 catalyst layer, henceforth denoted as $Cr_2O_3/Al_2O_3/SnO_2$ (+ 30 wt.% YSZ)-SE, was presented in Fig. 3.6 (a). The grain morphology of each layer after sintering at 1000°C for 2 h is visible in the SEM images presented in Fig. 3.6 (b-d). A rather porous surface was observed for the sintered Cr_2O_3 catalyst material with faceted polygonal-shaped

particles observed to approximately range from 80 to 400 nm in size (Fig. 3. 6 (b)). SnO_2 has a slightly porous surface, also with polygonal-shaped particles, and the particle size is found to approximately range from 10 to 300 nm (Fig. 6 (c)). While, Al_2O_3 had a comparatively denser morphology than the previous two samples, with smaller spherically-shaped particles approximately 10 to 200 nm in diameter (Fig. 3.6 (d)).

The sensing characteristics of the sensor utilizing $Cr_2O_3/Al_2O_3/SnO_2$ (+ 30 wt.% YSZ)-SE was investigated at 550^oC under the same testing conditions against Pt/air-RE. Figure 3.7 (a) shows the cross sensitivity of the newly developed sensor toward different examined gases. As can be seen here, the utilization of an intermediate layer between the SE and the catalyst layer has successfully diminished the unwanted response toward interfering gases, since the sensitivity to other gases was observed to be less than –15 mV and a sensitive response toward H_2 (Δemf about -70 mV) was successfully retained. Additionally, the Al_2O_3 layer which envelops the surface of the SE, with its narrow diffusion channels, is also believed to capable of hindering the penetration of gases from the electrode sidewalls.

Figure 3.7 (b) shows the typical response transients of the developed sensor toward different concentrations of H_2 (20-800 ppm) at an operational temperature of 550^oC. This sensor exhibited a quick response and recovery, since the 90% response time was observed to be approximately 10 s toward 100 ppm H_2 and the 90% recovery time was approximately 30 s upon the introduction of 21 vol.% O_2. As shown in Fig. 3.7 (c), the present sensor was found to have a linear relationship between the sensitivity and H_2 concentration on a logarithmic scale, indicating the sensing mechanism of the sensor was in good agreement with mixed potential model [8-10].

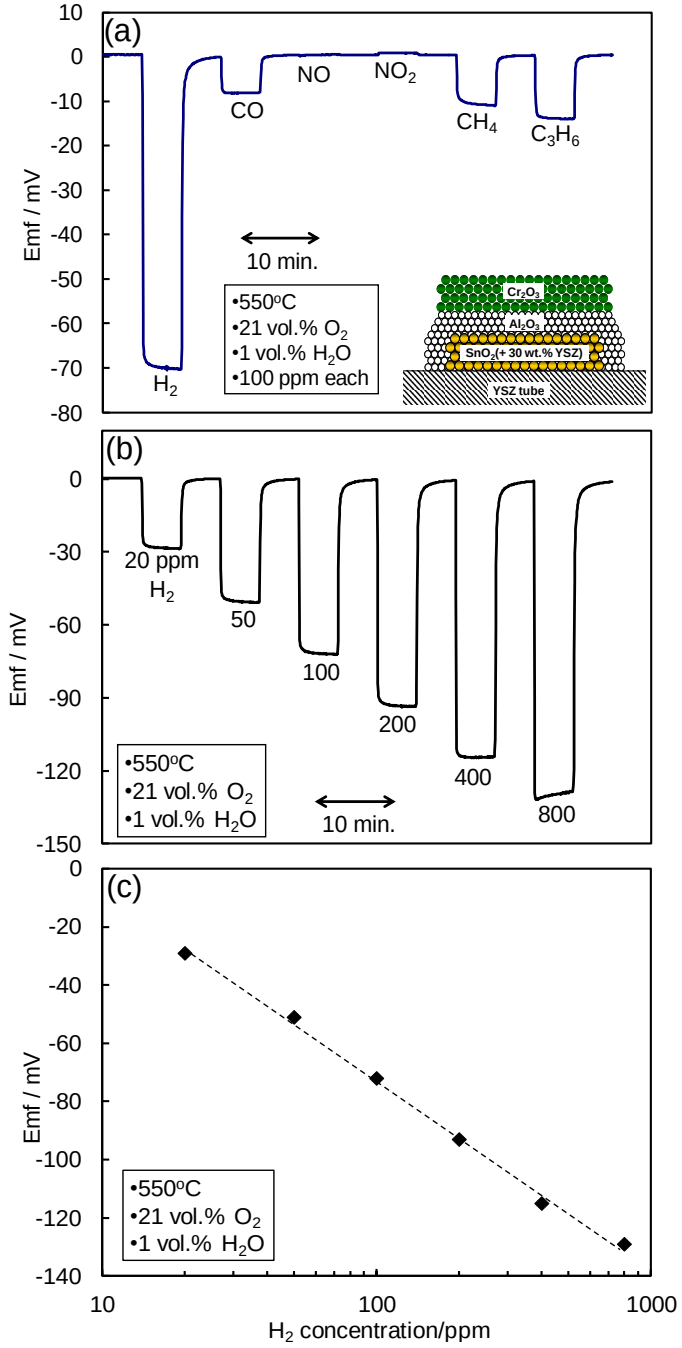

Figure 3.7 (a) Cross sensitivity toward different gases for the sensor using $Cr_2O_3/Al_2O_3/SnO_2$ (+ 30 wt.% YSZ)-SE, (b) response transients toward different H_2 concentration and (c) sensitivity dependency on the H_2 concentration, at operational temperature of 550°C under humid conditions. (Reproduced from [10], Copyright 2013, with permission from Elsevier)

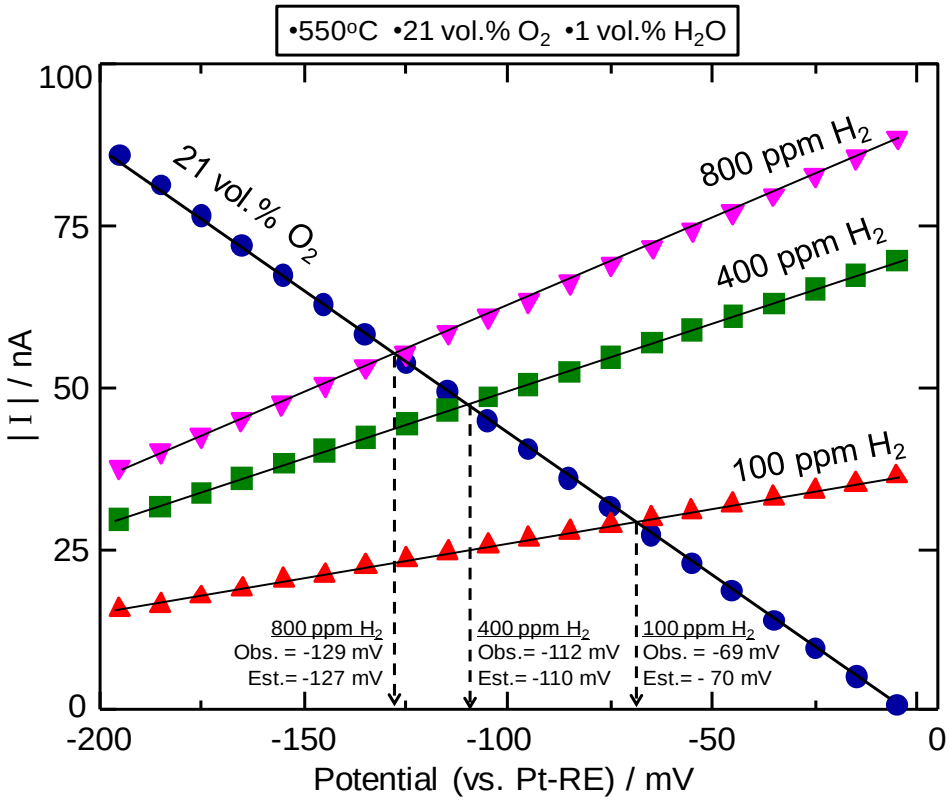

Figure 3.8 The modified polarization curves of the sensor using $Cr_2O_3/Al_2O_3/SnO_2$(+ 30 wt.% YSZ)-SE at 550°C under humid conditions for different concentrations of H_2. (Reproduced from [10], Copyright 2013, with permission from Elsevier)

The mixed-potential model can be rationalized by interpreting the polarization curves. The mixed potential is estimated from intersection point of modified anodic and cathodic polarization curves. Figure 3.8 shows the modified polarization-curves for the anodic reaction of H_2 at different H_2 concentrations as well as for the cathodic reaction of O_2 in 21 vol.% O_2 at 550°C. The current of the anodic curves increased with increasing H_2 concentration. The estimated mixed potential for each examined concentration is shown in Fig. 3.8 as well. It can be seen that the observed emf response is in good accordance with the estimated mixed-potential obtained from the polarization curves. This confirms that the sensing mechanism of the developed sensor is based on the mixed potential model [8, 11, 12].

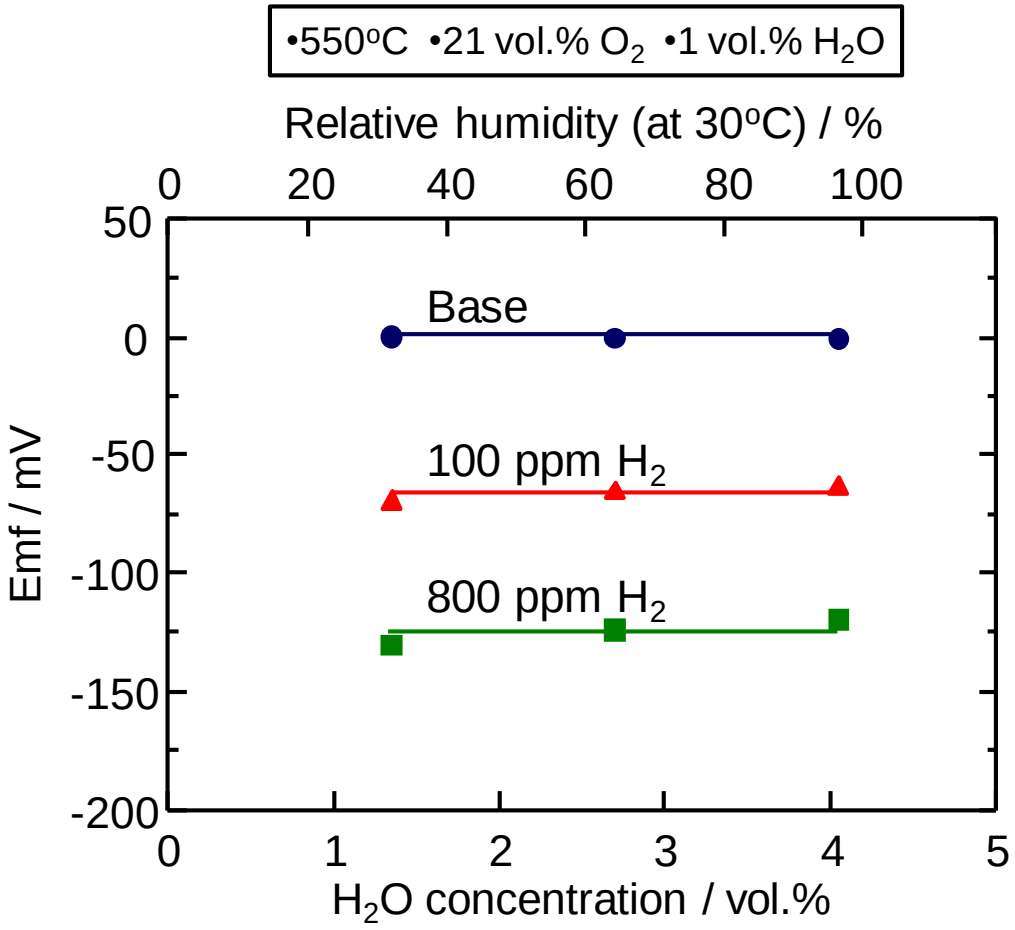

Figure 3.9 H_2 sensitivity dependency on the change in water vapor concentration for the sensor utilizing $Cr_2O_3/Al_2O_3/SnO_2$(+ 30 wt.% YSZ)-SE at an operational temperature of 550°C. (Reproduced from [10], Copyright 2013, with permission from Elsevier)

In order to ascertain the potential of the sensor to be used in realistic conditions, the sensor using $Cr_2O_3/Al_2O_3/SnO_2$ (+ 30 wt.% YSZ)-SE was exposed to H_2 in a gas mixture with different water vapor concentrations, the obtained results are shown in Fig. 3.9. The base line as well as the emf response toward 100 and 800 ppm H_2 was found to be indifferent with the change in water vapor concentration, within the range of 1-5 vol.% H_2O, indicating the ability of the developed sensor to work in environments where water vapor fluctuations occur. However, the sensor using $Cr_2O_3/Al_2O_3/SnO_2$(+ 30 wt.% YSZ)-SE can only exhibited a relatively stable response for about 20 days.

After 20 days, the sensitivity was gradually decreased. This might be a constraint for further development of the sensor using $Cr_2O_3/Al_2O_3/SnO_2$(+ 30 wt.% YSZ)-SE that need to be solved before working in real applications.

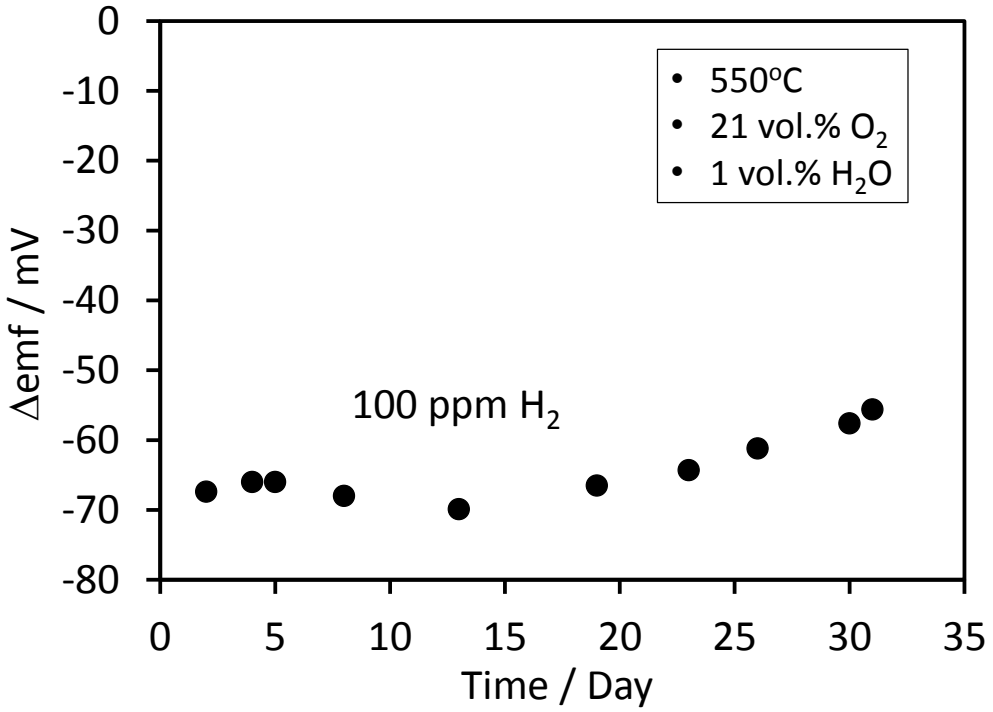

Figure 3.10 The short-term stability of the sensor utilizing $Cr_2O_3/Al_2O_3/SnO_2$(+ 30 wt.% YSZ)-SE at an operational temperature of 550°C.

3.4 Conclusions

A systematic investigation of catalyst materials revealed that Cr_2O_3 is capable of facilitating the oxidation of C_3H_6 selectively. However, the H_2 sensitivity for the sensor using Cr_2O_3/SnO_2 (+ 30 wt.% YSZ)-SE as well as the sensor using SnO_2(+ 1 wt.% Cr_2O_3)-SE, was found to have decreased, with respect to the SnO_2(+ 30 wt.% YSZ)-SE. The penetration of Cr_2O_3 into the SE layer, reaching the interface between SE and YSZ is believed to be the reason for the decreased H_2 response, indicated by the decreased

generated current visible in the polarization curve of H_2 for the sensor using Cr_2O_3/SnO_2(+ 30 wt.% YSZ)-SE and SnO_2 (+ 1 wt.% Cr_2O_3)-SE. When Al_2O_3 was employed as barrier layer sandwiched between SE and the catalyst layer, the newly developed sensor could generate sensitive and selective responses toward H_2. This indicates that the Al_2O_3 barrier layer successfully prevents the penetration of Cr_2O_3 particles into SnO_2-SE layer. The observed sensitivity for this sensor was found to be in good agreement with the estimated mixed-potential which was obtained from the polarization curves, indicating the sensing mechanism was based on the mixed-potential model.

(Some of the contents in this chapter is reproduced from [13], Copyright 2013, with permission from Elsevier)

References

[1] P.E. Norio Miura, Vladimir V. Plashnitsa, Taro Ueda, Ryotaro Wama, Masahiro Utiyama, Solid State Electrochemical Gas Sensing, in: G.F. Elisabetta Comini, Giorgio Sberveglieri (Ed.) Solid State Gas Sensing, Springer Science + Business Media, LLCC, USA, 2009, p. 181.

[2] M. Yamaguchi, S.A. Anggraini, Y. Fujio, M. Breedon, V.V. Plashnitsa, N. Miura, *Electrochimica Acta*, 76(2012) 152-8.

[3] H. Okamoto, H. Obayashi, T. Kudo, *Solid State Ionics*, 1(1980) 319-26.

[4] Y. Tan, T.C. Tan, *Journal of The Electrochemical Society*, 141(1994) 461-7.

[5] N. Li, T.C. Tan, H.C. Zeng, *Journal of The Electrochemical Society*, 140(1993) 1068-73.

[6] Y. Fujio, V.V. Plashnitsa, P. Elumalai, N. Miura, *Talanta*, 85(2011) 575-81.

[7] J. Jia, K. Haraki, J.N. Kondo, K. Domen, K. Tamaru, *The Journal of Physical Chemistry B*, 104(2000) 11153-6.

[8] S.A. Anggraini, V.V. Plashnitsa, P. Elumalai, M. Breedon, N. Miura, *Sensors and Actuators B: Chemical*, 160(2011) 1273-81.

[9] V.V. Plashnitsa, S.A. Anggraini, N. Miura, *Electrochemistry Communications*, 13(2011) 444-6.

[10] V.V. Plashnitsa, V. Gupta, N. Miura, *Electrochimica Acta*, 55(2010) 6941-5.

[11] J. Park, B.Y. Yoon, C.O. Park, W.-J. Lee, C.B. Lee, *Sensors and Actuators B: Chemical*, 135(2009) 516-23.

[12] T. Sato, V.V. Plashnitsa, M. Utiyama, N. Miura, *Electrochemistry Communications*, 12(2010) 524-6.

[13] M. Yamaguchi, S. A. Anggraini, Y. Fujio, T. Sato, M. Breedon, N. Miura, *International Journal of Hydrogen Energy*, 38 (2013) 305-12.

Chapter 4

H_2 Sensing Characteristics of the Sensor Utilizing $Zn_3Ta_2O_8$-based Sensing Electrode

4.1 Introduction

Dissimilar to the method that has been employed in Chapter 2, where various oxides were initially examined as a prospective H_2 sensitive material, ZnO is proposed to be used here as the base SE-material for H_2 sensor. The mixed-potential type sensor using ZnO-SE has been reported to exhibit relatively high sensitivity toward H_2 [1]. In this chapter, the proposed strategy to enhance the sensitivity as well as selectivity of YSZ-based sensor using ZnO-based-SE was conducted by incorporating another compound into ZnO. As has been mentioned in Chapter 1, the utilization of noble metal as an SE component may raise the sensor fabrication cost. Considering that, instead of noble metal used as an additive, the effort in improving H_2 sensitivity and selectivity was performed by mixing another metal oxide into ZnO-SE.

In chapter 1, it has been discussed that in accompany to the high H_2 sensitivity generated by the sensor using ZnO-SE, high responses to CO and HCs might interfere the sensitivity to H_2 [1]. In contrast to ZnO, the utilization of Ta_2O_5 as an additive has been reported to improve the gas selectivity [2] or to generate high sensitivity toward H_2 [3]. Based on those reported finding regarding Ta_2O_5 addition, in this chapter, investigation on changes in sensing characteristic toward H_2 due to the variation of Ta_2O_5 addition into ZnO was initially conducted. An improvement in sensitivity and selectivity was achieved by increasing sintering temperature of SE. The changes in morphology and electrode composition by increases in both of Ta_2O_5 additions and

sintering temperature were investigated and elucidated here.

4.2 Experimental

4.2.1 Sensor Fabrication

The utilization of an additional YSZ layer between SE and a YSZ tube has been reported to facilitate the sensing-signal stabilization and to improve the mechanical stability of the SE/YSZ interface [4], Thus, the YSZ paste was initially prepared by mixing YSZ powder (8 mol.% Y_2O_3-doped ZrO_2, Tosoh, Japan) with α-terpineol, and the resulting paste was applied onto the surface of a YSZ tube (8 mol.% Y_2O_3-doped ZrO_2, Nikkato, Japan) to form an intermediate YSZ layer (*i*-YSZ). The physical dimensions of the YSZ tube were: 300 mm in length; 5 and 8 mm in inner and outer diameter, respectively.

The powder mixture of ZnO (99.99%, Kojundo Chemical, Japan) and Ta_2O_5 (99.99%, Kojundo Chemical, Japan) was ground in a mortar and subsequently mixed with α-terpineol, forming a uniform paste. The obtained paste was applied onto the surface of *i*-YSZ layer to form a 4 mm-wide banded SE layer. A commercial Pt paste (Tanaka Kikinzoku, Japan) was applied on the inner surface of the YSZ tube, forming a reference electrode (RE). The painted-YSZ tube was then dried at 130^{o}C and sintered at various temperatures (1000, 1100, 1200, 1300 and 1400^{o}C) for 2 h in an atmospheric air.

4.2.2 Sensing-performance Evaluation

The fabricated YSZ-based sensor was assembled in a custom-made quartz testing-cell in a close proximity to the gas inlet, and connected to a conventional gas-testing system equipped with a high-temperature electric furnace and a mass-flow

controller system. The evaluation of gas-sensing characteristics was performed at a constant operating temperature of 600^{o}C.

The sensor was exposed alternately to the humidified base-gas (5 vol.% O_2 + 5 vol.% H_2O + N_2 balance) or the humidified sample gas (containing each of H_2, CO, C_3H_8, C_3H_6, CH_4, NH_3, NO and NO_2, diluted with the base gas). To examine the ability of the sensor under standard atmospheric condition, the sensor was also tested by flowing the humidified different base-gas (21 vol.% O_2 + 1.3 vol.% H_2O + N_2 balance) or the sample gas diluted with this base gas. The total gas flow-rate was set to 100 $cm^3 \cdot min^{-1}$. The inner Pt electrode was always exposed to an ambient air, functioning as Pt/air-RE, while SE was exposed to the sample gas or the base gas. The difference in potential (*emf*) between SE and Pt/air-RE was measured as the sensing signal. The gas sensitivity (Δemf) was defined as the difference between the *emf* value in the base gas and that in the sample gas.

4.2.3 Polarization Curve Measurements

The measurement of current-voltage (polarization) curves was conducted by means of an electrochemical analyzer (Autolab®, PGSTAT30, Eco-Chemie, Netherlands). The polarization curves were measured by the potentiodynamic method, with a constant scan rate of 8 $mV \cdot min^{-1}$ by using a two-electrode configuration in both of the base gas and the sample gas. The cathodic polarization curve was obtained by plotting the applied potential against the absolute current value. The modified polarization curve for the anodic reaction of H_2 was obtained by subtracting the current value in the base gas from that in the sample gas at each potential.

4.2.4 Morphology and Crystal Structure of SE

The morphological change of the SE materials after sintering at high temperatures were observed by means of a field-emission scanning electron microscope (FE-SEM, JSM-6340F, JEOL, Japan), operated at 5 kV. The change in crystal structure of the SE after sintering was examined via an X-ray diffraction analysis system (XRD, RINT 2100VLR/PC, Rigaku, Japan) with a Cu Kα X-ray source (λ = 1.5406 Å). To calibrate all XRD patterns, an internal Si reference powder (RSRP-43275G, Rigaku, Japan) was incorporated into the samples after sintering.

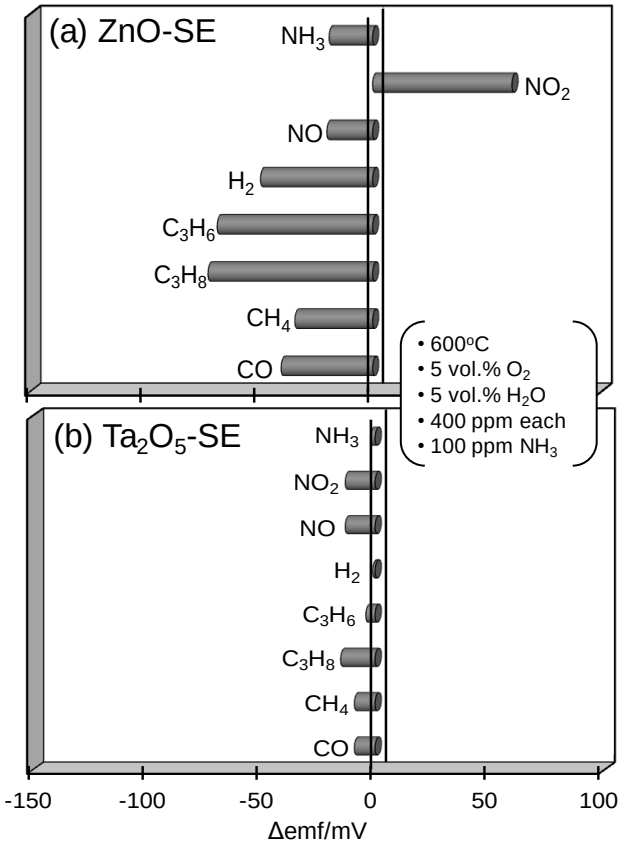

Figure 4.1 The cross sensitivity of the sensors using each of (a) ZnO- and (b) Ta_2O_5-SE sintered at 1000°C, operating at 600°C under humid conditions. (Reproduced from [5] Copyright 2012 and from [13] Copyright 2013 with permission from The Electrochemical Society)

4.3 Results and discussion.

4.3.1 Effect of Ta_2O_5 addition into ZnO-SE on H_2 Sensitivity

The sensing characteristics of the sensors using each of parental metal oxides (ZnO and Ta_2O_5) after sintering at 1000°C are shown in Fig. 4.1. The sensor using ZnO-SE was found to be sensitive toward H_2, CO, NO_2 and HCs gases (Fig. 4.1(a)). Conversely, the sensor using Ta_2O_5-SE generated negligible responses to all examined gases (Fig. 4.1(b)). With the aspiration to improve the selectivity toward H_2 of the sensor using ZnO-SE, Ta_2O_5 was then incrementally added into ZnO, and the sensing performances of these sensors using each of the resulting SE materials were examined [5].

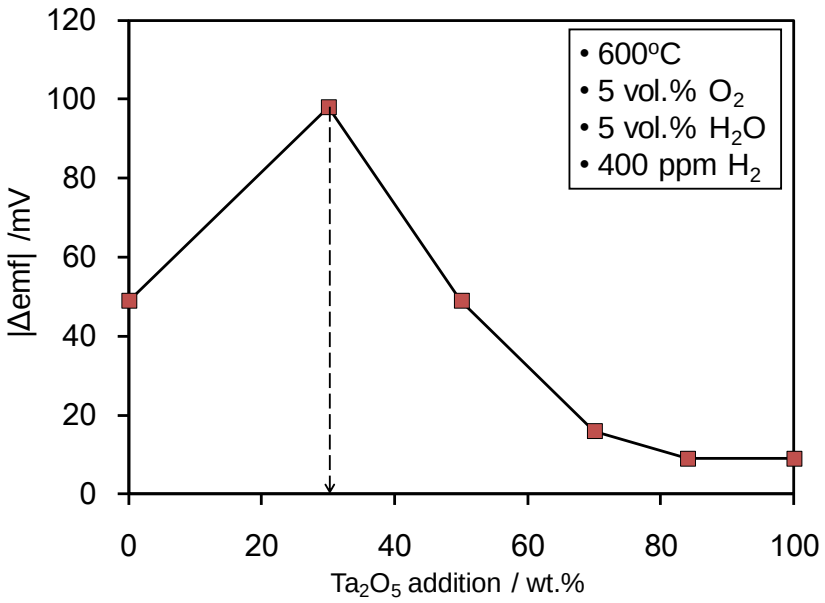

Figure 4.2 The effect of Ta_2O_5 addition into ZnO-SE on H_2 sensitivity (sintering temperature: 1000°C, operated temperature: 600°C). (Reproduced from [5] Copyright 2012 and from [13] Copyright 2013 with permission from The Electrochemical Society)

The effect of Ta_2O_5 addition on the H_2 sensing characteristics of the sensor using ZnO-based SE after sintering at 1000°C for 2 h is presented in Fig. 4.2. It is seen that the addition of 30 wt.% Ta_2O_5 is found to give the highest sensitivity toward H_2, when compared with other mixtures as well as the parent metal oxides [5].

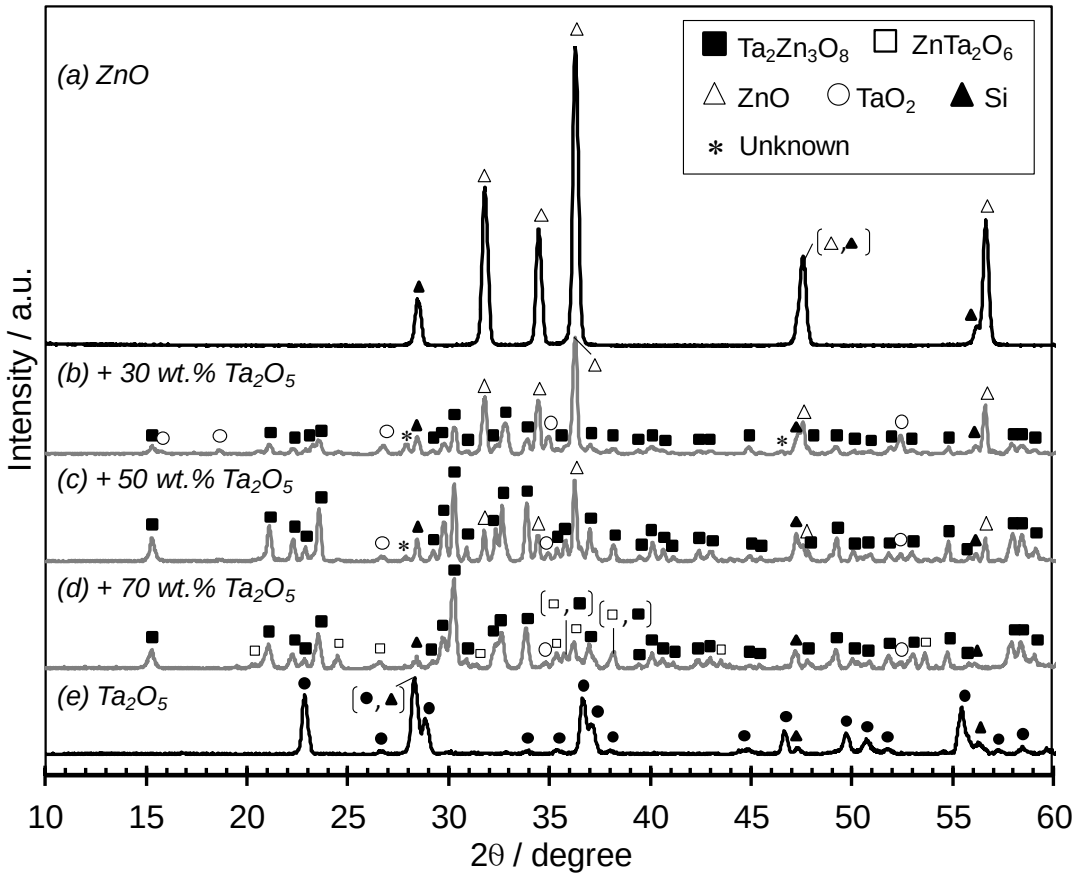

Figure 4.3 The XRD patterns of (a) ZnO added with (b) 30 wt.%, (c) 50 wt.%, (d) 70 wt.% Ta_2O_5 as well as (e) Ta_2O_5, after sintering at 1000°C for 2 h. (Reproduced from [13] Copyright 2013 with permission from The Electrochemical Society)

To investigate the change in the sensing performance toward H_2, the change in the crystal structure with different additions of Ta_2O_5 into ZnO after sintering at 1000°C for 2 h was examined by means of XRD (Fig. 4.3). Figure 4.3 (b) and (c) show that the addition of 30 and 50 wt.% Ta_2O_5 results in a similar mixture of compounds which are composed of ZnO (JCPDS no. 36-1451), $Ta_2Zn_3O_8$ (JCPDS no. 20-1237) and TaO_2 (JCPDS no. 77-2305). However, there are some peaks that are unable to be identified, and they are assigned as an asterisk in the XRD spectra. Further increase in Ta_2O_5 addition up to 70 wt.% was observed to form a mixture consisting of $Ta_2Zn_3O_8$ and $ZnTa_2O_6$ (JCPDS no. 76-1826) (Fig. 4.3 (d). It can be inferred from Figs.4.2 and 4.3 that

there is a correlation between the resulting mixture (the resulting chemical compounds) and the H_2 sensitivity. Although the resulted electrode composition was similar when the Ta_2O_5 addition was 30 and 50 wt.%, the H_2 sensitivity was observed to be different in both cases.

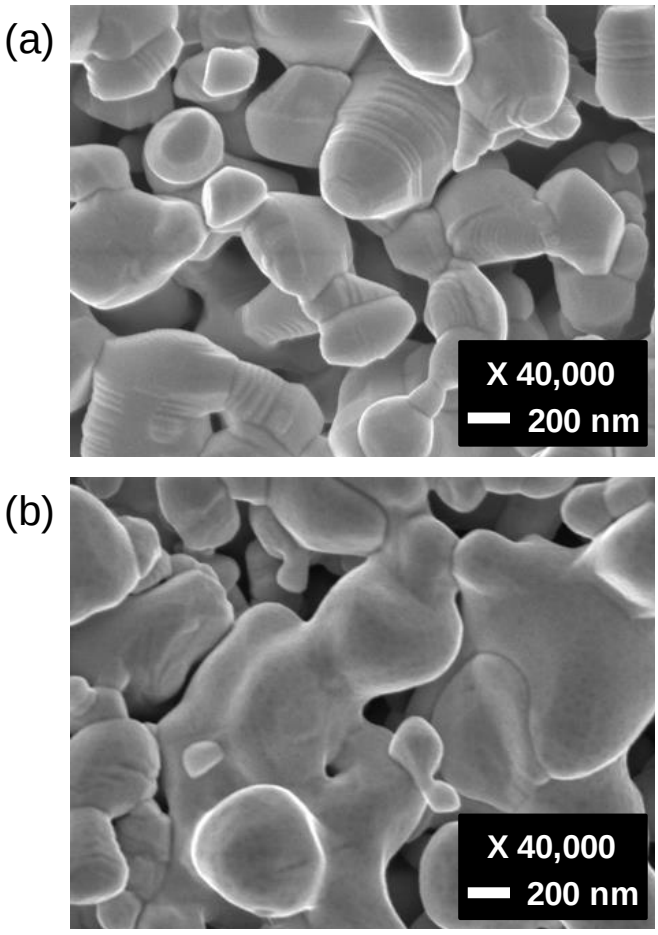

Figure 4.4 The SEM image comparison of the surface morphology of (a) ZnO(+ 30 wt.% Ta_2O_5) and (b) ZnO(+ 50 wt.% Ta_2O_5) after sintering at 1000^{o}C for 2 h. (Reproduced from [13] Copyright 2013 with permission from The Electrochemical Society)

Such a difference in the sensing characteristic toward H_2 can be explained by one or a combination of the following points. The first one is the change in SE morphology with different Ta_2O_5 addition (Fig. 4.4). After sintering at 1000^{o}C, the addition of 30 wt.% Ta_2O_5 into ZnO was found to form a polygonal particles with the stepped surface

and the size ranging from 200 nm to 1 μm (Fig. 4.4 (a)). When the Ta_2O_5 addition rose to 50 wt.%, the resulting composite was composed of smooth-surfaced polygonal particles with the size ranging from 200 nm to 1.5 μm (Fig. 4.4 (b)). This smooth surface may have an intrinsically lower specific surface-area, which would lead to decrease a number of active site for the electrochemical reactions at the SE/YSZ interface.

The second explanation can be ascribed to the decrease of the ZnO fraction in SE, as observed by the change in the relative XRD peak intensity of ZnO to $Ta_2Zn_3O_8$, given in Fig. 4.3 (b) and (c). Since ZnO-SE gives relatively high sensitivity to almost all examined gases (Fig. 4.1 (a)), the presence of ZnO may contribute to the increase in H_2 sensitivity. As shown in Fig. 4.3 (b), XRD pattern for ZnO(+ 30 wt.% Ta_2O_5)-SE exhibits that the second strongest peak for ZnO located at 31.8^o is higher than the strongest peak of $Ta_2Zn_3O_8$ at 30.2^o. The opposite result is observed for ZnO(+ 50 wt.% Ta_2O_5)-SE where the strongest peak (30.2^o) for $Ta_2Zn_3O_8$ is higher than the second peak

(31.8^o) of ZnO (Fig. 4.3(c)). This suggests that the addition of Ta_2O_5 in greater mass ratio will consume a greater fraction of ZnO in the formation process of $Ta_2Zn_3O_8$ in ZnO(+ Ta_2O_5)-SE, leading to the decrease in H_2 sensitivity. In addition, from the full-width half maximum (FWHM) of the ZnO and $Ta_2Zn_3O_8$ peaks, it is inferred that the crystallinity of the resulting mixture is changing with increasing Ta_2O_5 addition. The FWHMs of both $Ta_2Zn_3O_8$ and ZnO peaks for ZnO(+ 50 wt.% Ta_2O_5)-SE are smaller than those of ZnO(+ 30 wt.% Ta_2O_5)-SE. This indicates that the increase in Ta_2O_5 addition from 30 to 50 wt.% creates a more crystalline electrode-material, which may also contribute to the changes in the catalytic activities against the reactions involving H_2. On the other hand, the decreased H_2 sensitivity at the Ta_2O_5 content of 70 wt.% is believed to be due to the different electrode composition ($ZnTa_2O_6$ and $Ta_2Zn_3O_8$) which

is confirmed via XRD measurement (Fig.4. 3).

4.3.2 Effect of sintering temperature of SE on H_2 sensing characteristics

The high H_2 sensitivity observed in the sensor using ZnO(+ 30 wt.% Ta_2O_5)-SE, was unfortunately confirmed to be followed by the high sensitivities toward HCs and CO. Since the electrode composition or the morphology has been proven to be one of the important factors in governing the sensing properties of the sensor, these factors were then engineered by increasing sintering temperature of the sensor in order to improve the sensitivity as well as selectivity toward H_2. The sensor using ZnO(+ 30 wt.% Ta_2O_5)-SE was sintered at temperature of 1000-1400^{o}C with interval of 100^{o}C for 2 h. The sintering at 1400^{o}C resulted in evaporation of SE material; hence the sensing characteristics could not be obtained. Figure 4.5 (a) and (b) show the cross-sensitivity comparison of the sensor using ZnO(+ 30 wt.% Ta_2O_5)-SE after sintering at 1000 and 1100^{o}C, respectively. There is a little difference in their gas sensitivity, while the selectivity trend remained almost same. Further increase in sintering temperature to 1200^{o}C caused some changes in both gas sensitivity and selectivity, where the sensor became relatively sensitive and selective toward NO_2 (Fig. 4.5(c)). The responses toward H_2 generated by the sensors sintered at 1100 and 1200^{o}C are almost same. A significant change was observed after sintering at 1300^{o}C; the sensor generated a high response toward H_2 (Δemf = - 480 mV) with negligible responses toward other gases examined (Fig.4. 5(d)) [5].

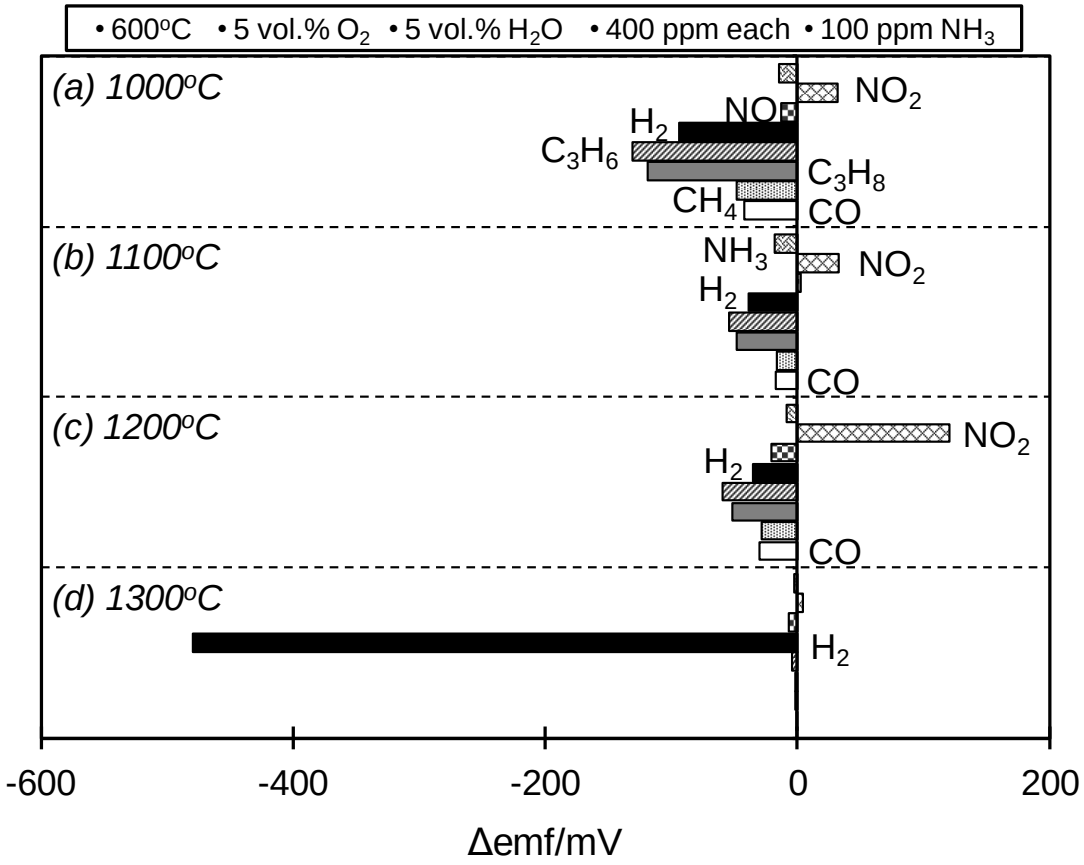

Figure 4.5 The cross sensitivity of the sensor utilizing ZnO(+ 30 wt.% Ta_2O_5)-SE after sintering at (a) 1000°C, (b) 1100°C, (c) 1200°C and (d) 1300°C for 2 h. (Reproduced from [5] Copyright 2012 and from [13] Copyright 2013 with permission from The Electrochemical Society)

Such a preferential H_2 sensing enhancement was further investigated by examining the crystal structure of the different SEs after sintering via XRD measurements (Fig.4. 6). As can be seen here, the sintering at 1000 and 1100°C was found to form a similar oxide-mixture composed of ZnO, $Ta_2Zn_3O_8$ and TaO_2 (Fig. 4.6 (a) and (b)). Further increase in the sintering temperature to 1200 and 1300°C brought about the formation of a mixture of ZnO and $Ta_2Zn_3O_8$ (Fig. 4.6 (c) and (d)). The effect of sintering temperature on the H_2 sensitivity and the SE composition is summarized in Table 4.1.

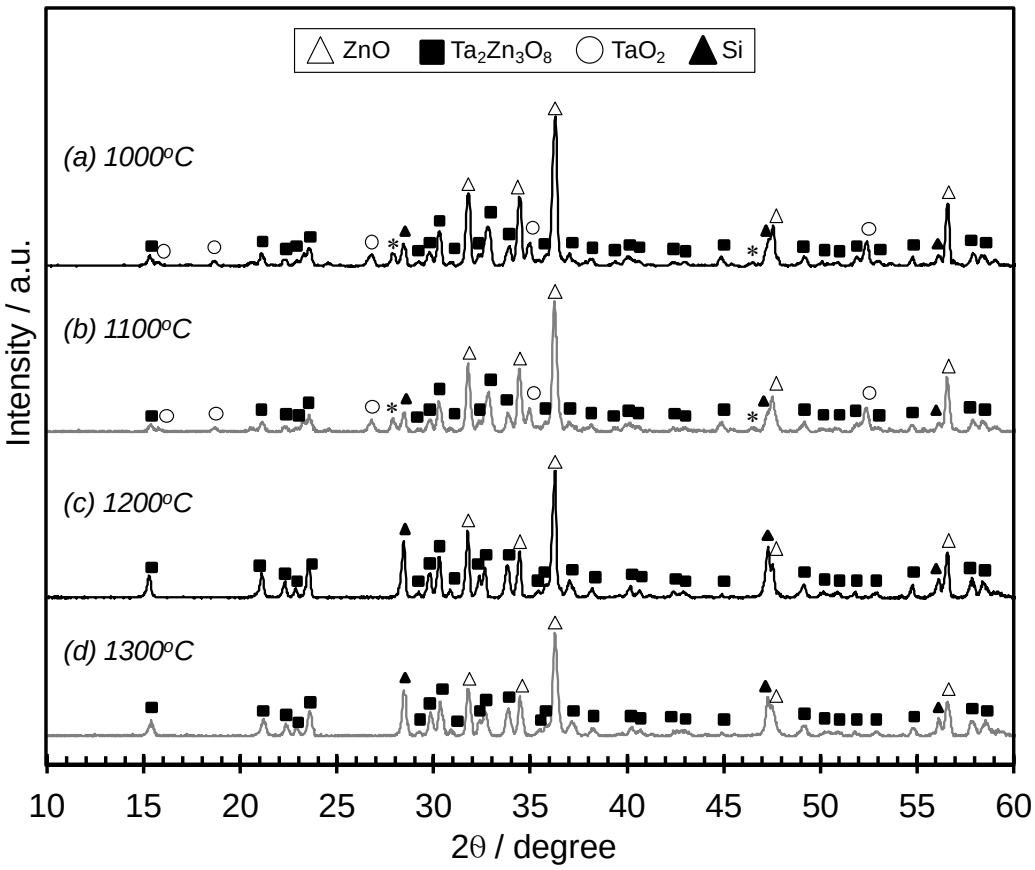

Figure 4.6 The XRD patterns of ZnO(+ 30 wt.% Ta_2O_5)-SE after sintering at (a) 1000°C, (b) 1100°C, (c) 1200°C and (d) 1300°C, for 2 h. (Reproduced from from [13] Copyright 2013 with permission from The Electrochemical Society)

Table 4.1 Effect of sintering temperature of ZnO(+ 30 wt.% Ta_2O_5)-SE on H_2 sensitivity (Δemf) and SE composition. (Reproduced [13] Copyright 2013 with permission from The Electrochemical Society)

Sintering temperature (°C)	1000	1100	1200	1300
H_2 sensitivity (mV)	-94	-40	-35	-480
Electrode composition	ZnO, TaO_2, $Ta_2Zn_3O_8$		ZnO, $Ta_2Zn_3O_8$	

It is noted that the significantly different H_2 sensitivities are observed in the sensors using each of SEs sintered at 1200 and 1300^oC, although the composition is same in the both cases. Then, the cause of such a considerably different sensing characteristic was elucidated by means of the polarization-curve measurements. The polarization curves for the cathodic reaction of O_2 and the anodic reaction of H_2 in the sensor using ZnO(+ 30 wt.% Ta_2O_5)-SE after sintering at 1200 and 1300^oC are given in Fig. 4.7. It is evident that the increase in the sintering temperature from 1200 to 1300^oC gives considerable decrease in the O_2 cathodic current (Fig. 4.7 (a)), while the H_2 anodic current is slightly changed (Fig. 4.7 (b)). The combination between such a significant decrease in the cathodic current and the slight increase in the anodic current shifted the mixed potential largely toward a more negative direction, bringing about the large increase in H_2 sensitivity. So far, the sensing mechanism of the sensor has been confirmed on the basis of the polarization curves measured [6-9]. The intersect point between the anodic and cathodic curves represents the mixed potential where the anodic and cathodic reactions proceed at the same rate. In the case of the present sensor, the estimated mixed-potential is found to be in good agreement with the sensor emf observed experimentally, as shown in Fig. 4.7 (c). This consistency suggests that the sensing mechanism of the present sensor is also based on a mixed-potential model [10-12].

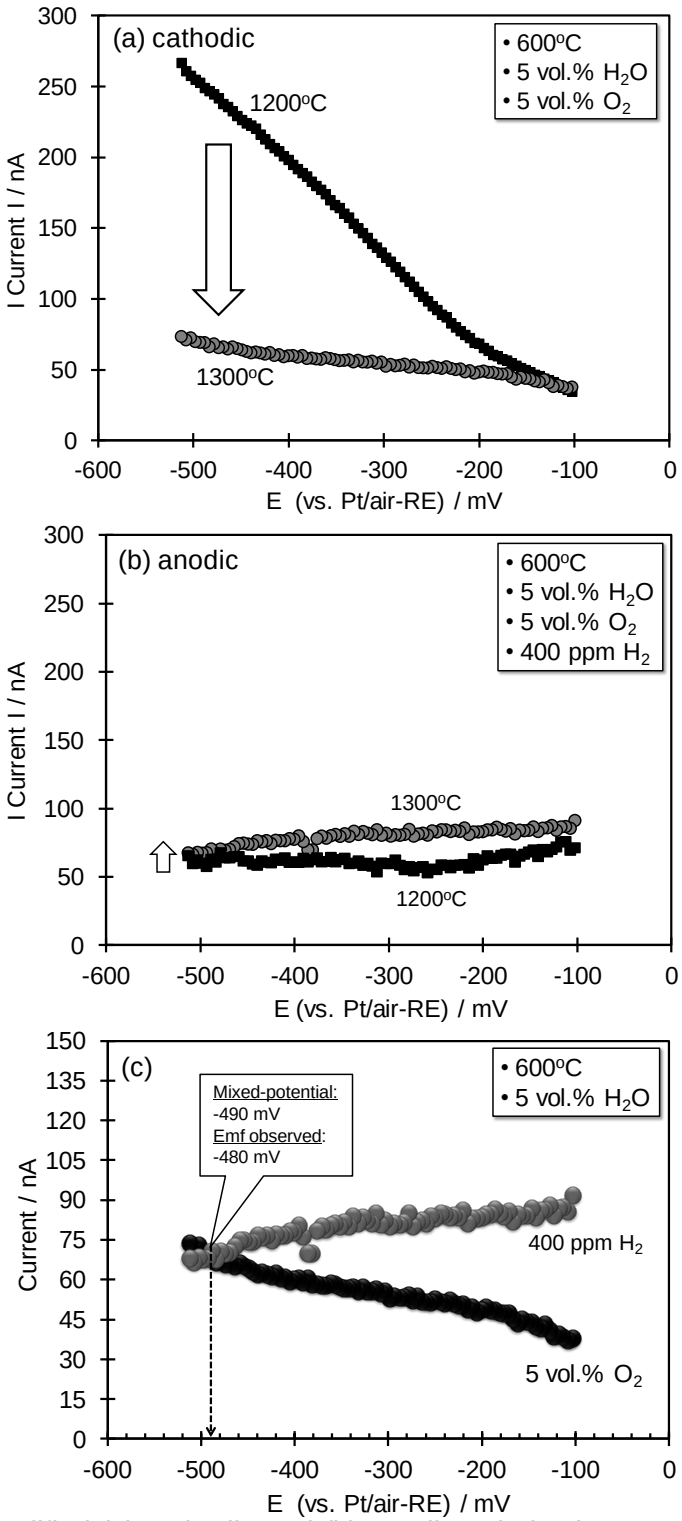

Figure 4.7 The modified (a) cathodic and (b) anodic polarization curves of the sensor using ZnO(+ 30 wt.% Ta_2O_5)-SE after sintering at 1200 and 1300°C for 2 h, and (c) the establishment of mixed-potential using the modified polarization curves for sensor utilizing ZnO(+ 30 wt.% Ta_2O_5)-SE sintered at 1300°C. (Reproduced from [13] Copyright 2013 with permission from The Electrochemical Society)

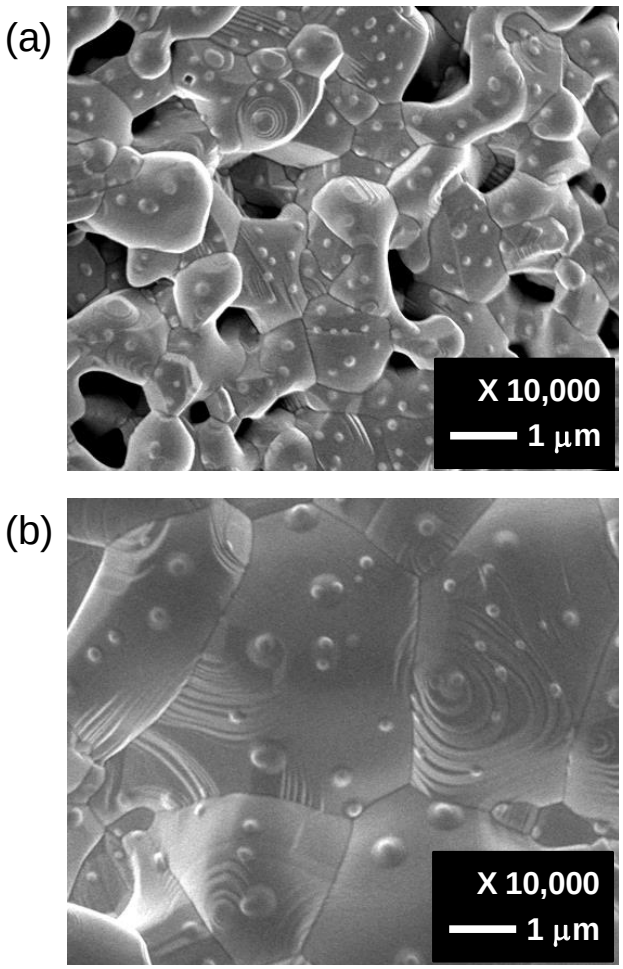

Figure 4.8 The SEM images of the surface morphology for ZnO(+ 30 wt.% Ta_2O_5)-SE after sintering at (a) 1200^oC and (b) 1300^oC, for 2 h. (Reproduced from [13] Copyright 2013 with permission from The Electrochemical Society)

The above-mentioned significant change in electrochemical catalytic activity, particularly toward O_2 reduction was further investigated by observing the morphology change after sintering. The SEM image given in Fig. 4.8(a) shows that SE after sintering at 1200^oC is composed of polygonal-shaped particles with the particle size of 400 nm - 2 μm and is relatively porous. On the other hand, when SE is sintered at 1300^oC (Fig. 4.8(b)), a denser (lower porosity) morphology consisting of larger polygonal particles (2-5 μm) was observed. Larger particles formed after sintering at 1300^oC will provide

an intrinsically smaller number of active site, by virtue of low ratio of surface area to volume, which can affect especially the cathodic reaction of oxygen, as seen in the polarization curves in Fig. 4.7 (a). Additionally, a denser (lower porosity) SE will result in a more tortuous path for large-sized gaseous molecules, except for the smallest-sized H_2 molecule. Thus, this may reduce the proportion of the larger-sized gaseous molecules capable of reaching and reacting at the SE/YSZ interface, after the gas-phase oxidation through the denser (lower porosity) SE layer.

4.3.3 Sensing characteristics of the sensor using ZnO(+ 30 wt.% Ta_2O_5)-SE sintered at 1300^oC.

Our research is focused on investigating the potential of the present material not only for H_2 detection under typical atmospheric conditions, but also for a sensor suitable for use in the wide range of oxygen concentration. Therefore, all initial measurements were conducted in 5 vol.% O_2 and humid conditions (5 vol.% H_2O). In order to investigate the sensing characteristics of the sensor using ZnO(+ 30 wt.% Ta_2O_5)-SE sintered at 1300^{o}C especially under a typical atmospheric condition, the sensor was then subjected to examine by using the different base gas (21 vol.% O_2 + 1.3 vol.% H_2O (32% RH at 30^{o}C) + N_2 balance). Figure 4.9 (a) shows the cross sensitivity toward different gases for the present sensor operated at 600^{o}C. It is clear that the sensor is relatively sensitive toward H_2 (Δemf $\approx$ -115 mV) with lower responses toward other gases (Δemf $\leq$ -20 mV). It should be noted that the selectivity trend when measured in 21 vol.% O_2 (Fig. 4.9 (a)) is similar to that examined in 5 vol.% O_2 (Fig. 4.5 (d)), while the sensitivity in 21 vol.% O_2 is lower than that in 5 vol.% O_2 [5].

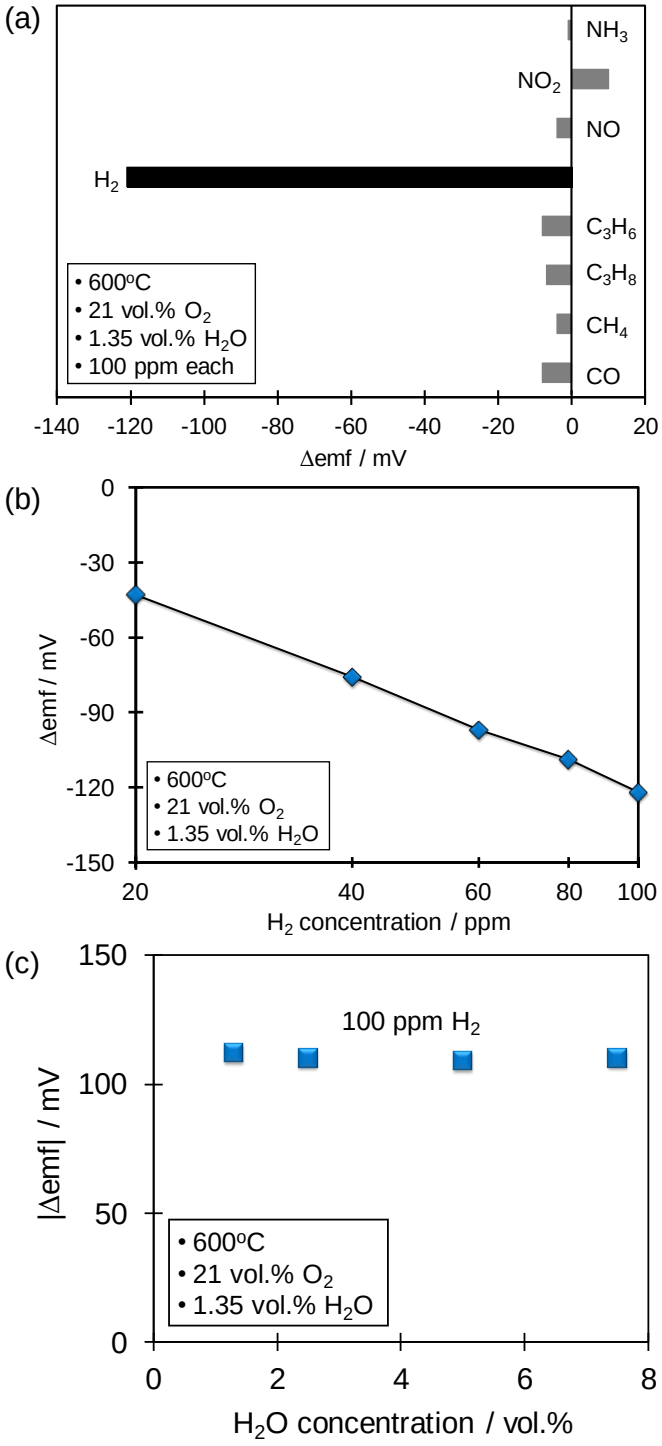

Figure 4.9 (a) The cross sensitivity, (b) the H_2 concentration dependence of Δemf and (c) the water-vapor concentration dependence of |Δemf|, for the sensor using ZnO(+ 30 wt.% Ta_2O_5)-SE operating at 600°C under humid conditions (21 vol.% O_2 + 1.3 vol.% H_2O + N_2 balance). ((a) and (b) reproduced from [5] Copyright 2012 and from [13] Copyright 2013, (c) is reproduced from [13], Copyright 2013, with permission from The Electrochemical Society)

Figure 4.9 (b) depicts the dependence of sensitivity on H_2 concentration for the present sensor in 21 vol.% O_2. A linear relationship between Δemf and H_2 concentration on a logarithmic scale is observed in the range of 20-100 ppm at 600^{o}C [5]. However, the response and the recovery are slow, which may be due to the low catalytic activities toward electrochemical reactions.

To further examine the ability of this sensor to function under fluctuated humidity, the sensor was tested under different water vapor concentrations. As shown in Fig. 9 (c), the H_2 sensitivity was only slightly affected by the change in water vapor concentration in the range of 1.3-7.5 vol.%. This suggests the robustness of the sensor against fluctuated conditions. The sensor was also subjected to the short-term stability test, where the sensitivity as well as selectivity was observed to be relatively stable during the 8-day operation examined. However, when this sensor using ZnO(+ 30 wt.% Ta_2O_5)-SE sintered at 1300^{o}C kept at 600^{o}C for long-term stability test, the H_2 sensitivity was decreased gradually over time (Fig. 4.10). This might limit the potential of the sensor using ZnO(+ 30 wt.% Ta_2O_5)-SE to be used in real applications.

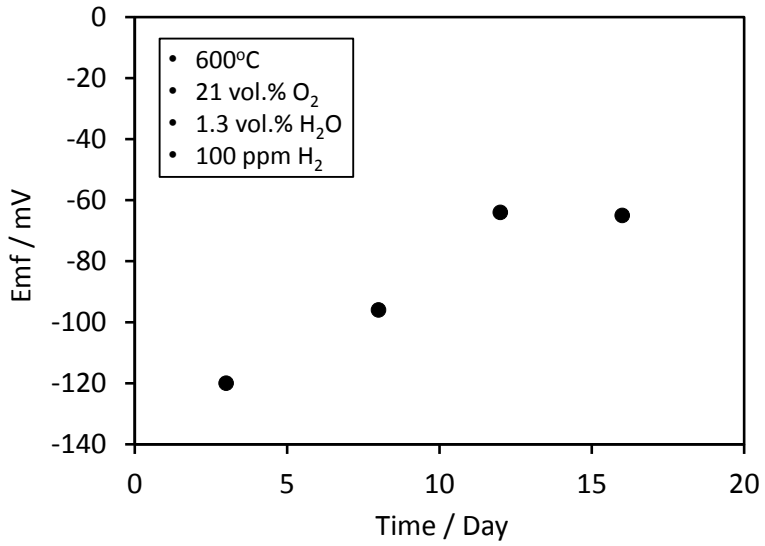

Figure 4.10 The short-term stability of the sensor using ZnO(+ 30 wt.% Ta_2O_5)-SE operating at 600^{o}C under humid conditions

4.4 Conclusions

A systematic investigation on the effect of Ta_2O_5 addition into ZnO-SE on the gas sensing performance was conducted. The addition of 30 wt% of Ta_2O_5 into ZnO has been proven to be effective in improving sensing properties of the YSZ-based sensor using each of the parental oxide-SEs. The addition of 30 wt.% Ta_2O_5 into ZnO-SE after sintering at 1000^oC was confirmed to form a mixture of ZnO, $Ta_2Zn_3O_8$ and TaO_2. This particular electrode composition with its corresponding morphology may be responsible for generating the highest response toward H_2 among the examined oxide mixtures. Furthermore, sintering of ZnO(+ 30 wt.% Ta_2O_5)-SE at 1300^oC was found to enhance the sensitivity and selectivity toward H_2. A drastic decrease in the O_2 cathodic current after sintering at 1300^oC may play a major role in augmenting H_2 sensitivity. Morphological observations via SEM revealed that a denser and tortuous morphology had formed after sintering at 1300^oC, which will drastically decrease the proportion of the large-sized gaseous molecules except for the smallest-sized H_2 molecule, being capable of reaching the interface of SE and YSZ, leading to the high sensitivity and selectivity to H_2. The good agreement between the estimated mixed-potential and the emf value observed experimentally suggests that the sensing mechanism of the present sensor is based on the mixed-potential model. Under typical atmospheric conditions, the sensor using ZnO(+ 30 wt.% Ta_2O_5)-SE sintered at 1300^oC is capable of generating sensitive and selective response toward H_2 and the H_2 sensitivity is hardly changed when examined at different water-vapor concentrations. In addition, both sensitivity and selectivity of the sensor were found to be relatively stable during the 8-day operation tested.

(Some of the contents in this chapter is reproduced from [5], Copyright 2012, and from [10], Copyright 2013, with permission from The Electrochemical Society)

References

[1] N. Miura, T. Raisen, G. Lu, N. Yamazoe, *Sensors and Actuators B: Chemical*, 47(1998) 84-91.

[2] L. Chevallier, E. Traversa, E. Di Bartolomeo, *Journal of The Electrochemical Society*, 157(2010) J386-J91.

[3] J. Zosel, G. Schiffel, F. Gerlach, K. Ahlborn, U. Sasum, V. Vashook, et al., *Solid State Ionics*, 177(2006) 2301-4.

[4] Y. Fujio, V.V. Plashnitsa, P. Elumalai, N. Miura, *Talanta*, 85(2011) 575-81.

[5] S.A. Anggraini, M. Breedon, N. Miura, *ECS Transactions*, 50(2013) 179-87.

[6] J.W. Fergus, *Sensors and Actuators B: Chemical*, 122(2007) 683-93.

[7] T. Hibino, A. Hashimoto, K.-t. Mori, M. Sano, *Electrochemical and Solid-State Letters*, 4(2001) H9-H11.

[8] N. Miura, G. Lu, N. *Solid State Ionics*, 136–137(2000) 533-42.

[9] A. Tomita, T. Yoshii, S. Teranishi, M. Nagao, T. Hibino, *Journal of Catalysis*, 247(2007) 137-44.

[10] M. Breedon, N. Miura, *Sensors and Actuators B: Chemical*, 182(2013) 40-4.

[11] T. Hibino, S. Wang, S. Kakimoto, M. Sano, *Sensors and Actuators B: Chemical*, 50(1998) 149-55.

[12] R. Mukundan, E.L. Brosha, D.R. Brown, F.H. Garzon, *Journal of The Electrochemical Society*, 147(2000) 1583-8.

[13] S. A. Anggraini, M. Breedon, N. Miura, *Journal of The Electrochemical Society*, 160 (9) (2013) B164-9

Chapter 5

H_2 Sensing Characteristic of the Sensor Utilizing $ZnTa_2O_6$-based Sensing Electrode

5.1 Introduction

The sensing characteristic of the sensor using $Zn_3Ta_2O_8$-based-SE has been discussed in chapter 4, where a sensitive and selective H_2 response was attained after sintering at high temperature. The incapability of the sensor to maintain a stable performance for a long-term operation has motivated the author to find another sensing electrode material that has a better endurance under a challenging atmosphere.

Despite the unsatisfactory stability exhibited by the sensor using $Zn_3Ta_2O_8$-based-SE, it has been found that another Zn-Ta-oxide-based-SE has showed a promising potential as a sensing electrode material to detect H_2 sensitively and selectively. Following this, the author then further explored another Zn-Ta-O compound, namely $ZnTa_2O_6$, as another prospective electrode material which is expected to possess a better performance as a sensing electrode material.

In this chapter, the investigation was also started by systematically examining the sensing characteristic of sensor using ZnO with different addition of Ta_2O_5. The morphology and the composition of the resulting SE materials, including the corresponding sensing performance of the developed YSZ-based sensor using each SE were investigated. Interestingly, unlike those developed sensors reported in chapter 3 and 4, where aging process has adverse effect on the sensitivity, the sensor using $ZnTa_2O_6$-based-SE received a positive effect from long-term aging. The sensing characteristic of the sensor using $ZnTa_2O_6$-based-SE after aging will be discussed in this

chapter.

5.2 Experimental

5.2.1 Sensor fabrication

The sensing device was fabricated by using a commercial hemispherically-terminated YSZ tube (8 mol.% Y_2O_3-doped ZrO_2, Nikkato, Japan). The physical dimensions of the tube were: 300 mm in length; 5 and 8 mm in inner and outer diameter, respectively. For stable sensing-performance of mixed-potential-type YSZ-based sensors, an additional YSZ layer between the SE and the YSZ solid electrolyte was recently proposed [1] The existence of such an intermediate YSZ layer has been reported to stabilize the sensing signal and improve the mechanical stability of SE [20]. Thus, an intermediate YSZ layer (*i*-YSZ) between the SE and the YSZ tube was also employed in this study. The YSZ powder (8 mol.% Y_2O_3-doped ZrO_2, Tosoh, Japan) was mixed with an organic binder (α-terpineol) and the resulting paste was applied onto the surface of the YSZ tube.

Following this, a commercial ZnO powder (Kojundo Chemical, Japan) was used as the base material for the ZnO-based SE. To fabricate the relevant ZnO:Ta_2O_5 mixture, Ta_2O_5 powder (Kojundo Chemical, Japan) was combined with ZnO powder and ground in a mortar. Then, α-terpineol was subsequently mixed with the powder, forming a uniform paste. The obtained paste was applied onto the surface of the *i*-YSZ layer to form a 4 mm-wide banded SE layer. Pt paste (Tanaka Kikinzoku, Japan) was applied on the inner surface of the YSZ tube, as the basis of the reference electrode (RE). The painted-YSZ tube was then dried at 130^{o}C, and subsequently sintered at 1200^{o}C for 2 h. Figure 5.1 is a representative cross-sectional SEM image of the sensor after sintering at 1200^{o}C. It can be seen here that the thickness of the SE layer was observed to be about

7 μm, while the thickness of the *i*-YSZ layer was approximately 3 μm.

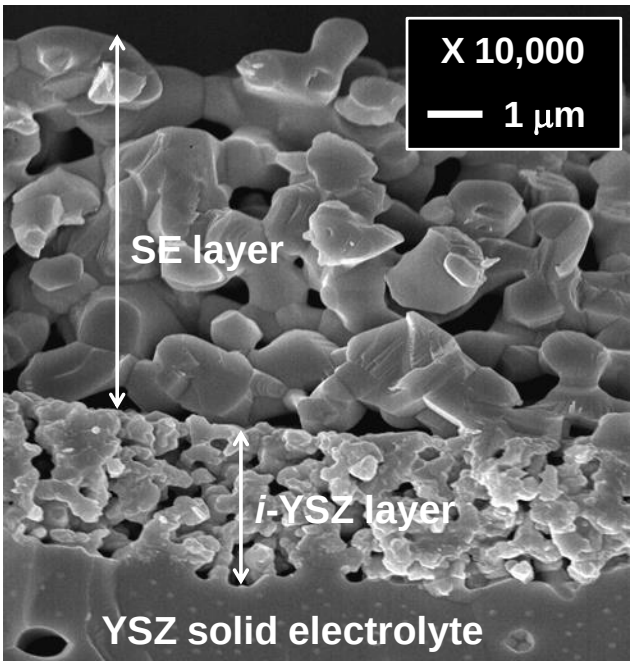

Figure 5.1 The representative cross-sectional SEM image of the sensing electrode after sintering at 1200°C for 2 h. (Reproduced from [3], Copyright 2013, with permission from Elsevier)

5.2.2 Sensing-performance evaluation

The fabricated tubular YSZ-based sensors were assembled in a custom quartz testing-cell in close proximity to the gas inlet, and connected to a conventional gas-testing system equipped with a high-temperature electric furnace and mass-flow controller system. The evaluation of gas-sensing characteristics was always performed at 500°C. The sensor was exposed alternately to the humidified base gas (5 or 21 vol.% O_2 + H_2O + N_2 balance) or the humidified sample gas containing H_2, CO, C_3H_8, C_3H_6, CH_4, NH_3, NO or NO_2, diluted with the base gas, in a constant gas flow-rate of 100 cm^3/min. The gas concentration of each sample gas was fixed at 100 ppm for cross sensitivity measurements. The concentration of water vapor was also fixed at 1.35 or 5

vol.%, except during the examination of the effect of water vapor on gas-sensing characteristics. The inner Pt electrode was always exposed to ambient atmospheric air, functioning as a Pt/air-RE, while the SE was exposed to sample gas or base gas. The difference in potential (*emf*) between the SE connected to the positive terminal of the electrometer and the Pt/air-RE connected to the negative terminal was measured as the sensing signal. The gas sensitivity (Δemf) was defined as the difference between the *emf* value in the base gas and that in the sample gas.

5.2.3 Morphology and crystal structure of SE

The morphology change of the SE materials after sintering at high temperature were observed by using a field-emission scanning electron microscope (FE-SEM, JSM-6340F, JEOL, Japan), operating at 5 kV. The crystal structure change of the SE was examined via an X-ray diffraction analysis (XRD, RINT 2100VLR/PC, Rigaku, Japan) with a Cu Kα X-ray source (λ = 1.5406 Å). To calibrate the XRD patterns, an internal standard of Si reference material (RSRP-43275G, Rigaku, Japan) was incorporated after sintering.

5.2.4Polarization curve measurements

The polarization (I-V) curve measurements were conducted by using an electrochemical analyzer (Autolab®, PGSTAT30, Eco-Chemie, Netherlands) with the potentiodynamic method at a constant scan rate of 8 mV/min in both of the base gas and the sample gas (H_2 diluted with base gas). The cathodic polarization curve was obtained by plotting the absolute current value against the applied potential. The modified polarization curve for the anodic reaction of H_2 was obtained by subtracting the current value in the base gas from the current value in the sample gas.

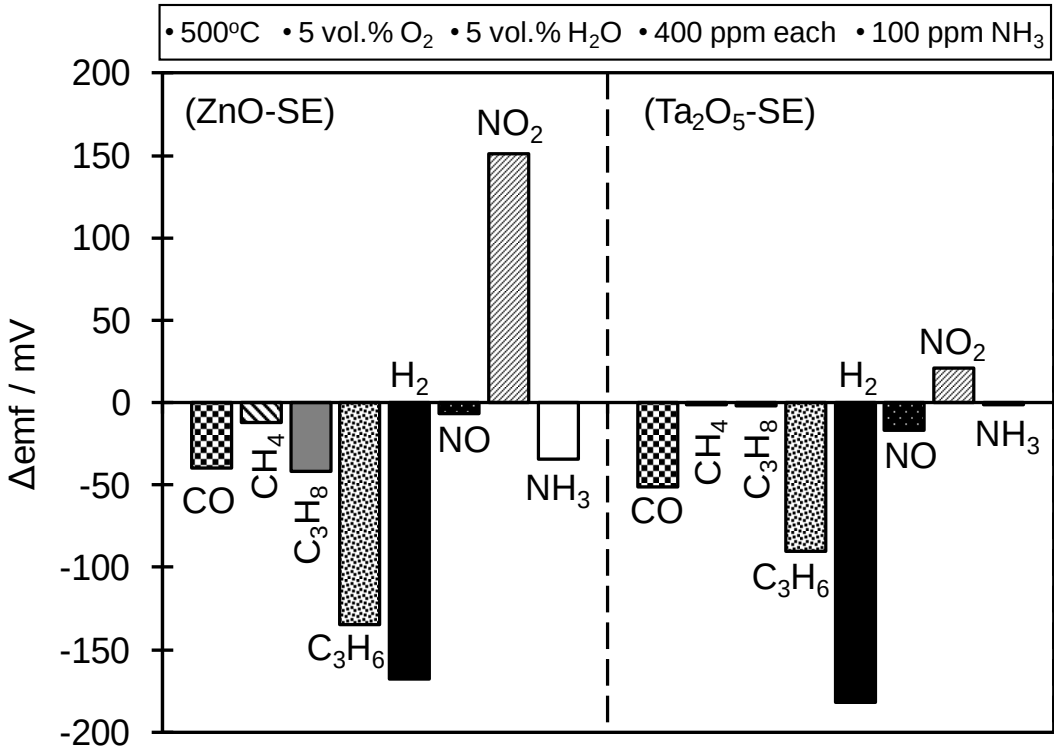

Figure 5.2 The cross sensitivity comparison of the sensor using (a) ZnO-SE and (b) Ta_2O_5-SE, at 500°C and under humid conditions. (Reproduced from [3], Copyright 2013, with permission from Elsevier)

5.3 Results and Discussion

5.3.1 Effect of Ta_2O_5 addition to ZnO on H_2 sensitivity

Preliminary investigations of the sensing characteristics of the ZnO- and Ta_2O_5-SE are presented in Fig. 5.2. The sensor using ZnO-SE could generate high responses toward H_2, CO, C_3H_6 and NO_2. Whilst, the sensor using Ta_2O_5-SE was found to be capable of generating high response toward H_2 followed by smaller responses toward CO and C_3H_6, with only minor responses toward other gases. Although the sensor using Ta_2O_5 as the SE seems to be capable of generating sensitive and selective response toward H_2, the utilization of Ta_2O_5 as a sensing electrode material has better SE mechanical stability. Therefore, the addition of Ta_2O_5 into ZnO is not only expected

to tune the sensitivity as well as selectivity of the sensor using ZnO-SE toward H_2, but also to improve the robustness of the sensor. Thus, Ta_2O_5 was added into ZnO with different composition, and the sensing characteristics toward H_2 were examined.

Figure 5.3 (a) shows the effect that Ta_2O_5 addition into ZnO has on H_2 sensitivity. When 30 wt.% Ta_2O_5 was added into ZnO, H_2 sensitivity decreased by approximately 75% from the recorded value of ZnO-SE at the same concentration (from -168 mV to -42 mV). The response toward H_2 was found to increase when Ta_2O_5 addition increased to 50 and 70 wt.%, where the sensor Δemf was observed to be -75 mV and -147 mV, respectively. The addition of 84 wt.% Ta_2O_5 was found to generate the highest response toward 400 ppm H_2 (Δ*emf*: approximately -251 mV), when compared with other SEs including the parent ZnO- and Ta_2O_5-SEs. However, a further addition of Ta_2O_5 to 95 wt.%, was found to reduce the sensitivity significantly from -250 mV to -70 mV. The detailed sensing characteristics for the sensor using ZnO(+ 84 wt.% Ta_2O_5)-SE toward different gases was examined, and presented in Fig. 5.4(b). It can be seen here that the sensor using this SE was also capable of generating sensitive, as well as a relatively selective response toward H_2.

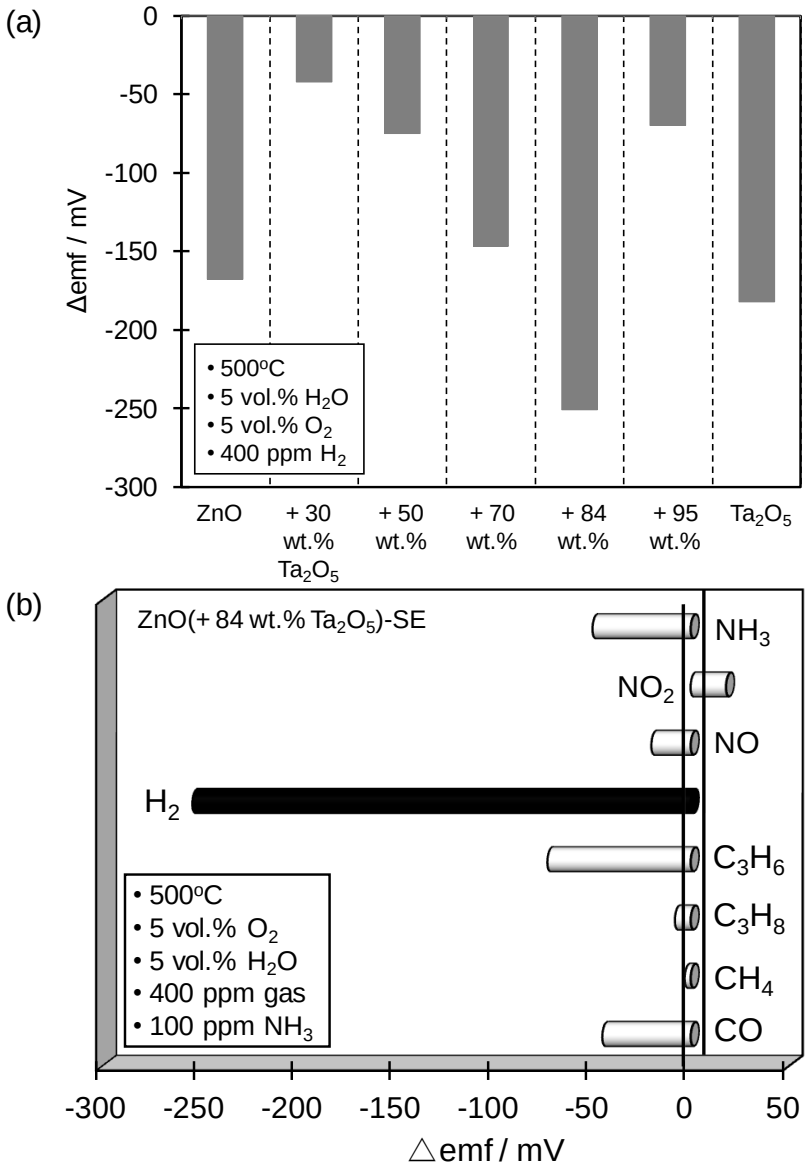

Figure 5.3 (a) Effect of Ta_2O_5 addition into ZnO on the H_2 sensitivity of the YSZ-based sensor operating at 500°C and under humid conditions, (b) The cross sensitivity of the sensor utilizing ZnO(+ 84 wt.% Ta_2O_5)-SE toward different gases. (Reproduced from [3], Copyright 2013, with permission from Elsevier)

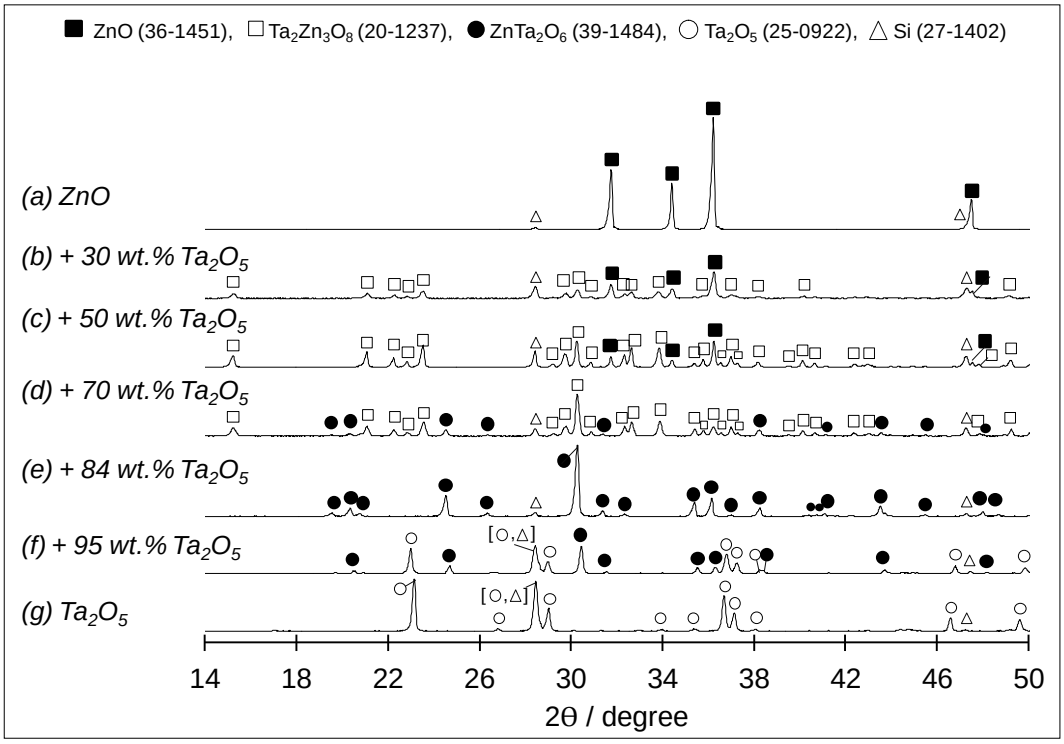

Figure 5.4 The XRD patterns for (a) ZnO with (b) + 30 wt.%, (c) + 50 wt.%, (d) + 70 wt.%, (e) + 84 wt.%, (f) + 95 wt.% Ta_2O_5 as well as (g) Ta_2O_5, after sintering at 1200°C. (Reproduced from [3], Copyright 2013, with permission from Elsevier)

5.3.2 Crystal structure and morphology of Zn-Ta-based oxide SE materials

The crystal structure of the ZnO-based SE materials with different additions of Ta_2O_5 was investigated with XRD. The corresponding XRD pattern of each SE material after sintering at 1200°C for 2 h, is given in Fig. 5.4, revealing that all of the observed peaks for the ZnO parental material were found to be in good agreement with the reference of ZnO (JCPDS no.: 36-1451). The addition of 30 and 50 wt.% Ta_2O_5 into ZnO generated a mixed composition, which was comprised of ZnO and $Ta_2Zn_3O_8$ (JCPDS no.: 20-1237) (Fig. 5.4 (b) and (c)). When the Ta_2O_5 content reached 70 wt.%, the observed XRD peaks for the resulting mixture corresponded well with the reference peaks for $ZnTa_2O_6$ (JCPSD no. 39-1484) and $Ta_2Zn_3O_8$ (Fig. 5.4 (d)). The characteristic reflections presented in Fig. 5.4(e) indicate that only the $ZnTa_2O_6$ phase was formed,

when 84 wt.% Ta_2O_5 was added into ZnO. A further addition of Ta_2O_5 up to 95 wt.% was confirmed to yield a mixture of $ZnTa_2O_6$, and Ta_2O_5 (JCPDS no.: 25-0922). Finally, the observed peaks in Fig. 5.4 (g) matched the reference peaks for Ta_2O_5.

It should be noted that some of the peaks for $ZnTa_2O_6$ and $Ta_2Zn_3O_8$ overlapped at the same 2θ angle in the + 84 wt.% Ta_2O_5 sample. As an example, at 32.3^o both $ZnTa_2O_6$ and $Ta_2Zn_3O_8$ would generate the highest intensity peak. However, given the phase diagram of this system [2] and the sintering temperature, it is unlikely that the $Ta_2Zn_3O_8$ phase will form at this particular composition. Furthermore, the intensity ratio of these peaks in the reference XRD pattern suggests that these peaks are in better agreement with those of $ZnTa_2O_6$.

The morphology changes of ZnO caused by the addition of Ta_2O_5 after sintering at 1200^oC are presented in Fig. 5.5. The SEM image shown in Fig. 5.5 (a) confirmed that pure ZnO had polygonal-shaped particles with hexagonally-stepped surfaces, with a particle size observed to be in the range of 1-3 μm. The addition of 30 wt.% Ta_2O_5 into ZnO was found to change the resultant particle shape from a stepped hexagonal motif, to smoother polygonal particles with size ranging from 300 nm to about 2 μm (Fig. 5.6 (b)). Some of these particles were observed to have a stepped morphology on their surface; however the number was greatly reduced when compared with the ZnO sample. Figure 5.6 (c) shows the morphology after the addition of 50 wt.% Ta_2O_5 into ZnO. Although the XRD analysis for ZnO with 30 and 50 wt.% Ta_2O_5 additions show similar XRD patterns, the morphology was found to be different. The ZnO(+ 50 wt.% Ta_2O_5) sample was also littered with smaller particles (size in the range of 100-200 nm) that were attached to the larger globular shaped particles (600 nm to 2 μm). The surface of these particles was rather smooth, with only a few stepped regions appearing on the surface of some of the particles. Increasing the addition to 70 wt.% Ta_2O_5 into ZnO

yields an even smoother morphology, as shown in Fig. 5.5 (d). As can be seen here, globular shaped particles were observed, with rather smooth surfaces, with an average particle size in the range of 500 nm to 2 μm. When 84 wt.% Ta_2O_5 was added into ZnO and sintered at 1200°C, the resulting sample was comprised of polygonal particles that had many stepped edges on its surface, compared with lower Ta_2O_5 wt.% additions. The average particle size was observed to be smaller than other additions, ranging from approximately 130 nm to 1.5 μm (Fig. 5.5 (e)). The addition of 95 wt.% Ta_2O_5 into ZnO

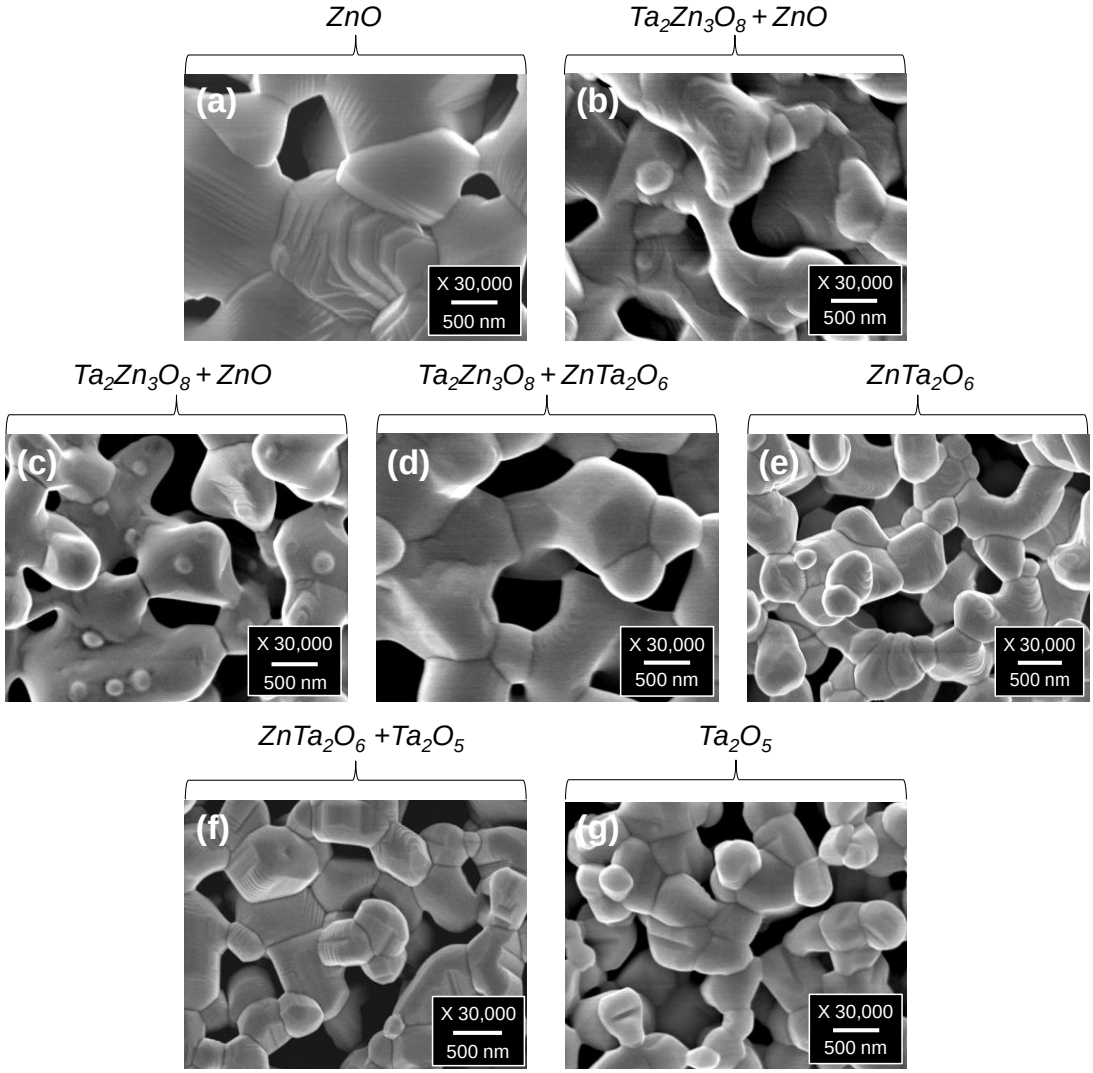

Figure 5.5 The representative SEM images of (a) ZnO with (b) 30 wt.%, (c) 50 wt.%, (d) 70 wt.%, (e) 84 wt.%, (f) 95 wt.% Ta_2O_5, additions; including the parent (g) Ta_2O_5-SE, after sintering at 1200°C. (Reproduced from [3], Copyright 2013, with permission from Elsevier)

was found to form polygonal particles with size ranging from approximately 250 nm to 1.2 μm. The surface of these particles was also observed to be predominantly smooth, with several stepped edges on the facetted regions of the particles (Fig. 5.5 (f)). For comparison, the surface of Ta_2O_5 after sintering at 1200^oC is presented in Fig. 5.5 (g). After calcination, Ta_2O_5 particles were polygonal-shaped with rather smooth surfaces and some steps present on the surface of the particles, with average sizes in the range of 250-900 nm in width.

The H_2 sensitivity (Fig. 5.2), as well as the XRD and SEM results of Figs. 5.4 and 5.5, suggests that the morphology and stoichiometry of the relevant SE material has an effect on H_2 sensing characteristics of each corresponding SE. The addition of 30 and 50 wt.% Ta_2O_5 into ZnO before sintering at 1200^oC resulted in the formation of a ZnO and $Ta_2Zn_3O_8$ composite electrode. The sensor using the composite (ZnO+$Ta_2Zn_3O_8$)-SE has lower H_2 sensitivity, when compared with the pure ZnO-SE. As can be seen in Fig. 5.5(b, c), an increase in Ta_2O_5 addition from 30 to 50 wt.% has improved the smoothness of the particles, with many of the stepped surfaces of the ZnO(+ 30 wt.% Ta_2O_5) (Fig. 5.6(b)) absent in the ZnO(+ 50 wt.% Ta_2O_5) sample. The nodular structures in Fig. 5.5(c) may also contribute to a reduction in the gas-phase catalytic activity of this composite. Further additions of 70 wt.% Ta_2O_5 yielded $Ta_2Zn_3O_8$ and $ZnTa_2O_6$, which can be used to fabricate an electrode with higher H_2 sensitivity. Neglecting the differences in the morphology, the formation of $ZnTa_2O_6$ appears to be a critical variable in influencing H_2 sensitivity. An increase of Ta_2O_5 into ZnO of approximately 84 wt.%, before sintering results in the formation of a pure $ZnTa_2O_6$ phase, which has the greatest H_2 sensitivity among the SE materials tested in this study. It is noteworthy that the ZnO(+ 70 wt.% Ta_2O_5) XRD patterns indicates that the majority of the SE material was $Ta_2Zn_3O_8$, due to the relative intensity differences between the reflections

of both phases. This is believed to be the reason why the ZnO(+ 70 wt.% Ta_2O_5)-SE has lower H_2 sensitivity than the ZnO(+ 84 wt.% Ta_2O_5-SE. When the Ta_2O_5 addition was increased up to 95 wt.%, the resulting mixture was observed to be comprised of $ZnTa_2O_6$ and Ta_2O_5. It is clear that the composition of the electrode material plays an important role in determining the H_2 sensitivity. However, it is also relevant to consider other contributing factors that are likely affecting H_2 sensitivity, such as the degree of crystallinity or particle size. The XRD pattern of the SE electrode materials were comprised of binary and ternary oxides, with the later having broadened peaks, when compared with the parent materials. This suggests that the degree of crystallinity may have decreased during the formation of these ternary compounds, which may be the result of an amorphous constituent contributing to the smoothness of the particles, observed in SEM in Fig. 5.5 (b), (c), (d) and (f). However, the relationship between the surface smoothness (and/or the degree of crystallinity) and the H_2 sensitivity, has yet to be clarified.

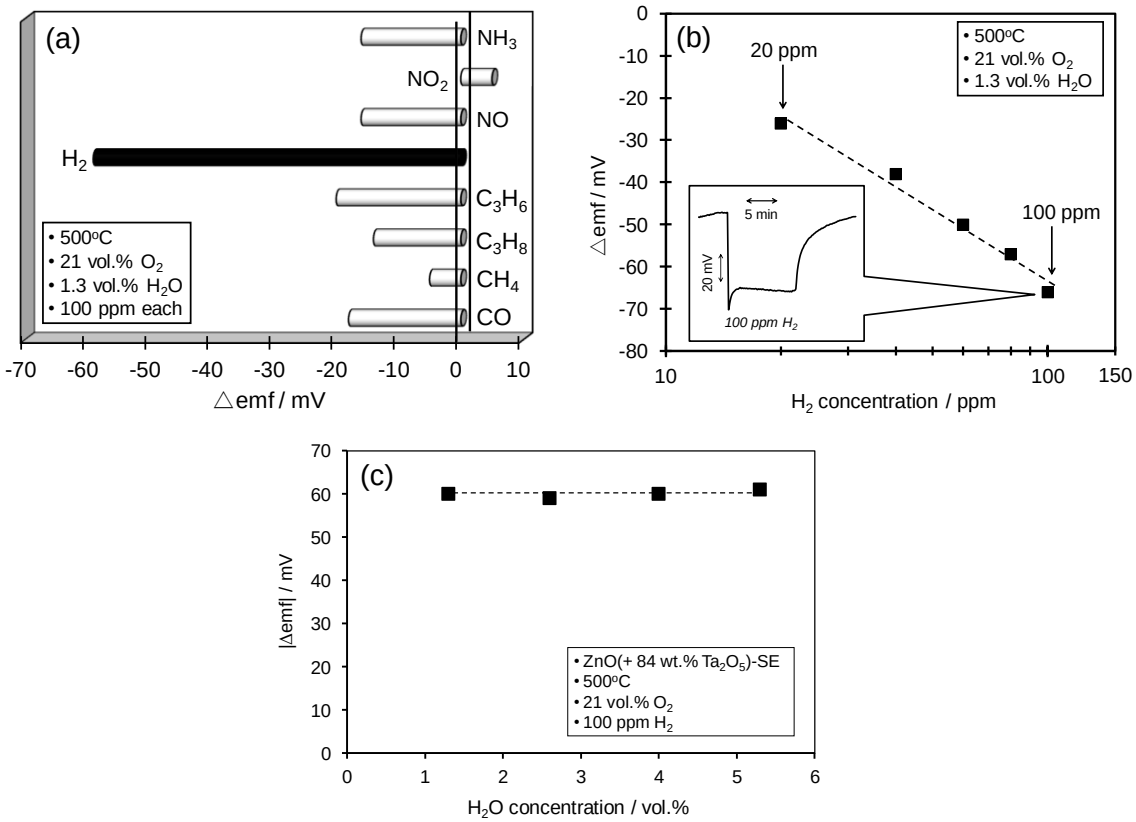

Figure 5.6 (a) The cross sensitivity and (b) the sensitivity dependency on H_2 concentration, for the sensor using ZnO(+ 84 wt.% Ta_2O_5)-SE at an operating temperature of 500°C under humid conditions. (Inset (b): Response transient to 100 ppm H_2). (c) The effect of humidity change on sensitivity (Δ*emf*) toward 100 ppm H_2 for the sensor using ZnO(+ 84 wt.% Ta_2O_5)-SE operating at 500°C under humid conditions. (Reproduced from [3], Copyright 2013, with permission from Elsevier)

5.3.3 The initial sensing characteristics of the sensor using ZnO(+ 84 wt.% Ta_2O_5)-SE

Previously, our research inquiries were concerned with the potential of this material not only for H_2 detection in typical atmospheric conditions, but also for wider exhaust gas detection applications. Therefore, all initial measurements were conducted in 5 vol.% O_2 and very humid conditions (5 vol.% H_2O). In order to investigate the sensing characteristics of the sensor using ZnO(+ 84 wt.% Ta_2O_5)-SE in realistic conditions, the sensor was then examined under the conditions approximating the atmospheric

conditions (21 vol.% O_2 and 1.3 vol.% H_2O, equivalent to 32% RH at 30^oC). The cross sensitivity of the sensor using $ZnTa_2O_6$-SE toward different gases is depicted in Fig. 5.6 (a). It can be clearly seen here that the sensor using $ZnTa_2O_6$-SE was relatively sensitive toward H_2 (Δemf ≈ -60 mV) with lower responses toward other gases (Δemf ≤ -20 mV). As can be seen here, the selectivity trend when measured in 21 vol.% O_2 was observed to be similar to that of examined in 5 vol.% O_2 (Fig. 5.3(b)). Figure 5.6(b) depicts the dependence of sensitivity on H_2 concentration for the present sensor. Good linearity between Δemf and H_2 concentration on a logarithmic scale in the range of 20-100 ppm was observed. The response transient to 100 ppm H_2 is given in the inset of Fig. 5.6 (b). The 90% response time was about 60 s, although the recovery was still slow. The improvement of sensing speed and the long-term stability of the present sensor are under investigation.

Since the humidity in the atmosphere fluctuates according to the weather, it is important for the sensor to work well under different humidity levels. In the light of this, the effect of water vapor concentration in the sample gas on the emf response for the sensor using $ZnTa_2O_6$-SE was assessed here and the result is given in Fig. 5.6 (c). It is apparent that the changes in water vapor concentration within the range of 1.3-5.3 vol.% hardly affects the sensitivity toward 100 ppm H_2. This indicates that the present sensor can endure the humidity change during operations, maintaining stable H_2 sensing characteristics.

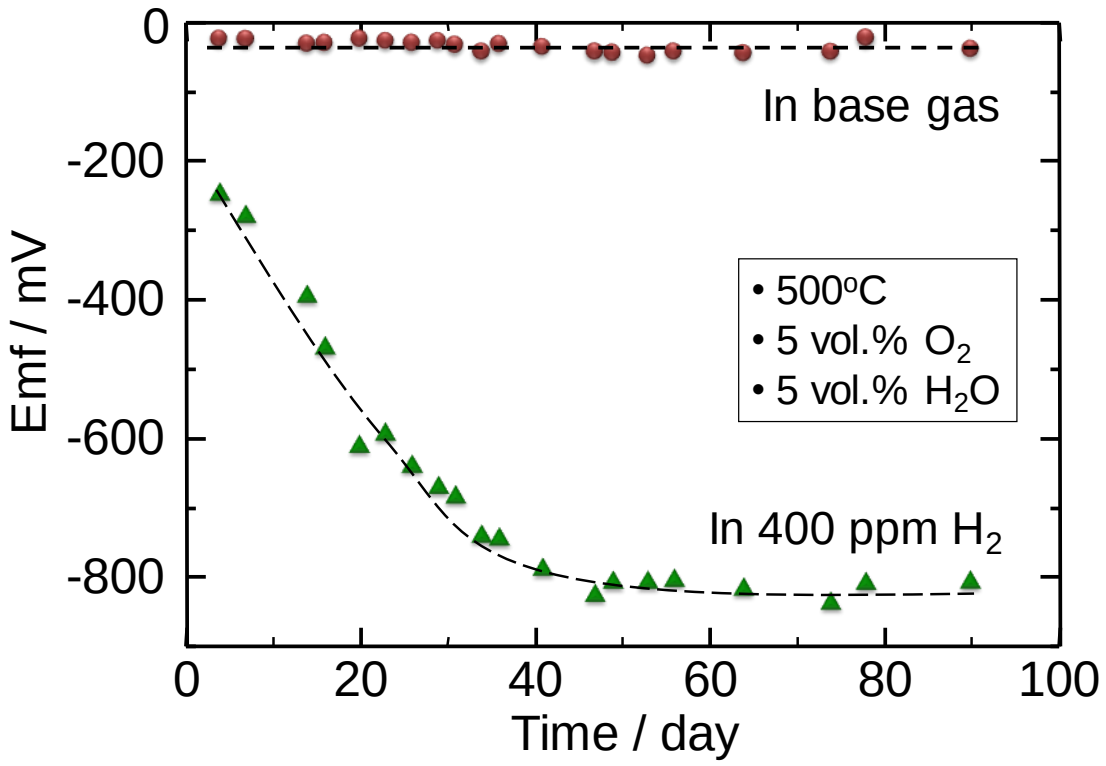

Figure 5.7 The change of emf value toward 400 ppm H_2 as well as the base line as a function of time for the sensor using ZnO(+ 84 wt.% Ta_2O_5)-SE. (Reproduced from [10], Copyright 2013, with permission from Elsevier)

5.3.4 Sensing characteristics of the sensor using ZnO(+ 84 wt.% Ta_2O_5)-SE after aging

The change in emf value to 400 ppm H_2 and to base gas is shown in Fig. 5.7 for the sensor using ZnO(+ 84 wt.% Ta_2O_5)-SE over the 90 days of operation (aging) at 500°C, where the emf value of the base gas was almost constant during the long-term operation. However, the H_2 sensitivity gradually increased with operation time and reached the plateau value of approximately -800 mV after 40 days of operation, and then it stabilized up to 90 days operation. All initial measurements were conducted in the gas containing 5 vol.% O_2 and 5 vol.% H_2O, in order to investigate the potential of the sensor to function at wide range of O_2 concentration [3].

Under typical atmospheric conditions, the stabilized sensor was still capable of

generating a sensitive response toward 100 ppm H_2 (Δemf $\approx$ -600 mV) with minor responses toward other examined gases (Δemf $< \pm$ 80 mV) (Fig. 5.8 (a)), with 90% response time to 100 ppm H_2 of approximately 70 s in humidified air. When the sensitivity (Δemf) was plotted against H_2 concentration, two different trends were observed. In the lower H_2 concentration range (10- 80 ppm), the sensitivity was linear with H_2 concentration on a linear scale (Fig. 5.8 (b)). Whilst in a higher H_2 concentration range (100-400 ppm), the sensitivity has a linear relationship with the H_2 concentration on a logarithmic scale (Fig. 5.8 (c)). The change in sensitivity for the entire examined range of H_2 concentration on a linear scale is shown in Fig. 5.8 (d).

The polarization curves given in Fig. 5.9 show that the generated anodic current of H_2 increased with increasing H_2 concentration. In the lower concentration range, the generated anodic current was found to be almost independent of the applied potential. This indicates that gas diffusion (mass transfer) across the SE layer is the rate-determining step. Since the absolute cathodic current of O_2 is almost proportional to the applied potential, according to the Butler-Volmer equation for low overpotential range, the sensitivity will be mathematically proportional with the gas concentration [4].

This manifests as the linear relationship between gas concentration and sensitivity (Fig. 5.9 (a)). In the higher concentration range, the generated anodic current was found to have a linear relationship with the applied potential which indicates that the rate determining step is most likely the electrochemical reactions occurring at the interface of SE/YSZ, following Tafel equation, where sensitivity will be proportional to the logarithm of gas concentration [5].

Polarization-curve measurements were also used to confirm the sensing mechanism of the developed sensor. The mixed potential obtained for each H_2 concentration was observed to be in relatively good agreement with the observed H_2 sensitivity (Table 5.1),

confirming that the sensing mechanism of the sensor is based on mixed-potential model [6-9].

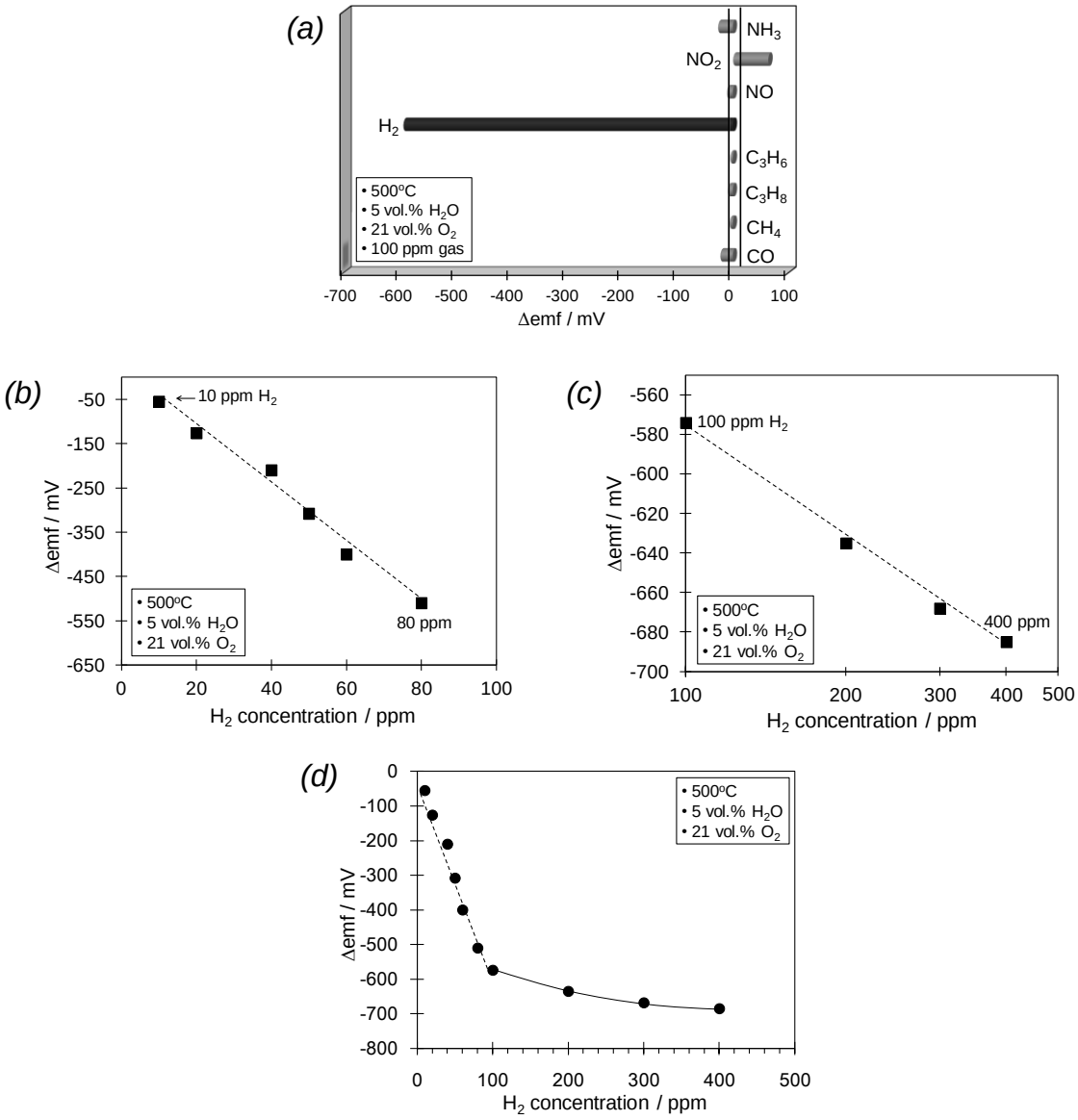

Figure 5.8 (a) The cross sensitivity to different gases and dependence of the sensitivity (Δemf) on H_2 concentration in (b) the lower concentration range (10-80 ppm), (c) the higher concentration range (100-400 ppm) and (d) the entire examined range of H_2 concentration, for the stabilized sensor utilizing ZnO(+ 84 wt.% Ta_2O_5)-SE. (Reproduced from [10], Copyright 2013, with permission from Elsevier)

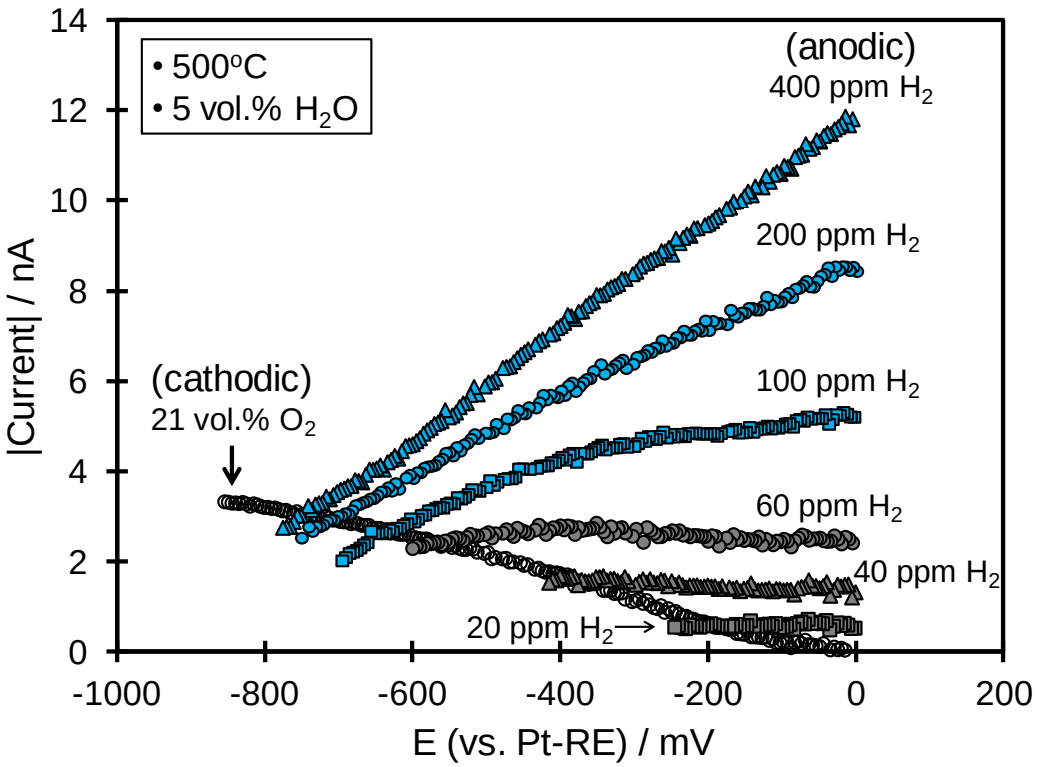

Figure 5.9 The modified polarization curves in 21 vol.% O_2 and in incrementally increasing H_2 concentration for the stabilized sensor using ZnO(+ 84 wt.% Ta_2O_5)-SE. (Reproduced from [10], Copyright 2013, with permission from Elsevier)

Table 5.1 The estimated mixed-potential and observed *emf* values toward different concentration of H_2 for the stabilized sensor utilizing ZnO(+ 84 wt.% Ta_2O_5)-SE. (Reproduced from [10], Copyright 2013, with permission from Elsevier)

H_2 conc. (ppm)	20	40	60	100	200	400
Emf obs. (mV)	-186	-386	-559	-653	-720	-771
Est. mixed potential (mV)	-196	-381	-561	-642	-716	-760

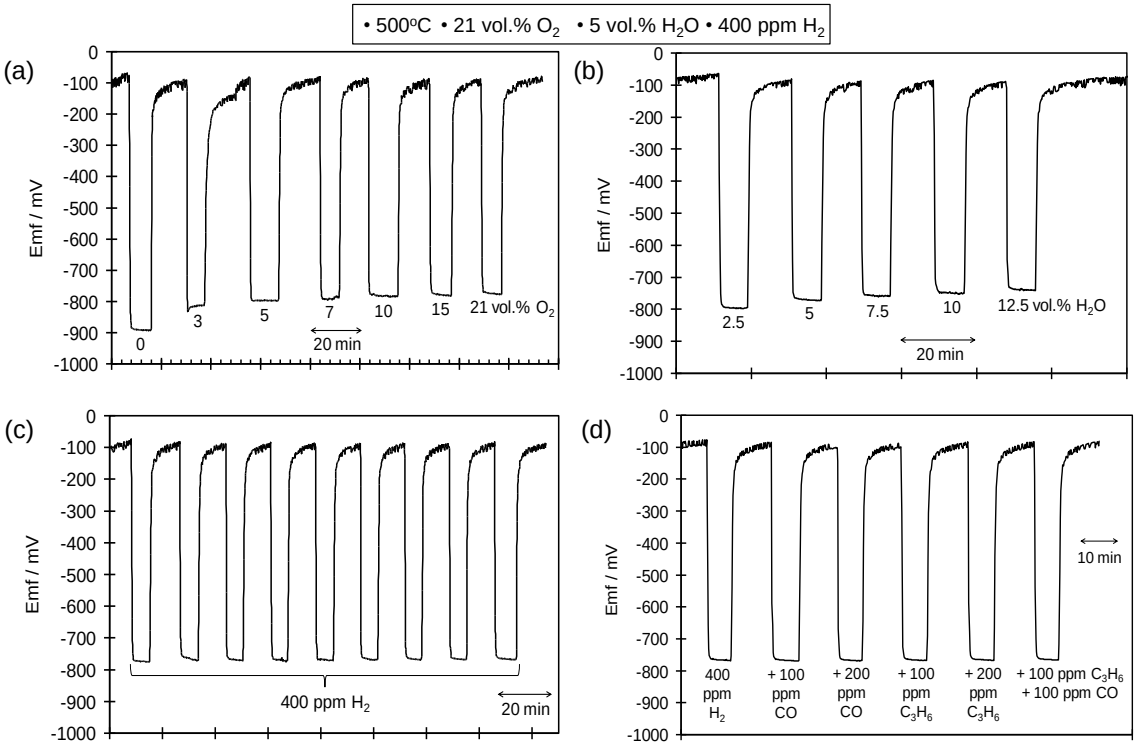

Table 5.10 Effect of changes in (a) O_2 and (b) H_2O concentration on the H_2 sensitivity, (c) the sensing signal repeatability to 400 ppm H_2 and (d) effect of interfering gases on the H_2 sensitivity, for the stabilized sensor using ZnO(+ 84 wt.% Ta_2O_5)-SE. (Reproduced from [10], Copyright 2013, with permission from Elsevier)

The ability of the sensor to function under fluctuating humidity and O_2 levels was examined to determine the wide-range operational parameters of the sensor. Figure 5.10 (a) depicts the response transient of 400 ppm H_2, which was only slightly affected by the change of O_2 concentration (3-21 vol.%). Similar behavior was observed over a wide range of water vapor concentrations (2.5-12.5 vol.%), where the H_2 sensitivity was largely unaffected by the change in water vapor (Fig. 5.10 (b)). This shows the robustness of the sensor to work in challenging conditions. In addition, the sensor was also capable of generating repeatable responses toward 400 ppm H_2 (Fig. 5.10 (c)). The effect of co-existing interfering gases (CO and C_3H_6) with H_2 was also investigated (Fig.

5.10 (d)), confirming that the response toward 400 ppm H_2 was stable, despite the co-existence of either CO or C_3H_6, even when the sensor was simultaneously exposed to a mixture of those three different gases.

5.4 Conclusions

A mixed-potential type YSZ-based sensor that capable of detecting H_2 sensitively and selectively has been developed, utilizing Zn-Ta-based oxides as the sensing electrode material. The addition of 84 wt.% Ta_2O_5 into ZnO-SE was found to generate the highest response toward H_2 when compared with other SEs with different mixture ratios. An 84 wt.% Ta_2O_5 addition into ZnO resulted in the formation of $ZnTa_2O_6$.

Initially, the sensor utilizing ZnO(+ 84 wt.% Ta_2O_5)-SE was relatively capable of detecting H_2 sensitively with lower responses toward unwanted interfering gases. The linear relationship between the sensitivity and gas concentration on a logarithmic scale indicated that the sensing mechanism is based on mixed-potential model. H_2 sensitivity increased and stabilized by the long-term aging for 90 days at 500^{o}C.

The H_2 sensitivity of the sensor using ZnO(+ 84 wt.% Ta_2O_5)-SE was gradually and drastically increased after long term aging, while maintaining minor response to other examined gases. Polarization-curve measurements for incrementally increasing concentrations of H_2 confirmed that the gas diffusion in the SE layer is the rate-determining step of the present sensor in the lower H_2 concentration range (10-80 ppm). While in the higher H_2 concentration range (100-400 ppm), the electrochemical reaction of H_2 (or O_2) occurring at the interface of SE/YSZ was identified as the rate-determining step. Good agreement between the estimated mixed-potential value and the obtained H_2 sensitivity suggests that the sensing mechanism of the sensor obeys the mixed-potential model. Owing to the excellent sensing performance, the developed

sensor can be considered as one of prospective candidates for the future H_2-leakage detection applications.

(Some of the contents in this chapter is reproduced from [3] and [10], Copyright 2013, with permission from Elsevier)

References

[1] Y. Fujio, V.V. Plashnitsa, P. Elumalai, N. Miura, *Talanta*, 85(2011) 575-81.

[2] J.L.W. R.S. Roth, W.S. Brower, *Journal of research of the National Bureau of Standards – Section A: Physics and Chemistry*, 74(1970).

[3] S.A. Anggraini, M. Breedon, N. Miura, *Sensors and Actuators B: Chemical*, 187(2013) 58-64.

[4] F.H. Garzon, R. Mukundan, E.L. Brosha, *Solid State Ionics*, 136–137(2000) 633-8.

[5] N. Miura, T. Raisen, G. Lu, N. Yamazoe, *Sensors and Actuators B: Chemical*, 47(1998) 84-91.

[6] S.A. Anggraini, V.V. Plashnitsa, P. Elumalai, M. Breedon, N. Miura, *Sensors and Actuators B: Chemical*, 160(2011) 1273-81.

[7] T. Hibino, A. Hashimoto, S. Kakimoto, M. Sano, *Journal of The Electrochemical Society*, 148(2001) H1-H5.

[8] X. Liang, S. Yang, J. Li, H. Zhang, Q. Diao, W. Zhao, et al., *Sensors and Actuators B: Chemical*, 158(2011) 1-8.

[9] A. Tomita, Y. Namekata, M. Nagao, T. Hibino, *Journal of The Electrochemical Society*, 154(2007) J172-J6.

[10] S.A. Anggraini, M. Breedon, N. Miura, *Electrochemistry Communications*, 31 (2013) 133-6

Chapter 6

Insight into Aging Effect on Enhancement of H_2 Sensing Characteristic of the Sensor Utilizing $ZnTa_2O_6$-based Sensing Electrode

6.1 Introduction

The previous chapter has elaborated detail investigation which was started by systematically examining the sensing characteristic of sensor using ZnO with different addition of Ta_2O_5. The addition of 84 wt.% Ta_2O_5 into ZnO has been confirmed to form a new phase of $ZnTa_2O_6$. The sensor using this particular compound was observed to exhibits a sensitive and relatively selective response toward H_2 [1] After the 40-day aging at 500^{o}C, the sensitivity of the sensor using $ZnTa_2O_6$-based-SE toward 400 ppm H_2 had peaked, and stabilized at around -800 mV [2]. Interestingly, this significant enhancement in H_2 sensitivity after the long-term aging was not accompanied by an increase in sensitivity toward the other examined gases such as CO and C_3H_6. Thus, the extremely high H_2 selectivity was achieved after the aging. [2]

In this chapter, the effect of aging in enhancing the H_2 sensing characteristic of the sensor utilizing ZnO(+ 84 wt.% Ta_2O_5)-SE will be elucidated in detail. Specifically, we examined the changes in morphology, crystal structure and chemical surface state of the SE material after the aging, including the corresponding changes in the catalytic activities. More importantly, the cause for such a highly sensitive and selective H_2 response will be discussed here. Aging process itself is a challenge that is often faced in sensor development and sometimes plays a role in changing the sensing properties of an electrode material. Therefore, an insight into how and why an aging process affects the sensing properties of an electrode material is very useful and particularly important for

those who are working in the field of gas sensor research.

6.2. Experimental

6.2.1 Sensor fabrication

First, an intermediate YSZ layer (abbreviated as *i*-YSZ) between the SE layer and a YSZ tube (8 mol.% Y_2O_3-doped ZrO_2, Nikkato, Japan) was formed; a YSZ powder (8 mol.% Y_2O_3-doped ZrO_2, Tosoh, Japan) was mixed with α-terpineol and the resulting paste was applied onto the surface of the YSZ tube. The utilization of such an additional YSZ layer between SE and a YSZ tube has been reported to facilitate the sensing-signal stabilization and to improve the mechanical stability of the SE/YSZ interface [3]. The physical dimensions of the hemi-spherically terminated tube utilized here were 300 mm in length, 5 and 8 mm in inner and outer diameter, respectively.

The SE paste was prepared by grinding a powdered ZnO (16 wt.%) (99.99%, Kojundo Chemical, Japan) together with a powdered Ta_2O_5 (84 wt.%) (99.99%, Kojundo Chemical, Japan) in a mortar, and then an organic binder (α-terpineol) was added to the powder mixture. The obtained paste was applied onto the surface of *i*-YSZ to form a 4 mm-wide banded SE layer. A Pt paste (Tanaka Kikinzoku, Japan) was applied on the inner-end surface of the YSZ tube, forming as the reference electrode (RE). The painted whole YSZ-tube was then dried at 130^{o}C and subsequently sintered at 1200^{o}C for 2 h in an air atmosphere.

6.2.2 Sensing-performance evaluation

The fabricated tubular YSZ-based sensors were assembled in a custom-made quartz testing-cell in close proximity to a gas inlet, and connected to a conventional gas-testing system equipped with a high-temperature electric furnace and a mass-flow

controller system, as reported elsewhere [1, 4]. The evaluation of gas-sensing characteristics was performed at a constant operating temperature of 500^{o}C. The sensor was alternately exposed to the humidified base-gas, (21 vol.% O_2 + 1.3 vol.% H_2O + N_2 balance) or the humidified sample-gas containing H_2, CO, C_3H_8, C_3H_6, CH_4, NH_3, NO or NO_2, diluted in the base gas with a total gas flow-rate of 100 cm^3/min. The gas concentration of each sample gas was fixed at 100 ppm for cross-sensitivity measurements. The inner Pt electrode was always exposed to an ambient air, functioning as a Pt/air-RE, while SE was exposed to the sample gas or the base gas. The difference in potential (electromotive force (*emf*)) between SE connected to the positive terminal of an electrometer (R8240, Advantest, Japan) and Pt/air-RE connected to the negative terminal was measured as a sensing signal. The gas sensitivity (Δemf) was defined as the difference between the *emf* value in the base gas and that in the sample gas.

6.2.3 Polarization curve measurements

The measurements of current-voltage (polarization) curves were conducted by means of an electrochemical analyzer (Autolab®, PGSTAT30, Eco-Chemie, Netherlands), based on a potentiodynamic method (at a constant scan rate of 8 mV/min), by using two electrode configurations in each of the base gas and the sample gases (diluted with synthetic air or N_2). The modified cathodic polarization curve was obtained by plotting the absolute current value (measured in the base gas) against the applied potential. The modified polarization curves for the anodic reactions of each of sample gases (H_2, C_3H_6 and CO, diluted with air) were obtained by subtracting the current value measured in the base gas from that in each sample gas (diluted with air). In the case of the anodic polarization curve measured in each of sample gases (H_2, C_3H_6

and CO, diluted with N_2), the obtained anodic current value was plotted directly against the applied potential.

6.2.4 XRD, SEM and XPS measurements

The crystal structure change of the SE material before and after the aging at 500^{o}C for 80 days was examined via an X-ray diffraction analysis system (XRD, RINT 2100VLR/PC, Rigaku, Japan), with a Cu Kα X-ray source (λ = 1.5406 Å). To calibrate XRD patterns, an internal Si reference powder (RSRP-43275G, Rigaku, Japan) was incorporated into the powder samples. The morphological change in the SE material before and after the long-term aging was also observed by means of a field-emission scanning electron microscope (FE-SEM, JSM-6340F, JEOL, Japan), operating at 5 kV. An X-ray photoelectron spectroscopy system (XPS, AXIS-165, Shimadzu/Kratos, Japan) was also utilized for examination of chemical surface state of the SE material before and after the aging, by the use of a monochromatic Al Kα source for excitation (12 kV and 2 mA) under ultra-high vacuum (1.18 x 10^{-6} Pa).

6.2.5 Evaluation of gas-phase catalytic activity

The examination regarding the gas-phase catalytic activity of the SE material was conducted by using a cell arrangement similar to that reported elsewhere [5]. The SE-material powder (50 mg) was packed into a quartz tube which was positioned inside a separate catalyst cell. This catalyst cell was located at the upstream of the sensing cell. The temperature inside the catalyst cell was maintained at the same temperature as that inside the sensing cell. The calibrated YSZ-based sensor using ZnO(+ 84 wt.% Ta_2O_5)-SE was used to monitor the change in H_2 concentration in the outlet gas from the catalyst cell, while an automotive emission analyzer, (MEXA102G, Horiba, Japan) was

utilized to monitor the change in C_3H_6 concentration in the outlet gas.

All measurements stated in Sections 2.4 and 2.5 were carried out by using ZnO(+ 84 wt.% Ta_2O_5) as a powder sample rather than the fabricated electrode itself, due to the incompatibility of the electrode for these measurements. Since the powder samples were fabricated and treated (aged) in a same manner as the SE was done, they could be used as a substitute for the SE sample. Thus, we believe that the results obtained from either of the powder sample or the SE will not result in a significant difference.

6.3. Results and Discussion

6.3.1 Effect of aging on electrode composition and morphology

Initially, the sensor using ZnO(+ 84 wt.% Ta_2O_5)-SE showed relatively sensitive and selective H_2 response, as depicted in Fig. 6.1(a). The H_2 sensitivity was gradually increased and stabilized after the aging for more than about 40 days [2]. As shown in Fig. 6.1(b), not only did the sensor become highly sensitive toward H_2, but also extremely selective to H_2 after the long-term aging (for 80 days in this case). This significant change in H_2 sensitivity after the long-term aging was studied here by investigating the change in crystal structure via XRD measurements and that in morphology via SEM observations.

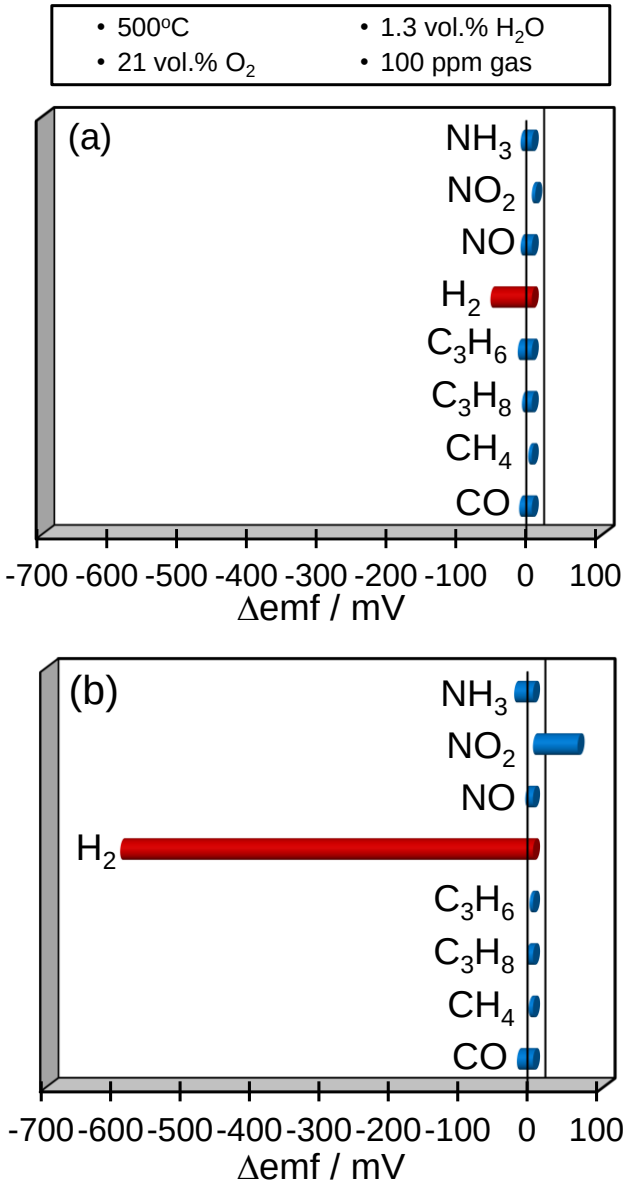

Figure 6.1 Cross sensitivity of the sensor using ZnO(+ 84 wt.% Ta_2O_5)-SE; (a) initial state and (b) stabilized state (after the aging at 500°C for 80 days) under humid conditions (1.3 vol.% H_2O). [Figure 6.1(a) reprinted from [21] and Fig. 6.1(b) reprinted from [22], with permission from Elsevier]

The comparison of XRD patterns of the ZnO(+ 84 wt.% Ta_2O_5) powder samples presented in Fig. 6.2 shows a negligible change in the crystal structure of the initial-state (before aging) sample (Fig. 6.2(a)) and that of the sample aged at 500°C for 80 days (Fig. 6.2(b)). All the XRD peaks in both samples were found to be in good

agreement with those for $ZnTa_2O_6$ (JCPDS no. 39-1484). As can be seen from the respective insets in Fig. 2, there is a subtle refinement in the peak shape to that of singular reflection after the aging, if (131) peaks compared before and after the aging. This imply the presence of small amount of another compound other than $ZnTa_2O_6$ at the bulk of the initial SE material

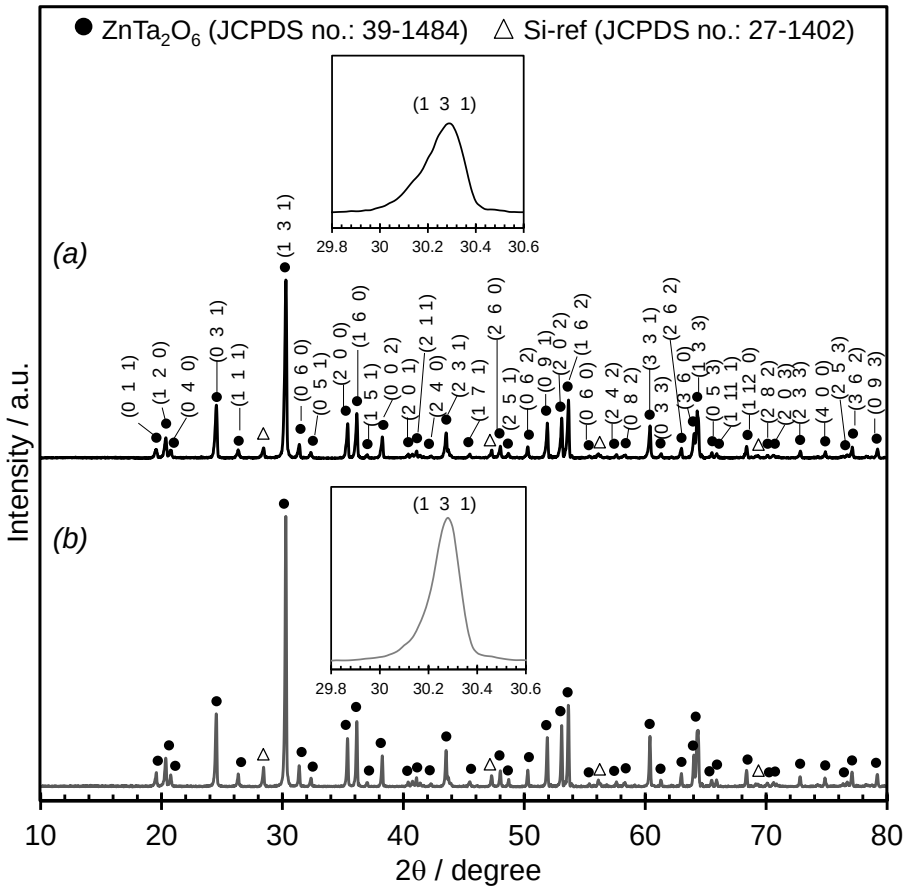

Figure 6.2 XRD patterns of the ZnO(+ 84 wt.% Ta_2O_5) powder sample; (a) initial state and (b) after the aging at 500°C for 80 days. (Insets show (1 3 1) peak before and after aging). (Reproduced from [24], Copyright 2013, with permission from the American Chemical Society).

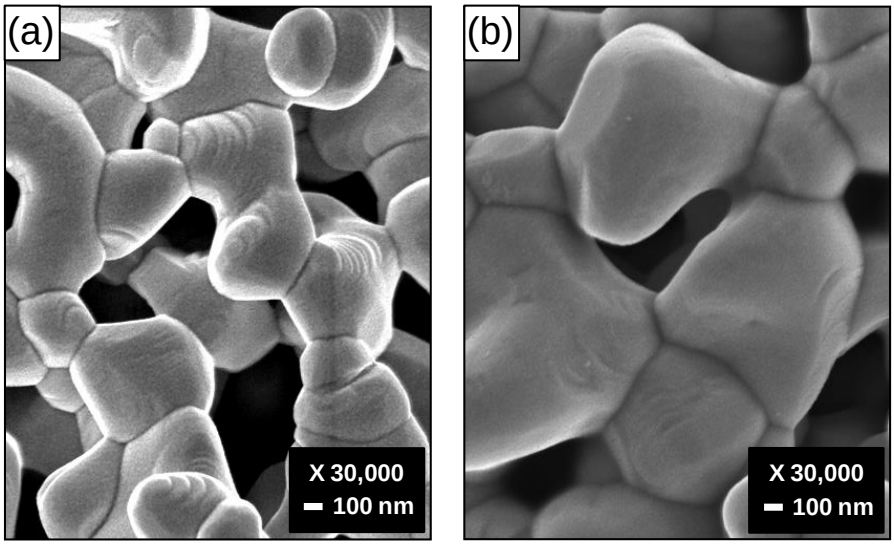

Figure 6.3 SEM images of the ZnO(+ 84 wt.% Ta_2O_5) sample (a) initial state and (b) after the aging at 500^oC for 80 days. (Reproduced from [24], Copyright 2013, with permission from the American Chemical Society).

The morphological change of the SE material due to the aging was observed by means of SEM and the results were presented in Fig. 6.3. It is seen that the morphology of the ZnO(+ 84 wt.% Ta_2O_5) powder sample just after sintering at 1200^oC for 2 h, consists of polygonal-shaped particles with some stepped regions that appear on the surface of several particles (Fig. 6.3 (a)). The particle size is in the range of 200 nm - 1.2 μm. Figure 6.3(b) shows the SEM image of the ZnO(+ 84 wt.% Ta_2O_5)-SE sample after aging at 500^oC for 80 days. The particles enlarge and agglomerate after the aging, with the particle size ranging from 500 nm to 1.4 μm. Additionally, the aging process also decreases the porosity of the SE material. A relatively denser morphology will naturally give a more tortuous diffusion path. Such a situation may be more favorable for smaller molecular-sized gas such as H_2, to pass through the path, compared with larger molecular-sized gases. This may be one of the factors that result in a significant improvement of H_2 selectivity after the long-term aging of the sensor.

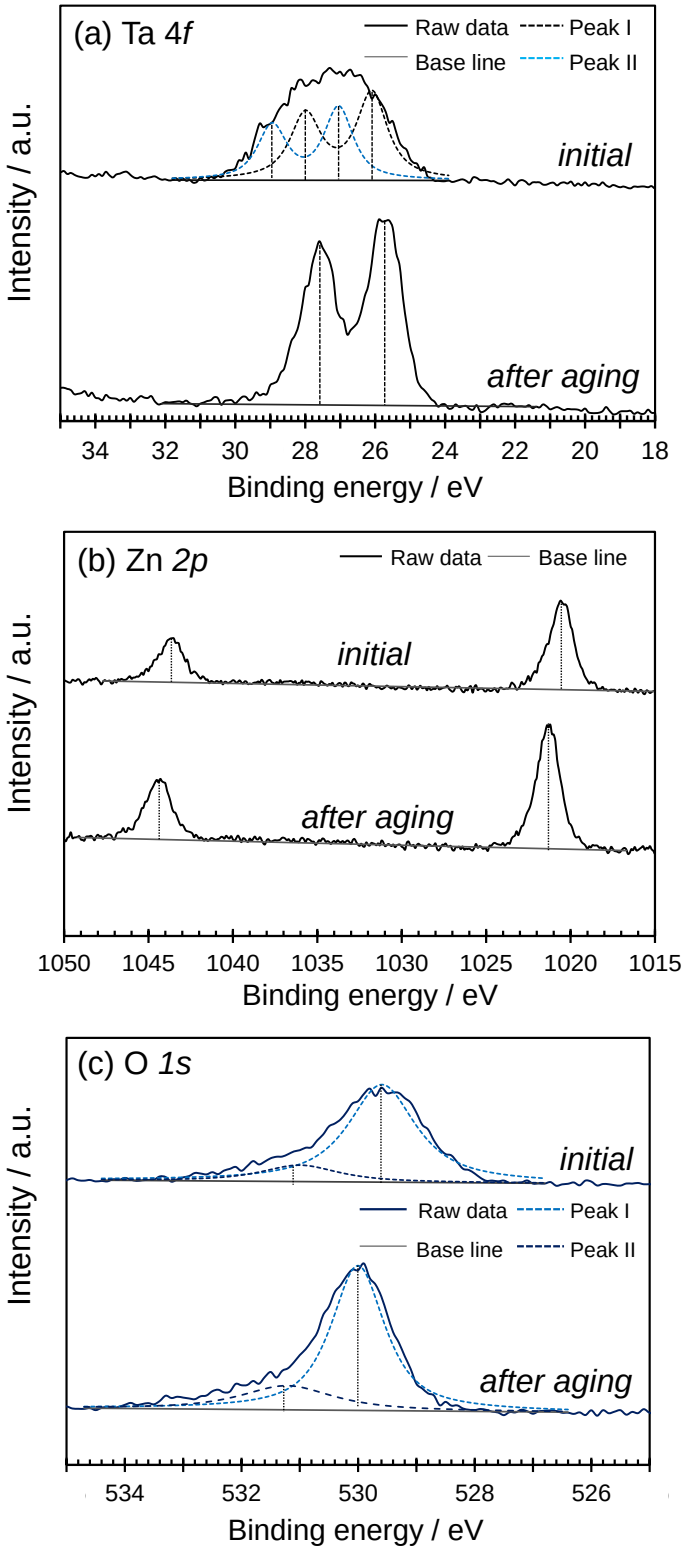

Figure 6.4 XPS spectra for (a) Ta *4f*, (b) Zn *2p* and (c) O *1s* of the ZnO(+ 84 wt.% Ta_2O_5) powder samples at initial state and after the aging for 80 days. (Reproduced from [24], Copyright 2013, with permission from the American Chemical Society).

6.3.2 Effect of aging on chemical surface state of SE

A detailed study regarding the change in the chemical surface state of the SE materials before and after the aging was performed via XPS measurements. The resulting spectra were treated by using a linear background and fitted with Lorentzian-Gaussian function. Figure 6.4 shows the comparison of XPS spectra of Ta 4*f*, Zn 2*p*, O 1*s* for the ZnO(+ 84 wt.% Ta_2O_5) powder samples before and after the aging for 80 days. The Ta 4*f* spectra of the initial-state sample show a broad peak which can be deconvoluted and fitted into two doublets (Fig. 6.4(a) and Table 6.1). The first pair of peaks is centered at ($4f_{7/2}$) 26.1 eV and ($4f_{5/2}$) 28.0 eV, with a spin orbital splitting 1.9 eV. The second set of peaks was found to consist of components that located at ($4f_{7/2}$) 27.0 eV and ($4f_{5/2}$) 28.9 eV, with an identical spin orbital splitting of 1.9 eV. The observed binding-energy values are within the range of those reported for the oxidation (valence) state (+5) of tantalum [6-9]. This is consistent with the fact that tantalum exists as Ta^{5+} in $ZnTa_2O_6$. The two-doublet peaks observed here may be due to the following possible cause; the formation of non-equilibrated Zn-Ta-O compound (like $Zn_3Ta_2O_8$) together with the equilibrated $ZnTa_2O_6$, particularly on the surface. The co-presence of surfacial compound like $Zn_3Ta_2O_8$ is very likely to cause the appearance of another doublet, due to the differing Ta-O bond length in $Zn_3Ta_2O_8$ (1.80 Å) [10] and $ZnTa_2O_6$ (1.93 Å) [11]. The presence of another compound in the bulk have been suggested by the previous XRD results, and then the XPS results here further confirmed the existence of a non-equilibrated compound, particularly concentrated on the surface.

After the aging for 80 days, the broad spectrum (two-doublet) seen in the initial-state sample was no longer observed and it could be fitted into two peaks (one-doublet) centered at ($4f_{7/2}$) 25.7 eV and ($4f_{5/2}$) 27.6 eV, with the spin orbital splitting of 1.9 eV (Fig. 6.4(a) and Table 6.1). These peak values are consistent with the

binding energy observed for the valence state (+5) of tantalum reported [12-14]. For the sake of comparison, an XPS measurement was carried out for a high-purity commercial Ta_2O_5 in which only Ta^{5+} exists. As a result, the Ta 4f peaks at ($4f_{7/2}$) 25.7 eV and ($4f_{5/2}$) 27.5 eV observed for Ta_2O_5 are also in good agreement with those for the sample after the aging, as given in Table 6.1. The similarity in binding energy of Ta *4f* between the aged sample and the reference Ta_2O_5 sample suggests that the long-term aging at high temperature has possibly stabilized the chemical surface state of Ta in the SE material of $ZnTa_2O_6$.

Table 6.1 Binding energy of Ta 4f peaks of the ZnO(+ 84 wt.% Ta_2O_5) powder samples at initial state and after the aging process, in comparison with the commercial Ta_2O_5 (Reproduced from [24], Copyright 2013, with permission from the American Chemical Society).

Ta *4f*	Binding energy / eV		
	initial state	after aging	commercial Ta_2O_5
$4f_{7/2}$	(i) 26.1 (ii) 27.0	25.7	25.7
$4f_{5/2}$	(i) 28.0 (ii) 28.9	27.6	27.5

The effect of the aging process on the photoelectron spectra of Zn 2*p* is depicted in Fig. 6.4(b). For the initial-state sample, the Zn 2*p* spectra can be fitted into two components, centered at ($2p_{3/2}$) 1020.7 eV and ($2p_{1/2}$) 1043.7 eV, with the spin orbital splitting of 23.0 eV. The binding energy values observed here are similar to those reported for Zn *2p* in ZnO [15-17]. After the aging, the Zn 2*p* signal manifests as two components located at ($2p_{3/2}$) 1021.4 eV and ($2p_{1/2}$) 1044.4 eV. These binding energy

values are also in good agreement with that reported for ZnO where Zn exists as Zn^{2+}[18-20].

The O *1s* spectra of both samples are given in Fig. 6.4 (c), revealing a slight shift in the central binding energy from 529.6 eV into 530.0 eV after the aging. The O *1s* peak at this binding energy value is in good agreement with those reported for Ta-O and Zn-O, whose binding energies are overlapping at approximately same value [13, 16, 20, 21]. Another smaller peak was also observed in both spectra at around 531.0 eV, which may be attributed to the contamination of surface hydroxyl group [22-23].

It can be deduced from these results that initially both of $ZnTa_2O_6$ and the non-equilibrated Zn-Ta-O compounds like $Zn_3Ta_2O_8$ exist on the surface of SE. The aging process is postulated to stabilize the non-equilibrated compound, resulting in the large change in the binding energy of Ta *4f*. The change in Ta *4f* spectra is accompanied by the shift in binding energy of Zn *2p* and O *1s*. Such a stabilization may result in the change in catalytic activities against key reactions which govern sensing-signal generation. Since there are several reactions (i.e. electrochemical reactions and gas-phase reactions) affecting the generation of sensing signal, the next investigations should be carried out with aspiration of determining which reaction would be most affected.

6.3.3 Effect of aging on catalytic activity

The sensing mechanism of the developed sensor has been confirmed to be based on mixed-potential model [2]. When SE of a mixed-potential type sensor is exposed to the sample gas diluted with air, a mixed potential can be established when the cathodic reaction (Eq. 1) and the anodic reaction (represented by Eq. 2 in the case of H_2 sensing) occur at the same rate at the interface of YSZ/SE.

$$2O_2 + 4e^- \rightarrow 2O^{2-} \quad (1)$$

$$2H_2 + 2O^{2-} \rightarrow 2H_2O + 4e^- \quad (2)$$

However, prior to proceeding electrochemical reactions at the YSZ/SE interface, the sample gas will be naturally oxidized within the SE layer by heterogeneous catalysis. Hence, the reactivity to gas-phase reaction (represented by Eq. 3, in the case of H_2 sensing) can control the number of gas species capable of reaching the YSZ/SE interface.

$$2H_2(g) + O_2(g) \rightarrow 2H_2O(g) \quad (3)$$

The mixed-potential model can be commonly rationalized by using polarization curves (Fig. 6.5(a)), where the intersect point of the modified anodic and the modified cathodic polarization curves is assigned as mixed potential (E_m). Therefore, in this study, the changes in catalytic activities against the gas-phase reactions and/or electrochemical reactions before and after the long-term aging were elucidated by the measurements of polarization curves as well as gas-phase catalytic activities.

Initially, the polarization-curve measurements were carried out in the sample gas (H_2, C_3H_6 and CO, diluted with air (21 vol.% O_2)). When the measurements are conducted in an oxygenated atmosphere, the heterogeneous catalysis that usually occurs within the SE layer will deplete fraction of the available sample-gas molecules. Then, the unreacted sample-gas molecules can reach TPB and undergo the electrochemical reactions there. As can be seen from Fig. 6.6, the generated cathodic current values measured in air (21 vol.% O_2) are very low (< 0.1 nA in the examined potential range) for the sensor using ZnO(+ 84 wt.% Ta_2O_5)-SE, both before and after the aging for 80 days. The generated current for anodic reaction of H_2 increased significantly after the aging in the potential range starting from around -750 mV (vs. Pt/air-RE), while those of C_3H_6 and CO were unaffected by the aging.

Before the aging, the combination of low cathodic current of O_2 and low anodic current of the sample gas will result in low mixed potential (as depicted in Fig. 6.5(b)). This was experimentally confirmed to result in low sensitivities for H_2, C_3H_6 and CO (Fig. 6.1(a)). After aging, the significant increase in anodic current of H_2 shifted the mixed potential to a more negative direction (Fig. 6.6(b) and 6.5(c)), which manifested experimentally as the higher H_2 sensitivity (Fig. 6.1(b)). However, since such a drastic increase in anodic current of H_2 was not observed in the cases of C_3H_6 and CO (Fig. 6.6(b)), the sensitivities to these gases after the aging was remained to be low (Fig. 6.1(b).

From the perspective of a mixed-potential model, the increase in the rate of anodic reaction of H_2 after long-term aging may arise from either an increase in the catalytic activity to the anodic reaction of H_2 and/or a decrease in the heterogeneous catalysis to the gas-phase reaction of H_2. To confirm further the change in catalytic activity toward the anodic reactions of each sample gas (H_2, C_3H_6 and CO) before and after the aging, the additional polarization-curve measurements were then conducted in the absence of O_2 (in N_2). Since heterogeneous catalysis is considered to be negligible under this set of conditions, all of the sample gases passing through the SE layer can reach TPB and electrochemically react with O^{2-} .

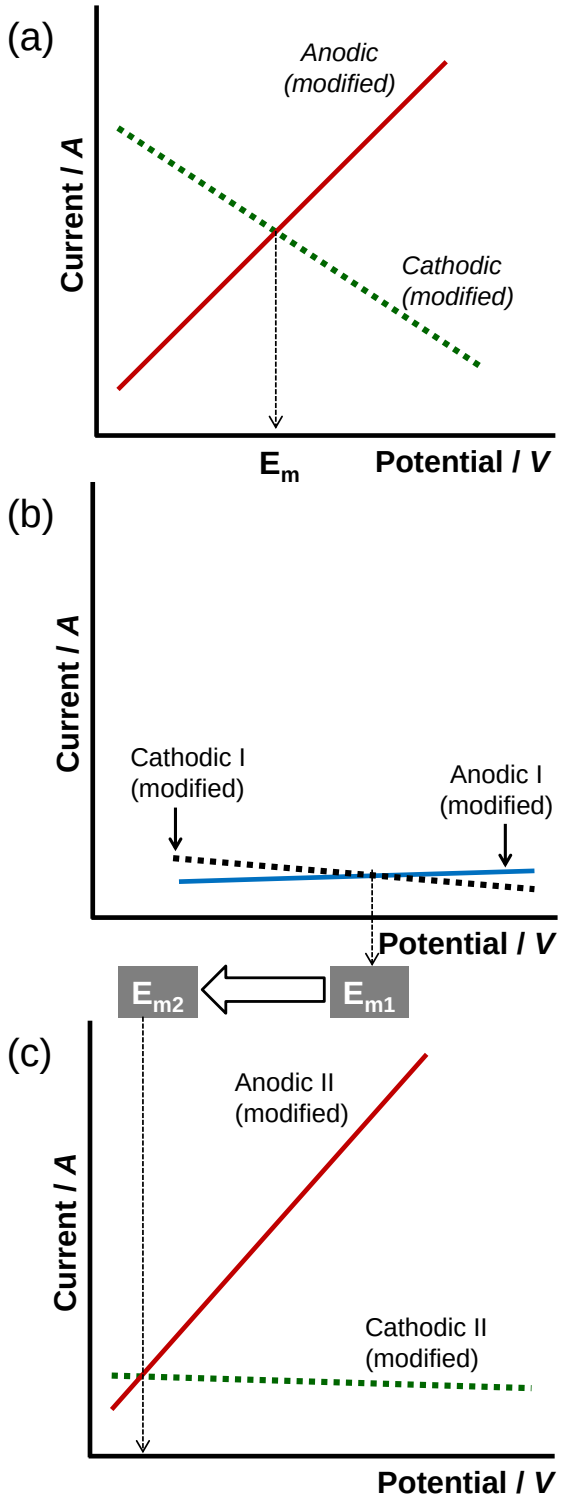

Figure 6.5 Illustration of mixed-potential model by using (a) standard modified polarization-curves and the explanation of the drastic change in gas sensitivity of the developed sensor at (b) the initial state and (c) after aging. (Reproduced from [24], Copyright 2013, with permission from the American Chemical Society).

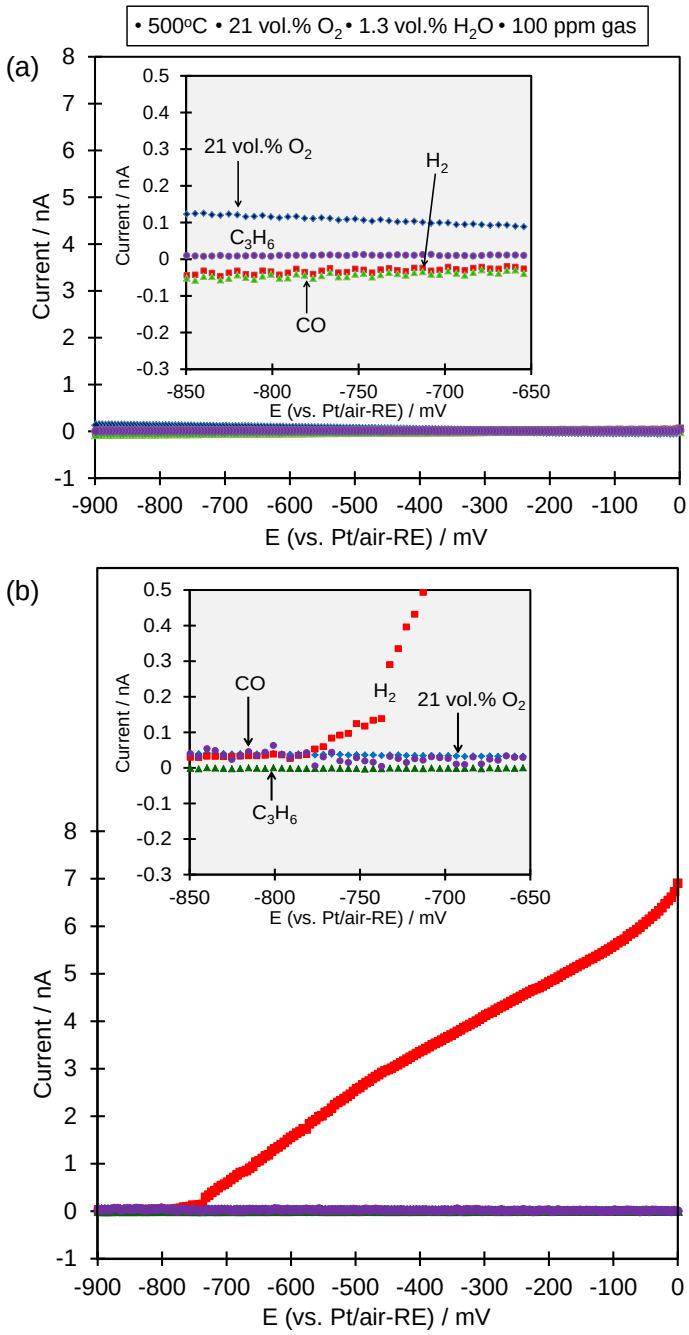

Figure 6.6 The modified polarization curves for the anodic reaction of each sample gas (H_2, C_3H_6 and CO, 100 ppm each) and for the cathodic reaction of 21 vol.% O_2, for the sensor using ZnO(+84 wt.% Ta_2O_5)-SE; (a) initial state and (b) after the aging for 80 days. (Insets are the enlarged figures especially in the potential range of from -850 to -650 mV (vs. Pt/air-RE)). (Reproduced from [24], Copyright 2013, with permission from the American Chemical Society).

Figure 6.7 shows the comparison of polarization curves measured in each sample gas (H_2, C_3H_6 and CO) in the absence of O_2, for the sensor using ZnO(+ 84 wt.% Ta_2O_5)-SE, before and after the aging for 80 days. It is seen from Fig. 6(a) that the anodic current values of each sample gas were rather high even before the aging, when compared with those measured in the presence of O_2 (Fig. 5(a)). It is also clear that the anodic current value of H_2 is relatively higher than those of C_3H_6 and CO both before and after the aging (Fig. 6.7 (a) and (b)). In addition, it is noted that the shapes of anodic polarization curves measured in each sample gas did not significantly changed after the aging (Fig. 6.7 (a) and (b)). These results suggest that the catalytic activity towards the anodic reactions of each sample gas is also not changed largely before and after aging. However, the catalytic activity to anodic reaction of H_2 remains comparatively higher than those of C_3H_6 and CO. By comparing these polarization curves (Fig. 6.7) with those measured in each sample gas diluted with air (Fig. 6.6), it is can be concluded that the heterogeneous catalytic activity to gas-phase reaction only to H_2 is significantly different between the initial and aged samples, while those of C_3H_6 and CO remain high even after the aging process. This, in turn, results in low sensitivities to C_3H_6 and CO, which brings about highly selective response toward H_2, accompanying with high H_2 sensitivity.

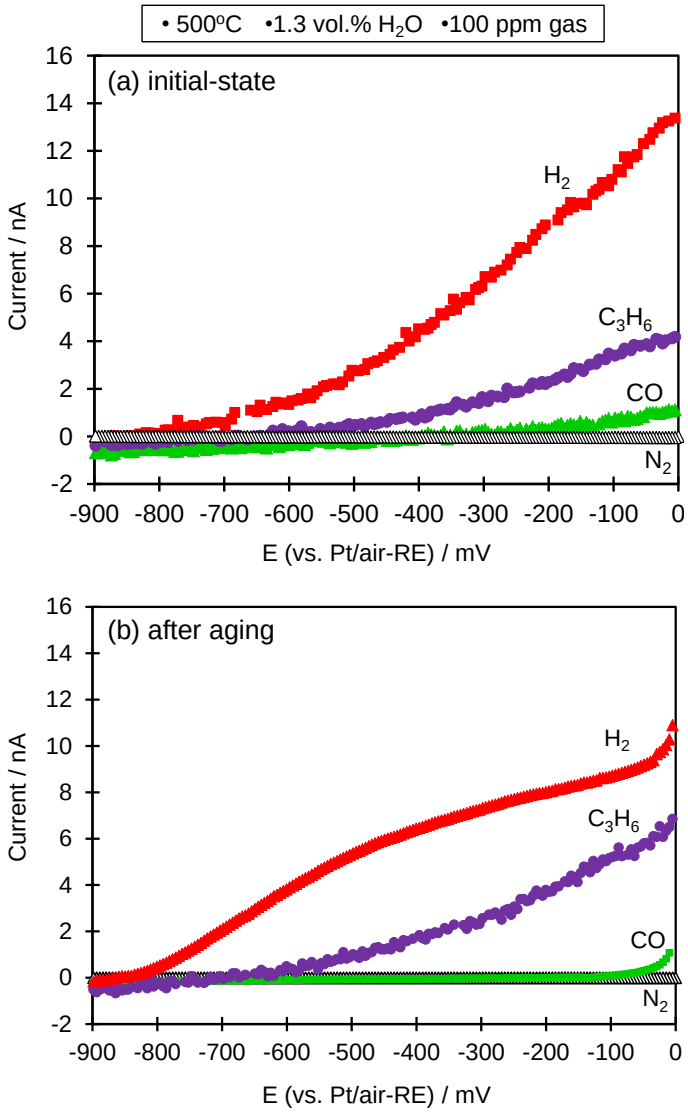

Figure 6.7 The polarization curves measured in each sample gas (H_2, C_3H_6 and CO, 100 ppm each, diluted with N_2), for the sensor using ZnO(+84 wt.% Ta_2O_5)-SE; (a) initial state and (b) after aging for 80 days. (Reproduced from [24], Copyright 2013, with permission from the American Chemical Society).

In order to confirm this assumption, the conversion of sample gas (H_2 or C_3H_6, diluted with air) in the gas-phase oxidation was evaluated. As a result, as shown in Fig. 6.8, the initial-state of ZnO(+84 wt.% Ta_2O_5) powder sample gave higher catalytic activity to the gas-phase oxidation of H_2 when compared with the aged sample; the conversion of H_2 decreased significantly from 50% to 15%, as expected. In contrast, the

C_3H_6 conversion showed only a minor difference between the initial and aged samples. This indicates that the high catalytic activity toward gas-phase reaction of H_2 is significantly decreased by the aging, while that of C_3H_6 is evidently unaffected.

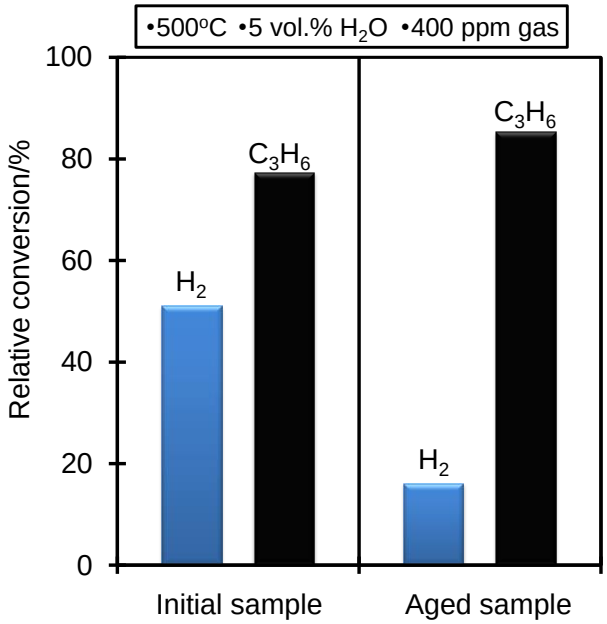

Figure 6.8 Comparison of the conversion of H_2 and C_3H_6 in the gas-phase oxidation on each of the initial and the aged ZnO(+84 wt.% Ta_2O_5) powder samples. (Reproduced from [24], Copyright 2013, with permission from the American Chemical Society).

6.3.4 Aging mechanism in enhancing sensitivity and selectivity against H_2

The aging effects on the sensing performances and the SE material properties are summarized in Table 6.2 and Fig. 6.9. In Fig. 6.9, a thicker arrow indicates higher gas fraction and thinner arrow indicates lower gas fraction. The initial-state morphology of $ZnTa_2O_6$-SE was confirmed to be rather porous with smaller-sized particles. The broad Ta *4f* spectra observed for the initial-state SE material suggests the existence of a non-equilibrated Zn-Ta-O compound (like $Zn_3Ta_2O_8$) together with pure $ZnTa_2O_6$,

particularly on the surface of the SE material. This initial-state SE material possesses high catalytic activity to both of gas-phase reactions and anodic reactions of the sample gases (such as H_2, C_3H_6 and CO). High catalytic activity to gas-phase reaction reduces the number of gas capable of reaching the SE/YSZ interface, as depicted in Fig. 6.9 (a). However, since the reactivity to the anodic reaction of H_2 is higher than those for CO and C_3H_6, a relatively sensitive and selective response toward H_2 was observed at the initial state (before aging).

After a stabilized state was attained by the long-term aging, the SE was comprised of larger particles with relatively lower porosity. A significant change was observed for the chemical surface state of the aged SE material. The long-term aging has presumably stabilized the surficial non-equilibrated Zn-Ta-O compound (like $Zn_3Ta_2O_8$) into a very stable form, resulting in the transformation of Ta *4f* broad peak (two-doublet) into one-doublet with lower binding energy values. This stabilized (aged) SE material has been proven to have a significantly lower catalytic activity to heterogeneous oxidation of H_2, allowing higher fraction of H_2 reach the TPB, as shown in Fig. 6.9(b). However, since the catalytic activity to the heterogeneous oxidation of C_3H_6 (or CO) is still high, the fraction of C_3H_6 (or CO) that reaches the TPB remains low. Despite this, the catalytic activity to anodic reaction of the sample gases (H_2, CO and C_3H_6) was not affected by the aging. Therefore, higher fraction of H_2 can react with O^{2-} at the TPB and result in significant increase in H_2 sensitivity, while maintaining lower sensitivity to CO and C_3H_6.

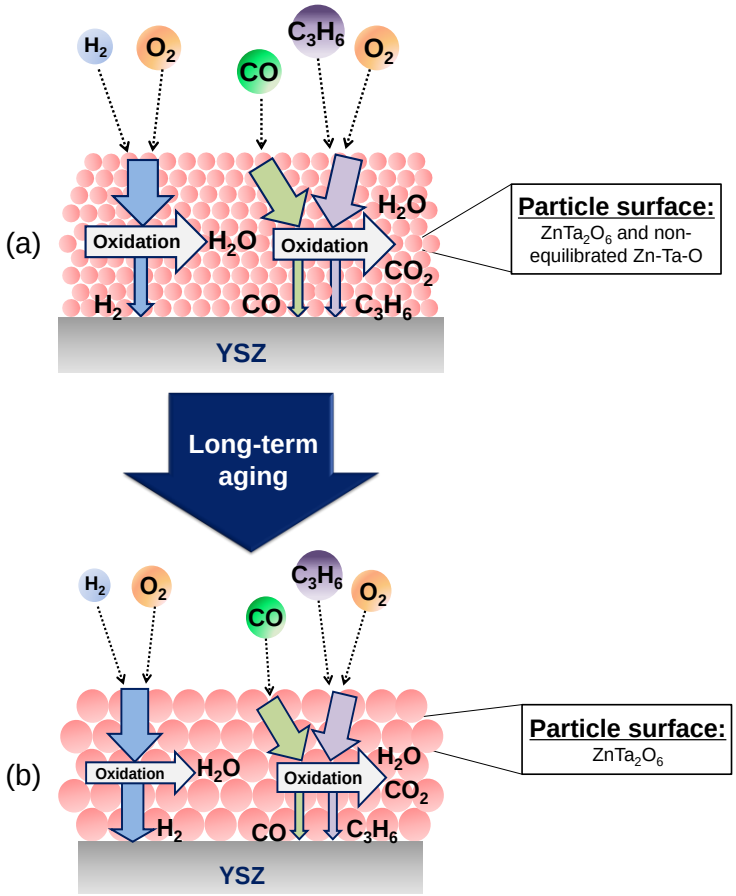

Figure 6.9 Illustration of aging effect on enhancing the sensing performance of the sensor using ZnO(+ 84 wt.% Ta_2O_5)-SE (a) at initial state and (b) after aging (Reproduced from [24], Copyright 2013, with permission from the American Chemical Society).

The fact, that the catalytic activity toward anodic reaction of the sample gases (H_2, CO and C_3H_6) remains unchanged after the long-term aging, suggests that the active sites for anodic reaction of these gases are hardly affected by the aging process. On the contrary, the stabilization process during the aging evidently reduced the number of active sites especially for the heterogeneous catalysis of H_2 oxidation, while those for CO and C_3H_6 seem to be less affected. The major changes in the XPS spectra of Ta *4f* after the aging appear to strongly correlate with the transformation of the initial non-equilibrated surface compound to a fully equilibrated one. The presence of the

non-equilibrated phase at the initial state is believed to possess a comparatively greater number of active sites for the heterogeneous catalysis, facilitating higher rates of H_2 oxidation. This contributed to the higher observed augmentation in both sensitivity and selectivity towards H_2 after aging. However, the reason why only the active site for heterogeneous H_2 oxidation is affected by the aging process remains needs further investigation.

6.4. Conclusions

The effects of the long-term aging on various properties of the SE material have been investigated and characterized for the sensor using ZnO(+ 84 wt.% Ta_2O_5)-SE. The XRD patterns of the SE material before and after the aging for 80 days confirmed the presence of $ZnTa_2O_6$ as the main SE component in the bulk of both samples. The aging process was found to promote particle agglomeration, as suggested by the change in particle size observed in SEM images of the aged sample. The initial-state sample (before the aging) having with its overlapping Ta *4f* peaks may be indicative of the co-presence of the non-equilibrated surficial Zn-Ta-O compound (like $Zn_3Ta_2O_8$) together with stable pure $ZnTa_2O_6$. The initial state sample was confirmed to have high catalytic activities against the gas-phase (heterogeneous) reactions as well as the anodic reactions toward each sample gas (H_2, CO and C_3H_6), resulting in lower sensitivity and moderate selectivity to H_2. During the aging process, the non-equilibrated Zn-Ta-O compound existing on the surface of the SE material was stabilized and was converted to an equilibrated compound (pure $ZnTa_2O_6$), as suggested by the well-defined valence state of Ta 4*f* which was in good agreement with the Ta^{5+} oxidation state. The stabilized SE material was found to have a lower catalytic activity to the heterogeneous oxidation of H_2, and it maintained a preferential catalytic activity to the anodic reaction of H_2,

compared with those for CO and C_3H_6. This caused the developed sensor become highly sensitive and highly selective toward H_2 after the long-term aging. Future investigation will be focused on reducing the long stabilization time.

(Some of the contents in this chapter is the accepted manuscript version of a published work that appears in final form in [24], Copyright © American Chemical Society and the Division of Chemical Education, Inc., after peer review and technical editing by the publisher. To access the final edited and published work, please see [24])

Table 6.2 Summary of effect on various properties and sensing properties of the ZnO(+ 84 wt,% Ta_2O_5)-SE material. (Reproduced from [24], Copyright 2013, with permission from the American Chemical Society).

SE condition	main SE component (bulk)	particle size	XPS spectra (Ta *4f*)	catalytic properties				gas sensitivity	gas selectivity
				sample gas	gas-phase (heterogeneous)	anodic reaction in sample gas	cathodic reaction of O_2		
initial state	$ZnTa_2O_6$	smaller	two-doublet (in higher binding energy)	H_2	high	high	low	low	moderate
				C_3H_6	high	moderate		low	low
				CO	high	lower		low	low
after aging	$ZnTa_2O_6$	larger	one-doublet (in lower binding energy)	H_2	**low**	high	low	**high**	**high**
				C_3H_6	high	moderate		low	low
				CO	high	lower		low	low

References

[1] Anggraini, S. A.; Breedon, M.; Miura, N. *Sens. Actuators, B* , 187(2013), 58-64.

[2] Anggraini, S. A.; Breedon, M.; Miura, N. *Electrochem. Commun.* , 31 (2013**)** 133-136.

[3] Fujio, Y.; Plashnitsa, V. V.; Elumalai, P.; Miura, N. *Talanta* , 85 (1) (2011**)** 575-581.

[4] Plashnitsa, V. V..; Elumalai, P.; Kawaguchi, T.; Fujio. Y.; Miura, N. *J. Phys. Chem. C*, 113(18), (2009) 7857-7862.

[5] Yamaguchi, M.; Anggraini, S. A.; Fujio, Y.; Sato, T.; Breedon, M.; Miura, N.; *Int. J Hydrogen Energy*, 38(1), (2013) 305-312**.**

[6] Mahmood, K.; Park, S. B.; Sung, H. J. *ACS Appl. Mater. Interfaces*, 5(9) (2013)3722-3730**.**

[7] Basame, S. B.; White, H. *Langmuir* , 15(3) (1999) 819-825**.**

[8] Skadtchenko, B. O.; Trudeau, M.; Kwon, C.; Dunn, B.; Antonelli, D. *Chem. Mater.*, 16(15),(2004) 2886-2894**.**

[9] Xu, C.; Xiao, Q.; Ma, J.; Jin, Y.; Shao, J.;Fan, Z. *Appl. Surf. Sci.*, 254 (20), (2008) 6554-6559.

[10] Waburg, M.; Müller-Buschbaum, H.*Monatshefte für Chemie*, 115 (1984) 15-20.

[11] Waburg, M.; Müller-Buschbaum, H.*Z. Anorg. A llg. Chem.*, 508(1984) 55-60.

[12] Tüysüz, H.; Chan, C. K. *Nano Energy* , 2(1) (2013) 116-123**.**

[13] Wei, A. X.; Ge, Z. X.; Zhao, X. H.; Liu, J.; Zhao, Y. *J. Alloys Compd.*, 509(41),(2011) 9758-9763**.**

[14] Wang, N.; Li, H.; Wang, J.; Chen, S.; Ma, Y.; Zhang, X. *ACS Appl. Mater. Interfaces*, 4(9), (2012) 4516-4523**.**

[15] Wang, J.; Tsuzuki, T.; Tang, B.; Hou, X.; Sun, L.; Wang, X. *ACS Appl. Mater. Interfaces*, 4(6), (2012) 3084-3090**.**

[16] Deng, X.; Yao, K.; Sun, K.; Li, W.; Lee, J.; Matranga, C. *J. Phys. Chem. C*, 117(21) (2013), 11211-11218**.**

[17] Agrell, J.; Boutonnet, M.; Melian-Cabrera, I.; Fierro, J. L. G. *Appl. Cat. A*, 253(1), (2003) 201-211**.**

[18] Zheng, Y.; Zheng, L.; Zhan, Y.; Lin, X.; Zheng, Q.; Wei, K. *Inorg. Chem.*, 46(17), (2007) 6980-6986**.**

[19] Chen, C.; He, H.; Lu, Y.; Wu, K.; Ye, Z. *ACS Appl. Mater. Interfaces*, 5(13),(2013) 6354-6359**.**

[20] De la Rosa, E.; Sepulveda-Guzman, S.; Reeja-Jayan, B.; Torres, A.; Salas, P.; Elizondo, N.; Yacaman, M. J. *J. Phys. Chem. C*, 111(24), (2007) 8489-8495**.**

[21] Wu, S. J.; Houng, B.; Huang, B. *J. Alloy Compd.* , 475(1-2) (2009), 488-493.

[22] Karamat, S.; Rawat, R. S.; Lee, P.; Tan, T.L.; Ramanujan, R.V.; Zhou, W. *Appl. Surf. Sci*, 256(8) (2010) 2309-2314.

[23] Wang, J.; Xu, M.; Zhao, R.; Chen, G. *Analyst*, 135(8), (2010) 1992-1996

[24] Anggraini, S. A; Breedon, M.; Ikeda, H.; Miura, N.; *ACS Appl. Mater& Interfaces*, 5(22), (2013) 12099-12106.

Chapter 7

Summary and Future Works

7.1 Summary of the thesis

A systematic and multi-facet approach for the development of highly selective and sensitive mixed-potential type YSZ-based H_2 sensor using oxide-based-SE has been carried out in this study. Method for obtaining a highly selective H_2 response can be divided into two main platforms. One approach is the sensor (or sensing electrode (SE)) configuration modification and another approach is surface (or morphology) transformation.

The first route in sensor-configuration approach which was conducted by refashioning the typical separated YSZ-based sensor configuration into a combined-electrode configuration was discussed in Chapter 2. Among the tested oxides as a prospective H_2 sensitive material, the sensor using SnO_2-SE generated the highest H_2 sensitivity. The mechanical strength of SnO_2 was improved by the addition of 30 wt.% YSZ into SnO_2. When SnO_2(+30 wt.% YSZ)-SE was paired with NiO-TiO_2-RE', the resulting sensor exhibited sensitive and selective response toward H_2. This combined-type sensor could detect H_2 in the range of 20-800 ppm with response time less than 30 s. The H_2 sensitivity was also hardly affected by the change of water vapor concentration (1-5 vol.%).

In Chapter 3, the second route in sensor-configuration approach was elaborated which was done by filtering the unwanted gas species before reaching the TPB. A specific oxide-based catalyst layer was initially screened and Cr_2O_3 was selected. Direct deposition of Cr_2O_3 on top of SnO_2(+ 30 wt.% YSZ)-SE was found to give a detrimental

effect to the H_2 sensing characteristic of the sensor. Investigation regarding the sensing performance deterioration led to the conclusion that direct deposition of Cr_2O_3 allows some of Cr_2O_3 particle to easily penetrate the SnO_2-SE and reach the TPB. The presence of Cr_2O_3 at TPB was confirmed to alter the H_2 sensing characteristic. The presence of an intermediate Al_2O_3 layer that sandwiched between SE and catalyst layer could successfully prevent Cr_2O_3 intrusion and maintain Cr_2O_3 function as a catalyst layer. The sensor using SnO_2(+YSZ)/Al_2O_3/Cr_2O_3-SE exhibited a selective and sensitive H_2 response. The consistency between the mixed potential estimated from polarization curve measurements and the observed sensitivity indicates that the sensing mechanism of the sensor using multilayer electrode was based on mixed-potential model.

Morphology transformation approach to attain a highly selective H_2 response was proposed by increasing the sintering temperature. In Chapter 4, the investigation was started by systematically examining the sensing characteristic of sensor using ZnO with different addition of Ta_2O_5. The addition of 30 wt.% Ta_2O_5 into ZnO formed a composite that composed of ZnO and $Zn_3Ta_2O_8$ as the main component, which was generated the highest H_2 sensitivity. After sintering at 1300^{o}C, the sensor using ZnO(+ 30 wt.% Ta_2O_5)-SE which was confirmed to comprised of $Zn_3Ta_2O_8$ and ZnO-SE demonstrated a highly sensitive and selective response toward H_2. Denser and more tortuous morphology that was observed after the sensor sintered at 1300^{o}C is believed to hinder larger-sized gas molecule such as hydrocarbons to move through and only allow smaller-sized gas with high mobility like H_2 to pass and reach TPB. Reduction of O_2 fraction reaching the TPB decreased the reactivity of electrochemical reaction of O_2. This lead to the shift of the mixed-potential to a more negative direction, thus higher sensitivity was observed.

Aging process is another route in surface and morphology modification that was

introduced and investigated in Chapter 5, for the sensor using another Zn-Ta-based oxide, i.e., $ZnTa_2O_6$. The $ZnTa_2O_6$-based-SE, which was obtained by adding 84 wt.% Ta_2O_5 into ZnO, was capable of generating the highest response toward H_2, compared with other examined electrode composition. The SE morphology and electrode composition was found to be affected by the change of Ta_2O_5 additions. Long-term aging process enhanced H_2 sensing characteristic drastically. Polarization-curve measurements for incrementally increasing concentrations of H_2 confirmed that the gas diffusion in the SE layer is the rate-determining step of the present sensor in the lower H_2 concentration range (10-80 ppm). While in the higher H_2 concentration range (100-400 ppm), the electrochemical reaction of H_2 (or O_2) occurring at the interface of SE/YSZ was identified as the rate-determining step. Good agreement between the estimated mixed-potential value and the obtained H_2 sensitivity suggests that the sensing mechanism of the sensor after aging also obeys the mixed-potential model.

The effects of the long-term aging on various properties of the sensor using $ZnTa_2O_6$-based-SE was analyzed via series of measurements and elaborated in Chapter 6. The XRD patterns of the SE material before and after the aging for 80 days confirmed the presence of $ZnTa_2O_6$ as the main SE component in the bulk of both samples. The aging process was found to promote particle agglomeration, as suggested by the change in particle size observed in SEM images of the aged sample. The overlapping Ta *4f* peaks that observed for the initial-state sample may be indicative of the co-presence of the non-equilibrated surficial Zn-Ta-O compound (like $Zn_3Ta_2O_8$) together with stable pure $ZnTa_2O_6$. The initial state sample was confirmed to have high catalytic activities against the gas-phase (heterogeneous) reactions as well as the anodic reactions toward each sample gas (H_2, CO and C_3H_6), resulting in lower sensitivity and moderate selectivity to H_2. During the aging process, the non-equilibrated Zn-Ta-O

compound existing on the surface of the SE material was stabilized and was converted to an equilibrated compound (pure $ZnTa_2O_6$), as suggested by the well-defined valence state of Ta 4*f* which was in good agreement with the Ta^{5+} oxidation state. The stabilized SE material was found to have a lower catalytic activity to the heterogeneous oxidation of H_2, and it maintained a preferential catalytic activity to the anodic reaction of H_2, compared with those for CO and C_3H_6. This caused the developed sensor become highly sensitive and highly selective toward H_2 after the long-term aging.

7.2 Future works

Several platforms for obtaining highly selective H_2 sensor technology has been presented and addressed in this thesis and also reported in many high impact factor publications. Despite the advancement that has been made in this research, a number of future directions listed below, would bring an optimization on the current sensing performance of the developed sensor.

a) Acceleration of stabilization period

The excellent sensitivity and selectivity that was demonstrated by the sensor using $ZnTa_2O_6$-based-SE after aging showed a potential of the sensor to be used in real H_2 monitoring applications. However, the 40 days of aging that is required to stabilize and achieves this outstanding sensing characteristic may not be necessarily advantageous for practical application. Therefore, to promote a greater possibility for the sensor to be employed in real and wider application, the stabilization period need to be reduced to a shorter timeframe.

b) Detail analysis on gas-solid interaction

Although the sensing mechanism and aging mechanism has been clarified in this thesis, detail fundamental work on gas-solid interaction has yet to be investigated and

verified. For example, detail clarification on why $ZnTa_2O_6$ has low catalytic activity only toward H_2 oxidation while other oxide such as Cr_2O_3 has higher catalytic activity toward HCs than to H_2 oxidation would be very useful for those who have interest, including but not limited, to gas sensor field.

c) Extension of the lower detection limit to sub-ppm level.

The lowest H_2 concentration that can be detected using the currently developed sensor is 10 ppm. This may be more than sufficient to prevent the H_2 explosion due to H_2 leakage. However, given that an H_2 sensor will not only be used as a detector but also a concentration monitor, it is important that the sensor could detect H_2 at lower level (sub-ppm), when it happens, the sensor can be used for wider applications.

d) Sensor miniaturization

As has been mentioned in Chapter 1, portability is another desired feature that also defined a high performance sensor. Planar configuration is a widely accepted and popular configuration for sensor miniaturization. Under planar configuration both SE and RE exposed to the same testing gas, the resulted sensing characteristic might be different from the separated/tubular configuration. Given the excellent sensing performances showed by the developed sensor, an optimization of the miniaturized H_2 sensor using the proposed oxide-SE under planar or rod geometry would be also pivotal for H_2 economy scenario implementation and also for other applications that involved H_2 such as petrochemical or metallurgical industries, nuclear power station and also rocket engine for space exploration.

ACKNOWLEDGEMENTS

First and foremost, I would like to express my heartfelt gratitude to my supervisor Professor Norio Miura for every bit of support, time, guidance, assistance, encouragement and expertise he has provided since the first day I work in his lab. More importantly, I want to thank him for giving me the second chance that I thought will never come. His spirit and enthusiasm for research and health matter was inspiring, contagious and motivational for me. It has been a great experience and also an honor to be one of his PhD students.

I would like to acknowledge Kyushu University and Takenoko Foundation for granting me scholarship for my doctoral study and made my PhD work possible. I would also like to thank my thesis examiners, Professor Yasutake Teraoka and Professor Shigeru Fujino, for their thoughtful and constructive comments and feedback. I would like to extend my gratitude to Dr. Yoshinori Miura, from Kyushu University Center for Advanced Instrumental Analysis for his assistance during the XPS measurements and discussion regarding the XPS analysis.

A good supporting system and friendship is always important to survive in graduate school and Miura-lab has been a source of friendship and research collaboration. Therefore, I would like to thank to the former member of Miura-lab whom I considered as my mentor; Dr. Vladimir Plashnitsa, Dr. Yuki Fujio, Dr. Michael Breedon and Dr. Perumal Elumalai. They have shared and taught me a great deal about research in gas sensor, electrochemistry, and material science, provided help for my publications and at the same time, becoming my good friends. I am also grateful for all staffs in Miura lab, particularly; Dr. Hiroshi Ikeda, Ms. Naomi Mori and Ms. Taeko Hashiguchi, for their generous assistance during my doctoral study. Ms. Keiko Kusunoki also deserves

special thanks, not only for the very substantial help she gave for my study and some personal matters, but also for the warm and sincere friendship.

I also thank my comrades in Miura lab; Dr. Tomoaki Sato (my lab mate and also my travel mate in many conferences for the past 3 years). His kind help and patience in many things during my doctoral study are highly appreciated. Also to Dr. Han Jin (my former lab mate) for the stimulating discussions we used to have and for providing me a fun environment to work. I would also like to thank the former and the current master students in Miura-lab for the happy and fun friendship for the past 3 years, particularly to Ms. Mami Yamaguchi who has collaborated with me and give me permission to use some of her data. I would also like to thank all my best friends whom I miss so much (I will not mention you guys here, but you know who you are), for being a good listener and for always putting up with me.

Special thanks go to my entire big family; my parents, sister and brother, the in-laws, for their non-stop prayers, love and supports for me. To my dearly loved daughter, Lintang Arista Wahyudi, for always being my motivation and driving force. Final acknowledgement is saved for my beloved husband and my very best friend in the world, Dr. Sugeng Wahyudi, for the endless support, love and encouragement. Thank you for letting me rekindles my dreams and for never stops having faith in me.

Alhamdulillah.

Fukuoka, December 2013
Sri Ayu Anggraini